Parallel Computing and the *IRAS* Galaxy Atlas

Thesis by
Yu Cao

In Partial Fulfillment of the Requirements
for the Degree of
Doctor of Philosophy

California Institute of Technology
Pasadena, California
1997
(Submitted October 31, 1996)

Acknowledgements

I have been fortunate to have Tom Prince as my advisor. Tom started me on a new project which greatly suited my interests, and ever since then he has never failed to guide me with his exceptional ability to see the big picture and to pay attention to details at the same time. His clear and logical way of thinking has influenced me tremendously. The close scrutiny he paid to my writings, and his insistence on polished yet unpretentious presentation have been invaluable parts of the training I received as a graduate student.

I would like to thank Sue Terebey for the crucial contributions she made to the project. Her serious, careful, enthusiastic, and perfectionist approach played a critical role to establish the quality of the project's primary product – the *IRAS* Galaxy Atlas.

I am thankful to Chas Beichman for his general guidance and advice, and for his masterful coordination (together with Tom) of the algorithmic and processing works.

I would like to thank H. H. Aumann, John Fowler, and Michael Melnyk for developing the HIRES program at IPAC, which laid the foundation for the topics discussed in this thesis. Tom Soifer, Jason Surace, and Joe Mazzarella were closely involved in the starting phase of the *IRAS* Galaxy Atlas project and helped me get acquainted with the relevant subjects when I was a complete novice. John Fowler, as one of the chief developers of HIRES, has been a consistent source of help over the past four years on countless subjects including details of *IRAS* instrumentation, the HIRES software, and new developments in the algorithm. I am grateful to Ron Beck and Diane Engler, who spent endless hours running the Atlas production (including several rounds of reprocessing) and numerous other HIRES jobs.

Thanks are also due to the system administrators at the Space Radiation Lab, Center for Advanced Computing Research, IPAC, and the Campus Computing Organization – Laura Carriere, Minerva Calderon, Jack Stuart, Jan Lindheim, Heidi Lorenz-Wirzba, Bevan Bennett, Sharon Brunett, Gary Olsen, Jack Lampley, Heather Sherman, and Roger Murray, for their excellent job in keeping the computer systems running, and for their help with my requests of various sorts.

I thank Professors John Preskill, Jim Bower, Christoph Koch, Ken Miller, Jerry Pine, and Ed Posner, for serving as my advisors before I settled down in Tom Prince's group. I am especially grateful to Ken Miller and Ed Posner, who encouraged and guided me through some of the more difficult times.

I would like to thank Stuart Anderson and Deepto Chakrabarty for their great job of developing the SRL thesis LaTeX style, which benefited the writing of this thesis tremendously. In addition, many LaTeX formating methods were borrowed from Deepto's thesis.

I appreciate the time spent and careful reading of the thesis by the professors on my committee, namely, Professors Gerry Neugebauer, Steve Frautschi, Michael Cross, and Chas Beichman.

I am grateful to the following friends at Caltech: Zhen Hu, Wen Jiang, Alex Zheng, Guangqing Chen, Bingqing Chen, Haiyan Gao, Jianzhong Li, Rongzhi Liu, Isaac Wong, Dawei Dong, Mingsheng Han, Yong Guo, Yixin Liu, Yonggang Jin, Hoimin Leung, Danny Koh, Nina Lu, and Ah San Wong. Most of them have left Caltech by now, and I wish them all the success and happiness they deserve.

Having spent much of my time on the computer and the Internet, I've made some friends on the Internet Go Server and the Internet Relay Chat: USTC, xiang, PL, blondie, veg, dee, vlad, beatme, hsh, zhuge, yen, rnz, zhouzi, april, zooie, road, LianBo, su, ia73, gumpy, cany, aydi, congcong, Jiang, and Ekta. Although I've only met about a half of them in real life, they've all made the late night working hours much more enjoyable.

I am forever indebted to Sunny, Ingrid, my brother Yang, and my parents, for generously providing their love, support, and inspiration.

I would also like to acknowledge the support I received from the Sir Run Run Shaw Foundation, and the NASA Astrophysics Data Program under contract No. NAS5-32642.

Abstract

The *Infrared Astronomical Satellite* carried out a nearly complete survey of the infrared sky, and the survey data are important for the study of many astrophysical phenomena. However, many data sets at other wavelengths have higher resolutions than that of the co-added *IRAS* maps ($4' - 5'$), and high resolution *IRAS* images are strongly desired both for their own information content and their usefulness in correlation studies.

The HIRES program was developed by the Infrared Processing and Analysis Center (IPAC) to produce high resolution ($\sim 1'$) images from *IRAS* data using the maximum correlation method (MCM). We describe the port of HIRES to the Intel Paragon, a massively parallel supercomputer, and other software tools developed for mass production of HIRES images.

Images produced from the MCM algorithm sometimes suffer from visible striping and ringing artifacts. Correcting detector gain offsets in the reconstruction scheme was found to be effective in suppressing the striping artifacts. A variation of the destriping algorithm was used to subtract zodiacal emission. Using a Burg entropy metric in the image space gave good ringing suppression results for some test cases, but was found to have difficulties with photometry and resolution enhancement and hence not used in subsequent image production. A different ringing suppression algorithm was later developed, which aims to maximize cross log entropy between measured and modeled data. The algorithm suppresses point source ringing, and gave scientifically superior image for the α Ori test field. A partial convergence proof for the log entropy algorithm was achieved.

HIRES images in the 60 and 100 μm wavelength bands were produced for the Galactic plane ($-4.7^\circ < b < 4.7^\circ$) and the Orion, ρ Ophiuchi, and Taurus-Auriga molecular clouds, using the MCM algorithm plus the gain compensation destriping technique (ringing suppression was not used because the cross log entropy algorithm had not been developed when the processing started). The images and ancillary maps comprise the *IRAS* Galaxy Atlas. The Atlas images have resolution of approximately $1' - 2'$.

Beam matching of the 60 and 100μm images for the star forming region W3-5 was carried out using the cross-band simulation technique, and a geometrical model was built for a wind-blown shell in W4.

Contents

List of Figures

List of Tables

Chapter 1

Introduction

1.1 Overview

The *Infrared Astronomical Satellite* (*IRAS*, Figure 1.1) provided our first comprehensive look at the infrared sky, producing a nearly complete survey at mid- to far-infrared wavelengths (12, 25, 60, and 100 μm) (Beichman 1987; Soifer, Houck, & Neugebauer 1987; *IRAS* Catalogs and Atlases: Explanatory Supplement 1988). Images made from the *IRAS* survey data show a wealth of extended structure from star-forming regions and other components of the interstellar medium. A variety of studies exploiting the *IRAS* images have been made to date ranging from structure on a Galactic scale to detailed studies of individual molecular clouds (e.g., Beichman et al. 1986; Weiland et al. 1986; Terebey & Fich 1986; Boulanger & Perault 1988; Sodroski et al. 1989; Scoville & Good 1989; Snell, Heyer, & Schloerb 1989; Clemens, Yun, & Heyer 1991; Wood, Myers, & Daugherty 1994). The strength of *IRAS* is the completeness of the survey. However, in many cases the spatial resolution of the comparison data sets at other wavelengths is better than for *IRAS*, and thus the $4' - 5'$ resolution of the released *IRAS* images (the *IRAS* Sky Survey Atlas, *IRAS* Sky Survey Atlas Explanatory Supplement 1994) can limit the comparison. The desire for higher spatial resolution combined with the paucity of new infrared satellite missions has inspired many efforts to extract high spatial resolution information from the data (e.g., Assendorp et al. 1995; Bontekoe et al. 1994; Bontekoe et al. 1991). The products most widely accessible to the US science community are the HIRES images distributed by the Infrared Processing and Analysis Center (IPAC), which are based on the maximum correlation method (MCM; Aumann, Fowler, & Melnyk 1990; Fowler & Aumann 1994). The HIRES images have been

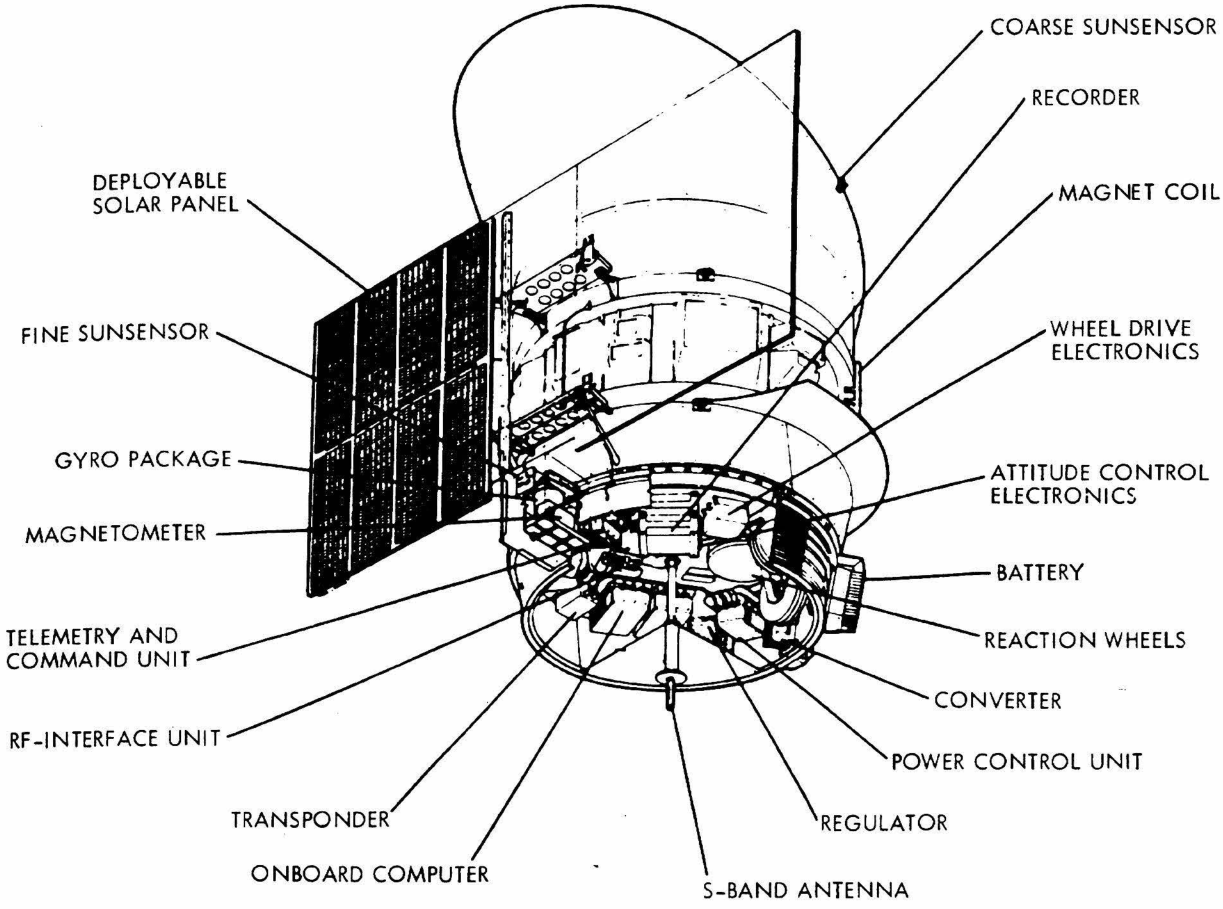

Figure 1.1: *IRAS* spacecraft configuration. (Adapted from Figure II.A.1, *IRAS* Catalogs and Atlases: Explanatory Supplement 1988.)

successfully used for a variety of Galactic and extra-Galactic studies (Rice 1993; Surace et al. 1993; Terebey & Mazzarella 1994).

Application of the HIRES algorithm to the *IRAS* data has been limited largely by the computational resources available for HIRES processing. A $1^\circ \times 1^\circ$ field of typical scan coverage takes 1 hour of CPU time on a Sun SPARCstation 10, for all four wavelength bands and 20 iterations (at which point artifacts limit further improvement of image quality). To overcome these CPU limitations we have undertaken the porting of the HIRES software to the Intel Delta and Paragon parallel supercomputers. HIRES processing is now feasible for large regions of the sky. As part of a program in high-performance computational science and engineering, Caltech has developed significant software and hardware capabilities for massively parallel computing (also called *concurrent supercomputing*). Among the several concurrent computers currently available at Caltech is the 512-node Intel Touchstone Delta, a prototype parallel supercomputer with measured performance of 13 GFLOPS, 8 gigabytes of memory, and 90 gigabytes of disk. Upgraded resources include a 56-node and a 512-node Intel Paragon. The new 512-node Intel Paragon Model L38 has a peak speed of 38.4 GFLOPS, 16 gigabytes of memory, and 14 RAIDs that control 67.2 gigabytes of disk, one Ethernet node, two HIPPI nodes, and six service nodes. The high demand for HIRES images, along with the availability of parallel computing facilities, motivated the port of HIRES to the parallel supercomputers.

The development of new artifact reduction algorithms allows the iterative procedure to be carried much further, requiring more CPU time and further justifying the parallel computing approach.

These efforts made possible a large scale mapping project: high resolution *IRAS* mapping of the Galactic plane. The new *IRAS* Galaxy Atlas (IGA) maps provide a 20-fold improvement in areal information content over current *IRAS* 60 and 100 μm maps and will be valuable for a wide range of scientific studies, including: 1) The structure and dynamics of the interstellar medium (ISM); 2) Cloud core surveys within giant molecular clouds; 3) Determination of initial mass functions (IMFs) of massive stars; 4) Study of supernova remnants (SNRs).

The IGA images will be made available on-line at IPAC and delivered to the National Space Science Data Center. Alternatively, standard four band HIRES images can be requested from IPAC.

1.2 Organization of the Thesis

This thesis describes the algorithmic enhancements and software developments that led to the high resolution *IRAS* Galaxy Atlas, documents the characteristics of the Atlas images, and presents some analysis of the W4 H I region using the images.

The rest of this chapter provides the necessary information about *IRAS* (Section 1.3), followed by descriptions of some science topics that may benefit from the availability of high resolution *IRAS* images of the Galactic plane (Sections 1.4 and 1.5).

The original HIRES algorithm which produces high resolution *IRAS* images and later enhancements developed by the author are described in Chapter 2. The maximum correlation method (MCM) algorithm (Aumann, Fowler, & Melnyk 1990) produces high resolution images from the survey and additional observation (AO) data, using a nonlinear iterative scheme. The resulting images have resolution of about $1'$, compared to the $4'$ – $5'$ subtended by the 100 μm band detectors in the *IRAS* focal plane. A description of the basic MCM algorithm is outlined in Section 2.1. Section 2.2 reviews the history, properties, and enhancements of the Richardson-Lucy algorithm (equivalent to one form of MCM). In Sections 2.3 and 2.4, we offer descriptions of artifact reduction algorithms, namely using estimates of gain offset to eliminate striping, and two different methods to suppress ringing around bright point sources. This chapter is adapted with changes from Cao et al. (1996a) and Cao, Eggermont, & Terebey (1996).

Chapter 3 serves as a documentation and user's guide for the *IRAS* Galaxy Atlas. The IGA covers more than 3300 square degrees of the Galactic plane, plus more than 1100 square degrees of the Orion, ρ Ophiuchi, and Taurus-Auriga molecular clouds. This compares with the roughly 1200 square degrees of sky that IPAC had processed with HIRES in the two years (using workstations alone) prior to the IGA production. Processing issues are discussed first in Section 3.3, including the overview of the production pipeline (Section 3.3.1), the calibration and zodiacal light subtraction of detector data using a spin-off method of the destriping algorithm (Section 3.3.2), reprojection of the data coordinates from Equatorial to Galactic (Section 3.3.3), and issues related to flux bias (Section 3.3.4). Section 3.4 deals with the parallelization strategy of the image reconstruction program. In the parallel processing each $1^\circ \times 1^\circ$ image field is mapped to an 8- or 16-node process grid, which shares the computation by loading different observation scans. An efficiency of 60% is reached with 8 nodes. Image characteristics (resolution, photometric accuracy, positional accuracy, surface brightness accuracy, mosaic property, and residual hysteresis effect) are discussed and quantified in Section 3.5. and image artifacts (striping, ringing, glitching, and discontinuity) are documented in Section 3.6. Also example images from the Atlas are presented in Section 3.7. This chapter is adapted with changes from Cao et al. 1996b.

In Chapter 4, we describe some preliminary analysis of the 60 and 100 μm images for the W3-5 field, a star-forming region in the outer Galaxy. The cross-band simulation technique was employed to provide beam matched images in the two wavelength bands.

And finally, Chapter 5 summarizes the topics and contributions discussed in the thesis.

1.3 Relevant Information about *IRAS*[1]

In this section we introduce the basic information about *IRAS* necessary for the topics covered in this thesis.

IRAS was launched into its 900 km altitude, 99° inclination Sun-synchronous polar orbit with a period of 103 minutes. This orbital altitude was low enough to be below most particles in the Earth's trapped particle belts yet high enough that only a negligible amount of residual atmospheric gases would build up on the cold mirror surfaces during the mission. With the telescope pointing radially away from the Earth and perpendicular to the Sun vector, no radiation from the Earth or the Sun could enter the telescope and all ecliptic latitudes would be swept out during one orbit while, as the line of nodes precessed at a rate of about 1° per day to remain perpendicular to the Sun vector, a natural scanning motion was provided and all ecliptic longitudes would be covered in a period of six months (Figure 1.2). The attitude control system and telescope were designed to allow pointing away from the local vertical within certain constraints, giving the telescope more pointing flexibility.

The *IRAS* survey was designed for the identification of point sources, rather than as an imaging instrument. The data were taken with rectangular detectors that scanned the sky multiple times in "push-broom" fashion (e.g., see Figure 1.3). The satellite data are fundamentally in the form of one-dimensional data streams for each detector. During post-processing it was discovered that two-dimensional images could be made by stitching together, i.e., co-adding, these one-dimensional detector streams. This basic processing accounts for many of the characteristics of the *IRAS* images. For example, stripes are a common image artifact because there are offset and gain variations in the one-dimensional detector streams. Also, the shape of the beam varies from place to place because the coverage (i.e., number and orientation of one-dimensional detector streams) is nonuniform. The effective data oversampling make the *IRAS* data amenable to resolution enhancement because of the geometric information contained within overlapping data samples.

The *IRAS* focal plane (shown in Figure 1.4) included eight staggered linear arrays subtending 30′ in width, two in each of four spectral bands at 12, 25, 60, and 100 μm. Data rate considerations forced the detector sizes to be much larger than the diffraction limit of

---

[1] The material in this section has been mostly drawn from *IRAS* Catalogs and Atlases: Explanatory Supplement 1988.

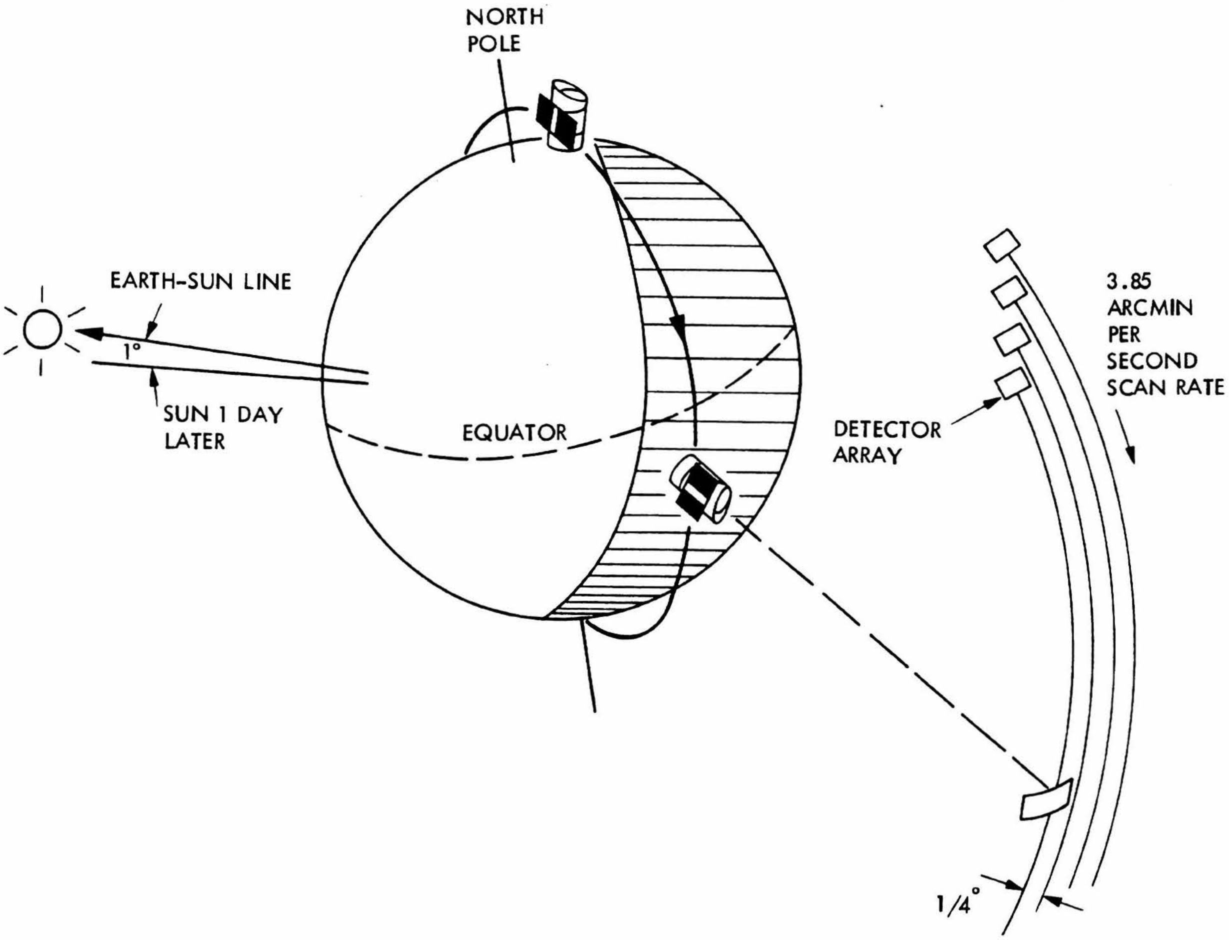

Figure 1.2: A schematic drawing of the *IRAS* orbital geometry. The orbital altitude, 900 km, and inclination, 99°, combined with the Earth's equatorial bulge lead to a precession of the plane of the orbit about 1° per day. As a result, the orbit normal always pointed towards the Sun as the satellite orbited above the Earth's terminator. By pointing the satellite radially away from the Earth, the cold telescope was shielded from the heat loads from the Sun and Earth while providing natural scanning motion across the entire sky in about six months. A sequence of hours-confirming scans on the celestial sphere is also shown. (Adapted from Figure III.B.1, *IRAS* Catalogs and Atlases: Explanatory Supplement 1988.)

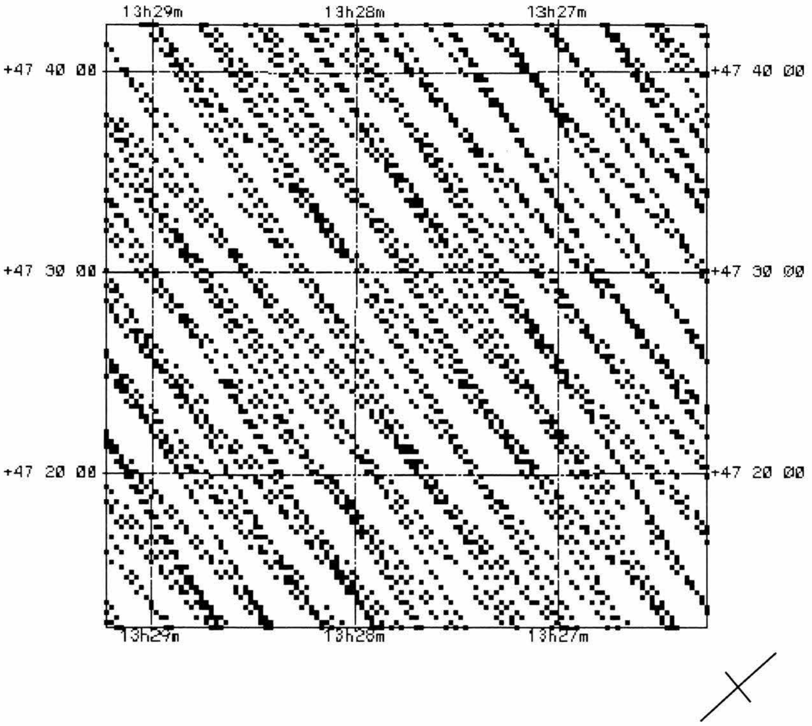

Figure 1.3: *IRAS* scan pattern in M51. Dots represent 60 μm detector footprint center positions. Lower right cross indicates FWHM of the 60 μm detector response function.

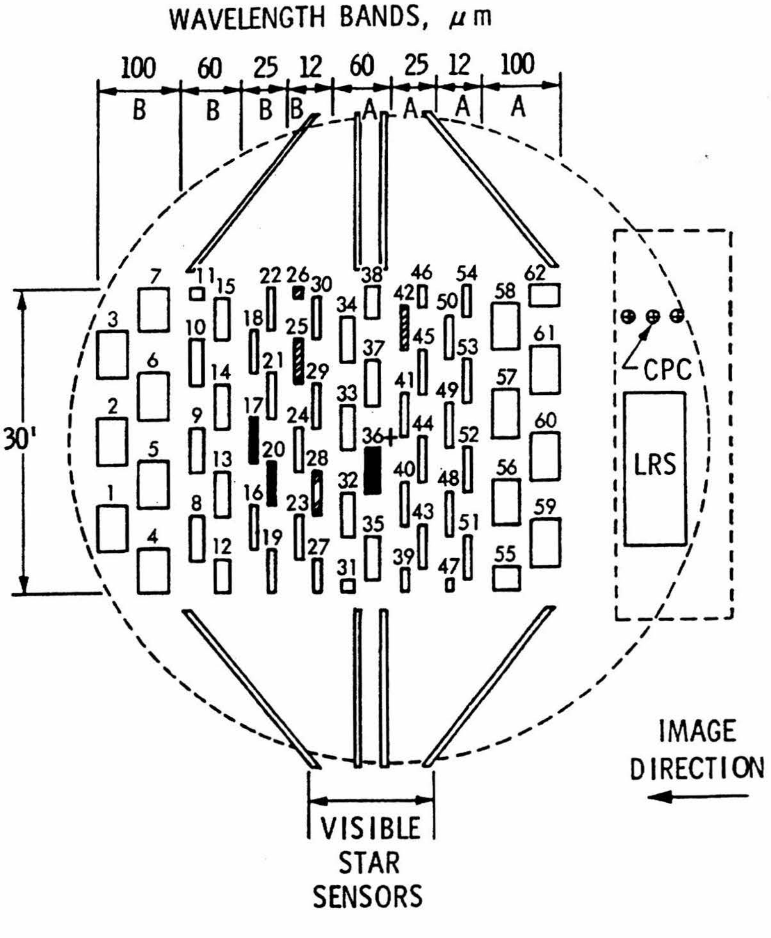

Figure 1.4: The *IRAS* focal plane. The numbered rectangles in the central portion each represent the field of view of a detector, filter and field lens combination. The filled-in detectors were inoperative while the cross-hatched detectors showed degraded performance during the mission. (Adapted from Figure II.C.6, *IRAS* Catalogs and Atlases: Explanatory Supplement 1988.)

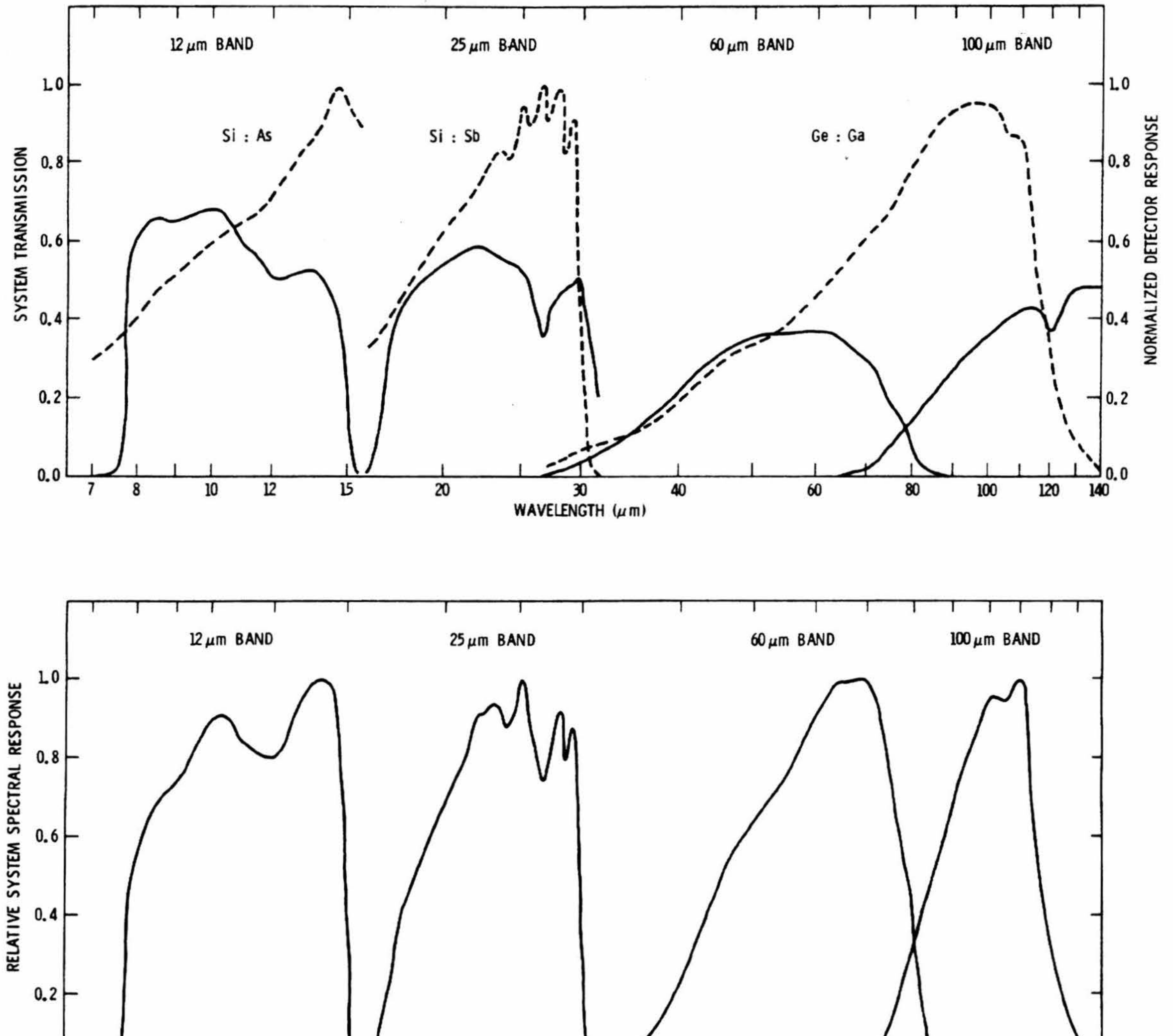

Figure 1.5: (a) Response vs. wavelength of optical components. Solid lines show the transmission of filters and lenses. Dashed lines show relative detector response to constant energy input; (b) Relative system spectral response. (Adapted from Figure II.C.9, *IRAS* Catalogs and Atlases: Explanatory Supplement 1988.)

the telescope. The typical detector sizes were 45 × 267, 45 × 279, 90 × 285, and 180 × 303 arcsec (full width at half maximum response, FWHM) respectively, at the four wavelength bands.

This combination of focal plane, detector size, and scan pattern optimized detection of point sources in areas of the sky where the separation between sources was large compared to the sizes of the detectors. However, it complicates the construction of images of regions containing spatial structure on the scale of arcminutes.

The detailed optical system transmission, detector spectral response and overall relative spectral response for the four infrared bands of *IRAS* are shown in Figure 1.5. The four bands (12, 25, 60, and 100 μm, referred to as band 1, 2, 3, and 4 in *IRAS* terminology) employed Si:As, Si:Sb, Ge:Ga, and Ge:Ga detectors. The high resolution *IRAS* Galaxy Atlas was produced for 60 μm (band 3) and 100 μm (band 4).

1.4 Correlations with Other Surveys

A fundamental use of the *IRAS* Galaxy Atlas will be to correlate the infrared emission with surveys at other wavelengths. In many cases, the $4'$ to $5'$ resolution at 100 μm of the current *IRAS* data is insufficient, and $1'$ is desirable. Examination of some IGA images showed interesting high frequency structure in the diffuse infrared emission (cirrus, Beichman 1987). Also, serious confusion problems in star-forming regions are aided by increased spatial resolution. Two ongoing surveys of the Galactic plane are particularly suitable for comparison, although other surveys exist that can be used as well.

1.4.1 FCRAO CO Survey of the Outer Galaxy

The CO J=1–0 emission is the primary tracer of molecular hydrogen. There are a variety of millimeter wavelength telescopes that provide roughly $1'$ resolution in CO surveys of molecular gas. However, most surveys to date are either sparsely sampled or cover relatively small regions in molecular clouds. Large scale, unbiased surveys are required to determine the distribution of molecular material within the Galaxy. Also, previous CO J=1–0 surveys from the First Quandrant of the Galaxy have been limited by the blending of emission from unrelated clouds due to the rotation of the Galaxy. The FCRAO survey will map a 320 square degree region in the Second Quandrant of the Galactic plane (which is free of cloud blending) in CO J=1–0 at $50''$ angular resolution, using the 15 element focal plane array receiver QUARRY. This direction in the Galaxy also contains several well defined spiral arm features. The survey started in the spring of 1994 and is 70% complete as of June 1996.

CO has been selected for the FCRAO survey to be sensitive to the low column density material that is necessary to define the large scale topology of the molecular gas.

The primary scientific goals of the FCRAO survey are: 1) to determine the large scale topology of the molecular interstellar; 2) to determine the mostly unexplored relationship between the molecular and atomic gas components in the interstellar medium; 3) to investigate the enhancement of molecular gas surface density within spiral arms; 4) to study sites of massive star formation. The study of all these topics can be greatly aided by the ready access to *IRAS* data that trace the dust and luminosity sources, and the H I data that trace the atomic component of the interstellar medium.

Information about the FCRAO survey can be found on the World Wide Web at `http://fcrao1.phast.umass.edu/telescope/2quad.html.` [2]

1.4.2 DRAO H I and Radio Continuum Survey

A project is underway (Normandeau, Taylor, & Dewdney 1997) to use the DRAO Synthesis Telescope to survey the Galactic plane at a resolution of $\sim 1'$ in the $\lambda 21$ cm H I–line and continuum. In addition the survey will contain wider-field, lower resolution images at $\lambda 74$ cm. Surveys of Galactic H I have been done before, but only at spatial resolutions about 100 times worse (in area) than the resolution of the DRAO Synthesis Telescope. The resolution of existing studies is simply too coarse to allow adequate comparison with observations of other important species in the interstellar medium.

Although there is a strong correlation of H I emission with diffuse far-infrared emission, the poor spatial resolution (about $30'$) of most H I surveys has been the limiting factor to improved understanding of the chemical and physical processes underlying this relationship. There is also very strong correlation between the total 21 cm wavelength radio synchrotron emission and far-infrared emission in external galaxies (e.g., Helou, Duric, & Crane 1990). The far-infrared emission is thought to be related to star formation activity while the radio emission is believed to be from cosmic rays associated with supernova remnants. This correlation is also seen in our own Galaxy but tends to break down at the

---

[2] We give references to online resources (mostly in the form of World Wide Web documents) whenever appropriate. The information is accurate as of 1996.

hundred parsec scale in the solar neighborhood (Boulanger & Perault 1988). Again, the lack of high spatial resolution data had been a critical limitation to further progress. A striking correlation between the far-infrared and 21 cm radio continuum emission is discovered through examination of the new IGA and H I data of the W3-5 star forming region, which differs from previous comparisons of far-infrared and radio continuum due to the unprecedented spatial resolution ($\sim 1'$) and sensitivity to large scale structures (Chapter 4 of this thesis).

The DRAO survey home page can be found at `http://www.ras.ucalgary.ca/GPS_pub.html`.

1.5 Selected Science Topics

The 60 and 100 μm *IRAS* Galaxy Atlas images have $1'$ to $2'$ resolution and provide new opportunities to study star formation and the interstellar medium. In addition to the enhanced spatial resolution, zodiacal emission has been subtracted from the data, and striping artifacts are reduced to a negligible level. The images can be mosaicked seamlessly, giving high sensitivity to large structures. Therefore, the IGA images will enable a new class of projects that require both high spatial resolution and large coverage, either for the purpose of large scale surveys or to study samples of intrinsically large objects. We describe below some of the possible science applications using the IGA images.

1.5.1 Structure and Dynamics of the Interstellar Medium

Various aspects of the structure of the interstellar medium (ISM) can be studied with the high resolution data from the *IRAS* Galaxy Atlas. From the *IRAS* 60 and 100 μm data alone, one can examine the power spectrum distribution with spatial frequencies (e.g., Gautier et al. 1992) which turns out to be a power law with index -2.9, consistent with radio measurements taken in H I maps (Green 1993; Crovisier & Dickey 1983). The nearly complete elimination of striping artifacts in the IGA images due to new algorithm development (Section 2.3) is crucial for extending the study to higher spatial resolution, as it frees the spatial frequency distribution from contamination caused by striping signal. This allows one to look for changes in the power law slope at high spatial frequency, such as are expected if there are well-defined intrinsic scales for different turbulent processes within the ISM (Falgarone & Phillips 1990; Larson 1995). This issue became more important as a recent study (Devega, Sanchez, & Combes 1996) suggested that the fractal structure in the ISM could be explained by self-gravity alone, without invoking the turbulence mechanism. While the high resolution *IRAS* maps do not have quite the resolution ($15 - 30''$) of the best millimeter wave studies (Falgarone, Phillips, & Walker 1991; Falgarone 1992), they would be available over thousands of square degrees, and would span a broad range of physical conditions. The IGA data could also be examined with a variety of new mathematical techniques including fractals (Dickman, Horvath, & Margulis 1990; Zimmermann & Stutzki 1992; Beech 1992; Vogelaar & Wakker 1994), wavelets (Langer, Wilson, & Anderson 1993), and morphological filters (Appleton, Siqueira, & Basart 1993) that offer new connections between spatial structure and underlying physical processes.

Joining the forces of the IGA and the new generation H I and CO maps will provide important insight into the dynamics and origin of the ISM structures. The velocity information contained in the line surveys can be used to "deproject" the infrared emission, which comes from dust mixed with both atomic gas (traced by H I) and molecular gas (traced by CO), and from dust in the interface region. The separation of the infrared emission may break up the "apparent" structures and allow the important details to be associated with particular velocity slices in the line survey maps, which may potentially give rise to more reliable identification of various structures and important dynamical information on the ISM.

Analysis of one $8^\circ \times 6^\circ$ pilot field in W3-5 is already in progress (Normandeau, Taylor, & Dewdney 1996; Heyer et al. 1996; Chapter 4 of this thesis). Notably, a strong correlation between the far infrared and radio continuum has been found in the W3-5 region, using the IGA and DRAO survey images. The emission appears to be thermal in nature (dust and ionized gas), therefore, the correlation found is different from the previously found correlation between far-infrared and radio continuum in external galaxies (e.g., Bicay, Helou, & Condon 1989), which is mostly non-thermal. Quantitative models of H II regions can be developed with the aid of the images (e.g., the wind-blown shell powered by the IC-1805 OB cluster). The shell is ionized on the inside, and heated by ultraviolet photons on the outer edge. Also discovered is an extensive faint ionized halo surrounding the shell.

1.5.2 Cloud Core Mass Function in Star Forming Regions

According to our current understanding, active star formation occurs in small subregions of molecular clouds commonly known as *dense cores* (Shu, Adams, & Lizano 1987). These high density regions contain up to $100 M_{\odot}$ of gas and range from $1'$ to $10'$ in size in the nearest molecular clouds (Benson & Myers 1989; Carpenter, Snell, & Schloerb 1995). Roughly half of the dense cores contain embedded infrared sources thought to be protostars (Beichman et al. 1986; Carpenter et al. 1993).

These dense cores are very important to the study of star formation, and various new mapping surveys started to become available in the 1990's (Lada, Bally, & Stark 1991; Tatematsu et al. 1993; Onishi et al. 1996; Launhardt et al. 1996).

Wood, Myers, & Daugherty (1994) identified 255 "*IRAS* cores" in nearby molecular clouds, using co-added images at 60 and 100 μm (which have resolution $2-3$ times lower than the IGA). The clouds were found to be remarkably filamentary, and that the cores are often distributed along the filaments. Carpenter, Snell, & Schloerb (1995) found that the more luminous *IRAS* sources tend to be associated with more massive cores, indicating that more massive cores generally form massive stars. The dense cores measure typically $1'$ or $2'$ at the 500 pc distance of Orion, and nearby molecular clouds such as Orion, Taurus-Auriga, and ρ Ophiuchi also extend over large regions. Therefore, the high spatial resolution large coverage, and superior striping correction provided by the IGA will contribute greatly to future surveys. Also, new techniques have been developed in recent years to subtract the diffuse infrared "background" from the images (Laureijs, Clark, & Prusti 1991; Appleton, Siqueira, & Basart 1993). The desired end result would be a reliable determination of the mass and size distribution of dense cores in several large molecular clouds.

1.5.3 Initial Mass Functions of Massive Stars

Most estimates of the initial distribution of stellar masses are based on volume-limited, *optically* selected star samples in the solar neighborhood (complete to distances of $\sim$ 2 kpc). A variety of proper motion, spectroscopic, and photometric techniques are combined to derive a luminosity function for main sequence stars. Then a main sequence mass-luminosity relationship is applied in order to obtain the present day mass function (PDMF). Next, the effects of stellar evolution are taken into account in order to derive the initial mass function (IMF). Not surprisingly, considerable uncertainty exists in the assumptions commonly made in the different steps, and it seems worthwhile to explore alternative approaches to the subject.

The *IRAS* survey provides a very good way to measure the high-mass star content of giant molecular clouds, even out to the edge of the Galaxy (e.g., Mead, Kutner, & Evans 1990; Carpenter, Snell, & Schloerb 1990; Carpenter, Snell, & Schloerb 1995). Therefore, the *infrared* luminosity function of the youngest (still embedded) stars can be determined, in contrast with the optical luminosity function of older massive stars. Previous works in this direction were limited by source confusion. With higher resolution, one can determine whether the infrared emission came from one or several embedded stars, and measure their relative fluxes. The IGA is particularly suitable for this task, offering data for a large number of sources and addressing the problem of source donfusion at the same time.

1.5.4 Supernova Remnants (SNR)

The number of proposed pulsar/SNR associations has grown dramatically in the 1990s, going from a total of 5 in 1988 to 28 in 1996. This is due in part to *ad hoc* searches (e.g., Wolszczan, Cordes, & Dewey 1991; Kaspi et al. 1992; Frail, Goss, & Whiteoak 1994; Gorham et al. 1996; Kaspi et al. 1996), in part to new pulsar and SNR surveys (e.g., Manchester, D'Amico, & Tuohy 1985; Johnston et al. 1992; Whiteoak & Green 1996), and in part to *a posteriori* cross correlations between pulsar and SNR catalogs (e.g., Manchester et al. 1991; Caraveo 1993). For recent reviews on the subject, see Kaspi (1996) and Frail (1996). However, most of the proposed pulsar/SNR associations require additional investigation before they can be considered secure (Gaensler & Johnston 1995; Kaspi 1996).

The *IRAS* Galaxy Atlas is an ideal tool, both for finding new supernova remnants by examining the vicinity of known young pulsars, and for validating the existing identifications of pulsar/SNR association by providing further morphological evidence for or against the SNR. Young pulsars are population I objects, and the majority lie within 5 degrees latitude of the Galactic plane, which coincides with the latitude range covered by the IGA. As the supernova remnants are warmer than the background diffuse emission (cirrus), their infrared signatures are also distinct (Saken, Fesen, & Shull 1992): young supernova remnants have peak fluxes in the 25 to 60 μm range, while the cirrus is brightest at 100 μm. Therefore, the search would be for extended regions of warm emission with shell-like morphology centered on young pulsars, using, for example, the pulsar catalog of

Taylor, Machester, & Lyne (1993). One will have to be careful about confusion with the dust shells of OB associations (which are much more luminous) if there are nearby massive stars. This study is not possible using the ISSA plates because of the high level of source confusion in the plane and instead requires the enhanced resolution of the HIRES product to reduce confusion (for example, see Figure A.2, which shows the remnant from Tycho's star before and after HIRES processing).

References

Appleton, P. N., Siqueira, P. R., & Basart, J. P. 1993. A morphological filter for removing cirrus-like emission from far-infrared extragalactic *IRAS* fields. *Astron. J.*, **106**, 1664.

Assendorp, R., Bontekoe, T. R., Dejonge, A. R. W., Kester, D. J. M., Roelfsema, P. R., & Wesselius, P. R. 1995. The Gröningen *IRAS* imaging software (IST). *Astron. & Astrophys. Suppl.*, **110**, 395.

Aumann, H. H., Fowler, J. W., & Melnyk, M. 1990. A maximum correlation method for image construction of *IRAS* survey data. *Astron. J.*, **99**, 1674.

Beech, M. 1992. The projection of fractal objects. *Astrophys. & Sp. Sci.*, **192**, 103.

Beichman, C. A., Myers, P. C., Emerson, J. P., Harris, S., Mathieu, R., Benson, P. J., & Jennings, R. E. 1986. Candidate solar-type protostars in nearby molecular cloud cores. *Astrophys. J.*, **307**, 337.

Beichman, C. A. 1987. The *IRAS* view of the Galaxy and the solar-system. *Ann. Rev. Astron. Astrophys.*, **25**, 521.

Beichman, C. A. 1988. The infrared universe revealed by *IRAS*. *Astrophys. L. & Comm.*, **27**, 67.

Benson, P. J. & Myers, P. C. 1989. A survey for dense cores in dark clouds. *Astrophys. J. Suppl.*, **71**, 89.

Bicay, M. D., Helou, G., & Condon, J. J. 1989. The infrared-to-radio ratio within NGC 5236 (M83) and NGC 6946. *Astrophys. J.*, **338**, L53.

Bontekoe, T. R., Kester, D. J. M., Price, S. D., Dejonge, A. R. W., & Wesselius, P. R. 1991. Image construction from the *IRAS* survey. *Astron. & Astrophys.*, **248**, 328.

Bontekoe, T. R., Koper, E., & Kester, D. J. M. 1994. Pyramid maximum-entropy images of *IRAS* survey data. *Astron. & Astrophys.*, **284**, 1037.

Boulanger, F. B. & Perault, M. 1988. Diffuse infrared-emission from the Galaxy. 1. solar neighborhood. *Astrophys. J.*, **330**, 964.

Cao, Y., Prince, T. A., Terebey, S., & Beichman, C. A. 1996. Parallelization and algorithmic enhancements of high resolution *IRAS* image construction. *Pub. Astron. Soc. Pacific*, **108**, 535.

Cao, Y., Terebey, S., Prince, T. A., & Beichman, C. A. 1996. The high resolution *IRAS* Galaxy Atlas. *Astrophys. J. Suppl.*, submitted.

Cao, Y., Eggermont, P. P. B., & Terebey, S. 1996. Cross log entropy maximization and its application to ringing suppression in image reconstruction. *IEEE Trans. Image Proc.*, submitted.

Caraveo, P. A. 1993. Associating young pulsars and supernova-remnants – PSR 1610-50 and the case for high-velocity pulsars. *Astrophys. J.*, **415**, L111.

Carpenter, J. M., Snell, R. L., & Schloerb, F. P. 1990. Molecular clouds associated with luminous far-infrared sources in the outer Galaxy. *Astrophys. J.*, **362**, 147.

Carpenter, J. M., Snell, R. L., Schloerb, F. P., & Skrutskie, M. F. 1993. Embedded star-clusters associated with luminous *IRAS* point sources. *Astrophys. J.*, **407**, 657.

Carpenter, J. M., Snell, R. L., & Schloerb, F. P. 1995. Star-formation in the Gemini OB1 molecular cloud complex. *Astrophys. J.*, **450**, 201.

Clemens, D. P., Yun, J. L., & Heyer, M. H. 1991. Bok globules and small molecular clouds – deep *IRAS* photometry and ^{12}CO spectroscopy. *Astrophys. J. Suppl.*, **75**, 877.

Crovisier, J. & Dickey, J. M. 1983. The spatial power spectrum of Galactic neutral hydrogen from observations of the 21-cm emission-line. *Astron. & Astrophys.*, **122**, 282.

Devega, H. J., Sanchez, N., & Combes, F. 1996. Self-gravity as an explanation of the fractal structure of the interstellar-medium. *Nature*, **383**, 56.

Dickman, R. L., Horvath, M. A., & Margulis, M. 1990. A search for scale-dependent morphology in 5 molecular cloud complexes. *Astrophys. J.*, **365**, 586.

Falgarone, E. & Phillips, T. G. 1990. A signature of the intermittency of interstellar turbulence – the wings of molecular line-profiles. *Astrophys. J.*, **359**, 344.

Falgarone, E., Phillips, T. G., & Walker, C. K. 1991. The edges of molecular clouds – fractal boundaries and density structure. *Astrophys. J.*, **378**, 186.

Falgarone, E. 1992. The structure of quiescent clouds. *IAU Symposia*, **150**, 159.

Fowler, J. W. & Aumann, H. H. 1994. HIRES and beyond. In *Science with High Spatial Resolution Far-Infrared Data*, ed. S. Terebey & J. Mazzarella (Pasadena: JPL 94-5), 1.

Frail, D. A., Goss, W. M., & Whiteoak, J. B. Z. 1994. The radio lifetime of supernova-remnants and the distribution of pulsar velocities at birth. *Astrophys. J.*, **437**, 781.

Frail, D. A. 1996. Pulsar supernova remnant associations. *IAU Symposia*, **165**, 257.

Gaensler, B. M. & Johnston, S. 1995. The pulsar/supernova remnant connection. *Mon. Not. R. Astron. Soc.*, **277**, 1243.

Gorham, P. W., Ray, P. S., Anderson, S. B., Kulkarni, S. R., & Prince, T. A. 1996. A pulsar survey of 18 supernova-remnants. *Astrophys. J.*, **458**, 257.

Gautier, T. N. III, Boulanger, F., Perault, M., & Puget, J.-L. 1992. A calculation of confusion noise due to infrared cirrus. *Astron. J.*, **103**, 1313.

Green, D. A. 1993. A power spectrum analysis of the angular scale of Galactic neutral hydrogen emission towards $l = 140°, b = 0°$. *Mon. Not. R. Astron. Soc.*, **262**, 327.

Helou, G., Duric, N., & Crane, P. (eds.) 1990. *The Interpretation of Modern Synthesis Observations of Spiral Galaxies* (Albuquerque: UNM).

Heyer, M. H., Brunt, C., Snell, R. L., Howe, J., Schloerb, F. P., Carpenter, J. M., Normandeau, M., Taylor, A. R., Dewdney, P. E., Cao, Y., Terebey, S., & Beichman, C. A. 1996. A massive cometary cloud associated with IC-1805. *Astrophys. J.*, **464**, L175.

IRAS Catalogs and Atlases: Explanatory Supplement 1988. Beichman, C. A., Neugebauer, G., Habing, H. J., Clegg, P. E., & Chester, T. J. (eds.) (Washington, DC: GPO).

IRAS Sky Survey Atlas Explanatory Supplement 1994. Wheelock, S. L., Gautier, T. N., Chillemi, J., Kester, D., McCallon, H., Oken, C., White, J., Gregorich, D., Boulanger, F., Good, J. and Chester, T. (Pasadena: JPL 94-11).

Johnston, S., Lyne, A. G., Manchester, R. N., Kniffen, D. A., D'Amico, N., Lim, J., & Ashworth, M. 1992. A high-frequency survey of the southern Galactic plane for pulsars. *Mon. Not. R. Astron. Soc.*, **255**, 401.

Kaspi, V. M., Manchester, R. N., Johnston, S., Lyne, A. G., & D'Amico, N. 1992. PSR J1341-6220 – a young pulsar in a supernova remnant. *Astrophys. J.*, **399**, L155.

Kaspi, V. M., Manchester, R. N., Johnston, S., Lyne, A. G., & D'Amico, N. 1996. A search for radio pulsars in southern supernova remnants. *Astron. J.*, **111**, 2028.

Kaspi, V. M. 1996. Pulsar/supernova remnant associations. *IAU Colloq.*, **160**, in press.

Lada, E. A., Bally, J., & Stark, A. A. 1991. An unbiased survey for dense cores in the Lynds 1630 molecular cloud. *Astrophys. J.*, **368**, 432.

Langer, W. D., Wilson, R. W., & Anderson, C. H. 1993. Hierarchical structure analysis of interstellar clouds using nonorthogonal wavelets. *Astrophys. J.*, **408**, L45.

Larson, R. B. 1995. Star-formation in groups. *Mon. Not. R. Astron. Soc.*, **272**, 213.

Launhardt, R., Mezger, P. G., Haslam, C. G. T., Kreysa, E., Lemke, R., Sievers, A., & Zylka, R. 1996. Dust emission from star-forming regions. 4. dense cores in the Orion B molecular cloud. *Astron. & Astrophys.*, **312**, 569.

Laureijs, R. J., Clark, F. O., & Prusti, T. 1991. *IRAS* detection of very cold dust in the Lynds 134 cloud complex. *Astrophys. J.*, **372**, 185.

Manchester, R. N., D'Amico, N., & Tuohy, I. R. 1985. A search for short-period pulsars. *Mon. Not. R. Astron. Soc.*, **212**, 975.

Manchester, R. N., Kaspi, V. M., Johnston, S., Lyne, A. G., & D'Amico, N. 1991. PSR 1758-24 and G5.4–1.2, a remarkable pulsar supernova remnant association. *Mon. Not. R. Astron. Soc.*, **253**, P7.

Martin, P. G., Rogers, C., Reach, W. T., Dewdney, P. E., & Heiles, C. E. 1994. Arcminute scale H I and *IRAS* observations toward high latitude cloud G86.5+59.6. In *Science with High Spatial Resolution Far-Infrared Data*, ed. S. Terebey & J. Mazzarella (Pasadena: JPL 94-5), 165.

Mead, K. N., Kutner, M. L., & Evans, N. J. 1990. Molecular clouds in the outer Galaxy. 4. Studies of star formation. *Astrophys. J.*, **354**, 492.

Normandeau, M., Taylor, A. R., & Dewdney, P. E. 1996. A Galactic chimney in the Perseus arm of the Milky Way. *Nature*, **380**, 687.

Normandeau, M., Taylor, A. R., & Dewdney, P. E. 1997. The Dominion Radio Astrophysical Observatory Galactic plane survey pilot project: the W3/4/5/HB3 region. *Astrophys. J. Suppl.*, **108**, 279.

Onishi, T., Mizuno, A., Kawamura, A., Ogawa, H, & Fukui, Y. 1996. A $C^{18}O$ survey of dense cloud cores in Taurus – core properties. *Astrophys. J.*, **465**, 815.

Rice, W. 1993. An atlas of high-resolution *IRAS* maps of nearby galaxies. *Astron. J.*, **105**, 67.

Saken, J. M., Fesen, R. A., & Shull, J. M. 1992. An *IRAS* survey of Galactic supernova remnants. *Astrophys. J. Suppl.*, **81**, 715.

Scoville, N. Z., & Good, J. C. 1989. The far-infrared luminosity of molecular clouds in the Galaxy. *Astrophys. J.*, **339**, 149.

Shu, F. H., Adams, F. C., & Lizano, S. 1987. Star formation in molecular clouds – observation and theory. *Ann. Rev. Astron. Astrophys.*, **25**, 23.

Snell, R. L., Heyer, M. H., & Schloerb, F. P. 1989. Comparison of the far-infrared and carbon-monoxide emission in Heiles Cloud-2 and B18. *Astrophys. J.*, **337**, 739.

Sodroski, T. J., Dwek, E., Hauser, M. G., & Kerr, F. J. 1989. Large-scale Galactic dust morphology and physical conditions from *IRAS* observations. *Astrophys. J.*, **336**, 762.

Soifer, B. T., Houck, J. R., & Neugebauer, G. 1987. The *IRAS* view of the extragalactic sky. *Ann. Rev. Astron. Astrophys.*, **25**, 187.

Surace, J. A., Mazzarella, J. M., Soifer, B. T., & Wehrle, A. E. 1993. High-resolution *IRAS* observations of interacting systems in the *IRAS* bright galaxy sample. *Astron. J.*, **105**, 864.

Tatematsu, K., Umemoto, T., Kameya, O., Hirano, N., Hasegawa, T., Hayashi, M., Iwata, T., Kaifu, N., Mikami, H. et al. 1993. Molecular cloud cores in the Orion A cloud. 1. Nobeyama CS (1–0) survey. *Astrophys. J.*, **404**, 643.

Taylor, J. H., Machester, R. N., & Lyne, A. G. 1993. Catalog of 558 pulsars. *Astrophys. J. Suppl.*, **88**, 529.

Terebey, S. & Fich, M. 1986. The correlation in the *IRAS* infrared cirrus and neutral atomic-hydrogen in the outer Galaxy. *Astrophys. J.*, **309**, L73.

Terebey, S. & Mazzarella, J. (eds.) 1994. *Science with High Spatial Resolution Far-Infrared Data* (Pasadena: JPL 94-5).

Vogelaar, M. G. R. & Wakker, B. P. 1994. Measuring the fractal structure of interstellar clouds. *Astron. & Astrophys.*, **291**, 557.

Weiland, J. L., Blitz, L., Dwek, E., Hauser, M. G., Magnani, L., & Richard, L. J. 1986. Infrared cirrus and high-latitude molecular clouds. *Astrophys. J.*, **306**, L101.

Whiteoak, J. B. Z. & Green, A. J. 1996. The MOST supernova remnant catalogue (MSC). *Astron. & Astrophys. Suppl.*, **118**, 329.

Wolszczan, A., Cordes, J. M., & Dewey, R. J. 1991. Discovery of a young, 267 millisecond pulsar in the supernova remnant W44. *Astrophys. J.*, **372**, L99.

Wood, D. O. S., Myers, P. C., and Daugherty, D. A. 1994. *IRAS* images of nearby dark clouds. *Astrophys. J. Suppl.*, **95**, 457.

Zimmermann, T. & Stutzki, J. 1992. The fractal appearance of interstellar clouds. *Physica* A, **191**, 79.

Chapter 2

Algorithm [*]

2.1 The Maximum Correlation Method (MCM)

Starting from a model of the sky flux distribution, the HIRES MCM algorithm folds the model through the *IRAS* detector responses, compares the result track-by-track [1] to the observed flux, and calculates corrections to the model. One important characteristic is that the standard MCM algorithm conserves flux. The process is taken through about 20 iterations in a tradeoff between speed of processing and artifact development versus spatial resolution. The algorithm yields a resolution of approximately $1'$ at 60 μm. This represents an improvement in resolution by as much as a factor of 20 in solid angle over the previous images from the *IRAS* Full Resolution Survey Co-adder (FRESCO). We give a brief description of the MCM algorithm following the formalism and notations of Aumann, Fowler, & Melnyk (1990).

Given an image grid f_j, with n pixels $j = 1, ..., n$ and m detector samples (*footprints*) with fluxes $D_i : i = 1, \ldots, m$, whose centers are contained in the image grid, an image can be constructed iteratively from a zeroth estimate of the image, $f_j^0 = \text{const.} > 0$ for all j. In other words the initial guess is a uniform, flat, and positive definite map. The exact value of the initial image intensity f_j^0 is insignificant and canceled out in the first iteration (the first iteration image being the response function weighted co-add of the detector

---

[*] Adapted (except Sections 2.2 and 2.4.2) with changes from "Parallelization and Algorithmic Enhancements of High Resolution *IRAS* Image Construction" in *The Publications of the Astronomical Society of the Pacific*, **108**, 535–544 (1996 June), by Y. Cao, T. A. Prince, S. Terebey, & C. A. Beichman. Used by permission of the authors. © 1996 by the Astronomical Society of the Pacific.

[1] Track, also called *leg* or *scanline*, refers to the set of data samples collected consecutively by one detector moving across a given field.

data and therefore uniquely determined by the data). For each footprint, a correction factor C_i is computed as

$$\begin{aligned} C_i &= D_i/F_i, \\ i &= 1,\ldots,m, \end{aligned} \tag{2.1}$$

where

$$\begin{aligned} F_i &= \sum_j r_{ij} f_j, \\ i &= 1,\ldots,m, \end{aligned} \tag{2.2}$$

and r_{ij} is the value of the ith footprint's response function at image pixels f_j. Therefore, F_i is the current estimate of the ith footprint's flux, given image grid f_j.

A mean correction factor for the jth image pixel is computed by projecting the correction factor for the footprints into the image domain:

$$\begin{aligned} c_j &= \left[\sum_{i=1}^{m} (r_{ij}/\sigma_i^2) C_i\right] / \left[\sum_{i=1}^{m} (r_{ij}/\sigma_i^2)\right], \\ j &= 1,\ldots,n. \end{aligned} \tag{2.3}$$

The weight attached to the ith correction factor for the jth pixel is r_{ij}/σ_i^2, where σ_i is the *a priori* noise assigned to the ith footprint. Typically, $sigma_i$ is assumed to be the same for all footprints in the same scan line, and is estimated through the scatter of fluxes of detector samples covering the low intensity (background) regions of the image. The $1/\sigma_i^2$ factor in the correction factor weighting represents an attempt to incorporate the Gaussian noise in the footprint flux. [2]

In practice when the footprint noise σ_i is not easily estimated, an equal noise value for all footprints is assumed, and the MCM is identical to the Richardson-Lucy algorithm (Richardson 1972; Lucy 1974).

The $k+1$th estimate of the image is computed by

$$\begin{aligned} f_j^{(k+1)} &= f_j^{(k)} c_j^{(k)}, \\ j &= 1,\ldots,n. \end{aligned} \tag{2.4}$$

---

[2] For a more mathematically rigorous method to combine Poisson and Gaussian noise in the iterative scheme, see Snyder (1990) and Snyder et al. (1995). When the Gaussian noise is dominant, the *image space reconstruction algorithm* (ISRA, Daube-Witherspoon & Muehllehner 1986) is suitable for least squares estimate. It can also be easily extended to incorporate different noise values in the footprints (see Section 2.4.2).

The process is carried to 20 iterations, after which time noise and artifacts limit further resolution enhancement. However, for strong extended sources further iterations are often beneficial (Rice 1993; Hurt & Barsony 1996).

2.2 The Richardson-Lucy Algorithm

For the standard HIRES processing at IPAC, the MCM algorithm is used with equal noise value assigned to all footprints. Therefore, the process is equivalent to the well-known Richardson-Lucy algorithm, of which we take a short excursion to discuss the history and properties.

2.2.1 The Algorithm

The Richardson-Lucy algorithm can be derived formally as follows: Assuming the noise process is Poisson (due to photon counting statistics), the likelihood of the data D_i occuring given an estimate of the image f_j is,

$$P = \prod_{i=1}^{m} \frac{e^{-F_i} F_i^{D_i}}{D_i!}, \tag{2.5}$$

and under Stirling's approximation

$$\begin{aligned} \ln P &= \ln \prod_{i=1}^{m} \frac{e^{-F_i} F_i^{D_i}}{D_i!} \\ &= \sum_{i=1}^{m} \left(D_i - F_i + D_i \ln \frac{F_i}{D_i} \right). \end{aligned} \tag{2.6}$$

To maximize the likelihood P with an estimate of f_j, we set the formal derivative $\partial \ln P / \partial f_j$ to zero

$$\begin{aligned} \frac{\partial \ln P}{\partial f_j} &= \frac{\partial}{\partial f_j} \sum_{i=1}^{m} (D_i - F_i + D_i \ln F_i - D_i \ln D_i) \\ &= \sum_{i=1}^{m} (-r_{ij} + r_{ij} D_i / F_i) \\ &= 0, \\ j &= 1, \ldots, n. \end{aligned} \tag{2.7}$$

From this an iterative algorithm can be built (Lucy 1974),

$$f_j^{(k+1)} = f_j^{(k)} c_j^{(k)},$$

$$j = 1, \ldots, n. \tag{2.8}$$

where

$$\begin{aligned} c_j &= \left[\sum_{i=1}^{m} r_{ij} C_i\right] / \left[\sum_{i=1}^{m} r_{ij}\right] \\ &= \left[\sum_{i=1}^{m} r_{ij} D_i / F_i\right] / \left[\sum_{i=1}^{m} r_{ij}\right], \\ j &= 1, \ldots, n. \end{aligned} \tag{2.9}$$

Usually, the process is started from a uniform image $f_1^0 = f_2^0 = f_j^0$ for all j.

The above derivation, although crude and lacking mathematical rigor, is helpful for understanding the rationale of Poisson likelihood maximization of the algorithm.

2.2.2 Discussion

The Richardson-Lucy algorithm has been derived independently several times, both in the field of astronomical image reconstruction and in medical imaging (more specifically, in positron emission tomography, or PET, see Ter-Pogossian, Raichle, & Sobel 1980). In 1972, Richardson gave the first derivation of the algorithm, using arguments based on the Bayes theorem. Lucy arrived at the formalism in 1974 and pointed to the fact that the Poisson likelihood (of the data occurring given the estimated image) always increases when applying a small fraction of the correction steps. The seminal paper by Shepp & Vardi (1982) proposed the algorithm once again, after building a physical model of the PET process from which the iterative procedure arised. Shepp and Vardi's work also showed the algorithm converges to a maximum likelihood estimate when applying the full correction, [3] by casting the algorithm in the more general framework of Expectation-Maximization (EM, by which the image reconstruction algorithm itself is referred to in medical imaging) algorithms, for which convergence properties were well established (Dempster, Laird, & Rubin 1977). And once again in 1984, Lange and Carson achieved the same maximum likelihood model for PET following a similar path (but independently). At IPAC, Aumann, Fowler, & Melnyk (1990) invented the MCM algorithm for *IRAS* data, and referred to some earlier work by Meinel (1986).

The above history attests to the simplicity and power of the algorithm. Despite the common problems associated with maximum likelihood approaches (most notably, noise

---

[3] For more complete treatments of the algorithm's convergence, see Vardi, Shepp, & Kaufman (1985); Wu (1983).

caused by overfitting the data), the Richardson-Lucy algorithm has the nice property of local flux conservation, which makes it particularly attractive in astronomical applications where photometric integrity is a concern:

$$\sum_{i=1}^{m} F_i^{(k+1)} = \sum_{i=1}^{m} F_i^{(k)}. \tag{2.10}$$

Therefore, when the coverage of the field is uniform, flux is conserved exactly from one iteration to the next.

The Richardson-Lucy algorithm played an important role in the restoration efforts of pre-servicing mission *Hubble Space Telescope* images, which suffered from spherical aberration in the primary mirror (White & Allen 1990; Hanisch & White 1994b; Hanisch & White 1994a). Hanisch & White (1994a) also suggested the restoration algorithms already developed would be very useful for removing the remaining diffraction features and optimizing dynamic range in post-servicing mission data.

When reconstructing images using the Richardson-Lucy iteration, the images become very noisy after a certain number of iterations. This is due to the unconstrained nature of the maximum likelihood estimate and the ill-posed nature of the image reconstruction problem. Two principal solutions have been proposed: 1) regularization of the maximum likelihood estimate and 2) halting the iterative process before deterioration occurs.

One way to regularize the image reconstruction problem is to use penalty terms based on Bayesian considerations, where the penalty term is related to the prior probability of the image, and the resultant image is often called the maximum *a posteriori* (MAP) estimate. Found in the literature are entropy prior (Núñez & Llacer 1990), Gaussian prior (Levitan & Herman 1987), Gibbs prior (Geman & McClure 1987), and spatial autoregressions (Molina et al. 1992). Another method of regularization employs the so-called *sieves* (Snyder & Miller 1985; Snyder et al. 1987). With this method, an estimate is sought not for f_j but, rather, a blurred version $\phi_{j'} = \sum_j \rho_{jj'} f_j$. Here $\rho_{jj'}$ is a resolution kernel that is selected by the user, a natural choice of which would be the diffraction-limited PSF.

The simplest stopping rule is to choose the image with an acceptable χ^2, but estimating the effective number of degrees of freedom is non-trivial. Stopping rules have been proposed based on statistical hypothesis testing, or *feasibility* of the image (Veklerov & Llacer 1987; Llacer & Veklerov 1989). A more recent approach is cross validation, which involves splitting the data set into two or more subsets, using one set to determine some characteristics of the data, and another to verify the characteristics (Núñez & Llacer 1993; Perry & Reeves 1994).

Other techniques to reduce noise in the image include damping the cost function at low fluxes (White 1994), and multi-resolution restoration using wavelet methods (Starck & Murtagh 1994).

For HIRES processing of *IRAS* data, the process is stopped at 20 iterations by default, which resulted primarily from visual quality assessment of the images.

As the standard Richardson-Lucy algorithm is only suitable for maximizing the Poisson likelihood, enhancements were developed to incorporate Gaussian read-out noise (Snyder 1990; Snyder et al. 1995). Faisal et al. (1995) also implemented Snyder's method on the DEC mpp 12000 Sx/Model 200 massively parallel computer. When the Gaussian noise is predominant, the image space reconstruction algorithm (ISRA, Daube-Witherspoon & Muehllehner 1986) has been suggested for least-squares estimate (subject to positivity constraint). ISRA and Richardson-Lucy are not only structurally similar, but can also be derived from the same mathematical framework (De Pierro 1993). As we shall see in Section 2.4, the unification of ISRA and Richardson-Lucy gave birth to another algorithm (also in the same framework), which turned out to be effective in suppressing ringing artifacts around bright point sources.

2.3 Destriping Algorithm

Stripes are the most prominent artifacts of the HIRES images. HIRES takes in the *IRAS* detector data, and if not perfectly calibrated, would try to fit the gain differences in the detectors by a striped image. The striping builds up in amplitude and sharpness along with the HIRES iterations, as the algorithm refines the "resolution" of the stripes (see Figure 2.2(a) and (b)).

The IPAC program LAUNDR (Fowler & Melnyk 1990) invokes several one dimensional flat fielding and deglitching techniques. The basic algorithm applied clamps the background of different scan lines (taken as a low percentile in detector flux histogram for each scan line) to a common level. For the purpose of destriping, the one dimensional algorithm works well for regions with a well-defined baseline, but the result is not satisfactory for regions where structure exists in all spatial frequencies.

2.3.1 Destriping with Uniform Offset Compensation

Our approach combines the image reconstruction and the destriping process. Since the striping gets amplified through the iterations, the idea of applying constraints to the correction factors is natural.

We will incorporate the estimation of leg offsets with image construction, i.e., we will first try to maximize the likelihood function by choosing proper offsets for the legs, then proceed to compute the correction factors from the modified detector data.

Additive Offset Compensation

Assume footprints in the same leg L suffer from the same unknown additive (baseline) offset O_L, then

$$D_i^* = D_i - O_L \tag{2.11}$$

is the "true" detector flux, had the detector baseline been perfectly calibrated. The O_L's can be seen as extra parameters to be estimated, besides the image pixels f_j. Under a Poisson framework, the likelihood function becomes

$$P = \prod_{i=1}^{m} \frac{e^{-F_i} F_i^{D_i - O_L}}{(D_i - O_L)!}. \tag{2.12}$$

Maximizing P with choice of O_L leads to

$$\begin{aligned} \frac{\partial \ln P}{\partial O_L} &= \frac{\partial}{\partial O_L} \sum_{i \in L} [-F_i + (D_i - O_L) \ln F_i (D_i - O_L) \ln (D_i - O_L) + (D_i - O_L)] \\ &= \sum_{i \in L} [-\ln F_i + \ln (D_i - O_L)] \\ &= 0. \end{aligned} \tag{2.13}$$

So we have

$$\prod_{i \in L} \frac{D_i - O_L}{F_i} = \prod_{i \in L} C_i^* = 1, \tag{2.14}$$

in which $C_i^* = D_i^* / F_i$ is the correction factor calculated from offset compensated detector data. This polynomial equation in O_L can be solved with Newton's method. The offsets O_L are computed starting from the second iteration, since in the first iteration $F_i^0 = \sum_j r_{ij} f_j^0 =$ const. and there's no reason to regard it as an approximation of the true F_i.

Multiplicative Offset (Gain) Compensation

Due to calibration error in detector gain, the unknown offset could be multiplicative in nature. In this case $D_i^* = G_L D_i$ and $\partial \ln P / \partial G_L = 0$ gives

$$\sum_{i \in L} D_i \ln \frac{F_i}{G_L D_i} = 0, \tag{2.15}$$

or equivalently

$$\prod_{i \in L} \left(\frac{G_L D_i}{F_i} \right)^{D_i} = \prod_{i \in L} (C_i^*)^{D_i} = 1 \tag{2.16}$$

in which C_i^* is the gain compensated correction factor. C_i^* is then used in place of C_i in Equation (2.3) to compute the pixel correction factors. A new set of G_L is estimated for every MCM iteration.

This choice of the unknown gain offset G_L minimizes the mutual information between the sets D_i^* and F_i in the leg, i.e., the resulting correction factors C_i^* will extract the minimum amount of information from the stream D_i^*. From the viewpoint of the maximum entropy principle, this is the most reasonable choice.

From another point of view, this strategy works because the procedure of averaging C_i's to get c_j has a smoothing effect on the image, so that the image f_j and estimated flux F_i do not contain as much striping power as the footprints D_i.

Offset compensation schemes, both additive and multiplicative, have been tried on *IRAS* test fields. Although a simple statistical test indicated multiplicative offset was a more accurate representation of the effect (Cao & Prince 1994), the results did not show significant difference in image quality. In addition, one type of preprocessing method (in LAUNDR) subtracts the additive baseline from all detector data (which invalidates the assumption that different scan lines differ by gain offsets only), it was decided that the production software uses additive offsets.

2.3.2 Destriping with Local Gain Compensation

A further complication lies in the fact that the assumption of a uniform gain offset in a certain leg is only approximately true. Various hysteresis effects (see Chapter IV of *IRAS* Catalogs and Atlases: Explanatory Supplement 1988) cause the gain to drift slightly within the 1° range. A more aggressive form of the destriping algorithm estimates the gain offset locally as the weighted geometric mean of the correction factors for nearby footprints, so the estimated gain correction for each footprint varies slowly along the leg. The local gain offset is compared to the global one estimated from the entire leg, and if they differ by more than 10% then the global value is used, since the gain is not expected to drift that much over a 1° scale, and the variation in computed offset average is most likely due to real local structure. We used an averaging length of $10'$ to estimate the local offset. Because it is larger than the spatial resolution of the first iteration image ($5'$), it is safe to refer the average correction factor on that scale as due to gain offset. The $10'$ length scale is also small enough to capture the drifting behavior of the gain, as shown by visual inspection of both the output images and their Fourier power spectra. Unlike the standard HIRES algorithm (in which stripes are amplified throughout the iterations), the local gain compensation decreases the striping power monotonically to a negligible level after roughly 10 iterations.

One aspect of the local gain compensation method is that the computed correction factors can cause the flux scale to drift slightly. This is solved by requiring an occasional iteration using the standard MCM algorithm to enforce flux conservation. In practice a standard MCM iteration performed at 10 and 20 iterations produced no noticeable re-introduction of stripes.

2.3.3 Validation of Gain Offset Recovery

To verify the gain offset estimation, a test trying to recover artificially introduced offsets was carried out. A stripe free image was used to generate a set of simulated detector data, and Gaussian-generated gain offsets (uniform within each scan line) were applied to the legs. This set of data was fed to the uniform gain offset compensation program, and a scatter plot of the recovered vs. introduced offsets is shown in Figure 2.1.

The introduced offsets are Gaussian with standard deviation 0.12. The standard deviation of residual offset after compensating for estimated offset is 0.024, indicating a factor of 5 reduction in striping amplitude (25 in power).

The reconstructed image is stripe free and visually indistinguishable from the input image. This suggests that the uniform gain compensation is capable of its designed goals, and that the residual striping seen in the real data (Figure 2.2c) is in fact due to small gain variations within the legs, lending support to the local gain compensation method.

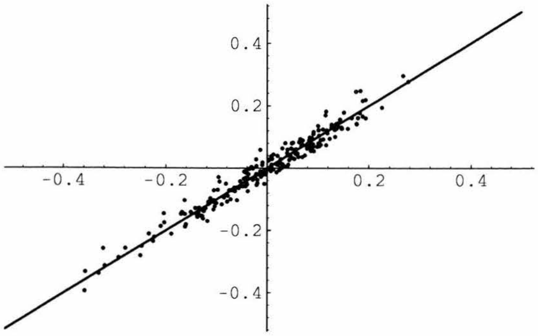

Figure 2.1: Recovery of artificially introduced offsets. vertical: log of recovered gain offset; horizontal: log of introduced gain offset.

2.3.4 Results of the Destriping Algorithm

Figure 2.2 demonstrates the striking effect of the destriping algorithm. Figure 2.2(a) shows the first iteration (FRESCO) image for a 1° × 1° field in ρ Ophiuchi, which is smooth (blurry). Figure 2.2(b) is the 20th iteration image of the field obtained with the standard HIRES algorithm, and is contaminated with strong striping artifacts. A tremendous improvement is seen in Figure 2.2(c) which is produced with uniform gain compensation, although some weak stripes are still visible. Finally, using the local gain compensation method gives a stripe-free image, Figure 2.2(d). It is also apparent that Figure 2.2(d) contains many high spatial frequency features that are absent in 2.2(a).

Local additive offset compensation was used for destriping after rigorous testing (Cao et al. 1996a; Section 3.5) when producing the *IRAS* Galaxy Atlas, and the program was delivered to IPAC as part of the HIRES production software in Spring of 1996. As a result, all HIRES products requested from IPAC using YORIC version 2.00 and higher should be virtually stripe-free.

2.4 Ringing Suppression

For many astronomical image reconstruction problems, ringing around bright point sources is a prominent artifact when there is a non-zero background. In Fourier language, the reconstruction process tries to make the image agree with the true scene in the low spatial frequency components (data constraint), without access to the infinitely high spatial frequencies inherent in the point source scene. The result is known as the Gibbs ringing.

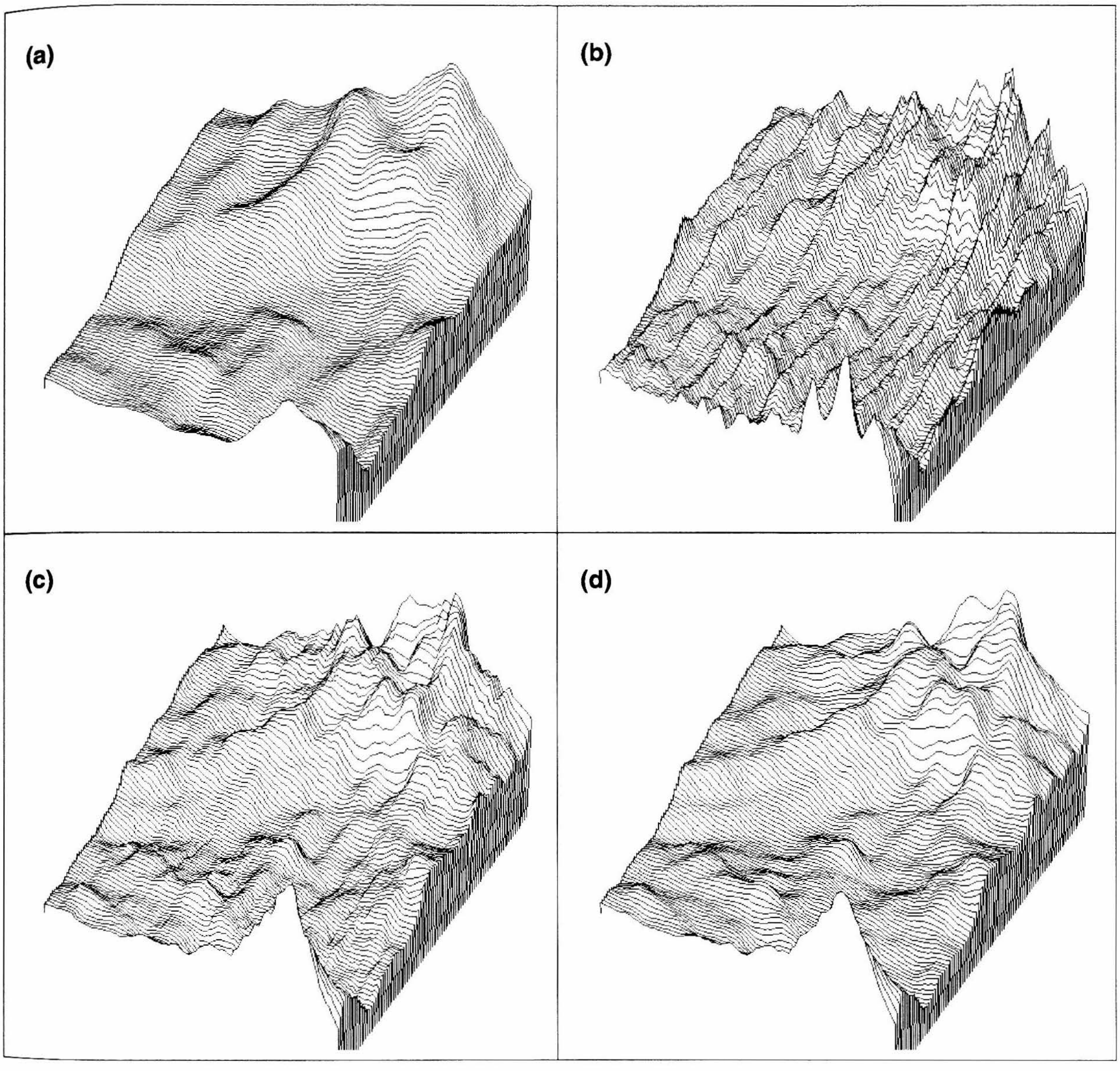

Figure 2.2: Demonstration of the destriping algorithm. (a). 1st iteration image for a field in ρ Ophiuchi(100 μm band); (b). 20th iteration, standard HIRES; (c). 20th iteration, with uniform gain compensation; (d). 20th iteration, with local gain compensation. Size of image is 1° × 1°. Height of surface represents flux.

Astronomical images are often taken with the intent of making photometric measurements of objects in the field. The ringing artifact hinders the increase of photometric accuracy with smaller aperture, and numerous approaches have been tried in the field of astronomical image reconstruction to overcome the difficulty.

The majority of the approaches found in the literature have all involved separation of the data into components (or channels) that represent the different spatial scales, i.e., smooth extended emission and point source.

The most natural way is to reconstruct the point sources (e.g., using the CLEAN algorithm) and remove them from the data before using methods like Richardson-Lucy or maximum entropy to reconstruct the extended emission. This method employs different algorithms suitable for different components of the image and was suggested for image restorations from the pre-servicing *Hubble Space Telescope* data (Meier 1990).

Another method, which seeks to inject the necessary amount of high spatial frequency signal into the image by planting point sources in the starting image for iterative algorithms like Richardson-Lucy (thus reducing the misfit between model and data), has been developed and applied by several authors (Fowler & Aumann 1994; Lucy 1994). Both Fowler's and Lucy's schemes require the prior knowledge of the exact location of the point source. Since the separation of the data into two channels is not unique, Fowler's method also requires knowledge of the relative strength of the point source compared to the background emission, while Lucy's deals with the problem by imposing regularization (smoothness constraint) on the background emission channel.

In the regime of maximum entropy image reconstruction (Burch, Gull, & Skilling 1983; Skilling & Bryan 1984; Skilling & Gull 1985; Skilling 1986a; Skilling 1986b), the ringing problem is also severe as the entropy regularization favors flatter images. When it comes to photometry measurement, the flux of the point source was found to be biased by approximately one sigma (e.g., see Weir & Djorgovski 1990 and the references therein). The intrinsic correlation function (ICF) method was developed to introduce spatial correlation into the reconstructed image (Gull 1989). [4] Using a single-channel ICF was found to result in marginal improvements for *IRAS* images, and that ringing effects persist around bright point sources, the extent of which scales with the width of the ICF (Bontekoe et al. 1994).

---

[4] We note the similarity between the ICF method and the method of sieves introduced for Richardson-Lucy (see Section 2.2), both aimed at regularization of the image using spatial correlation. Furthermore, Gull's method featured Bayesian justification and parameter determination, while Veklerov & Llacer (1990) incorporated (frequentist) statistical hypothesis testing into the method of sieves.

Methods using more than one correlation lengths were developed, including the multichannel ICF method (Weir & Djorgovski 1990) and pyramid maximum entropy (Bontekoe et al. 1994), the latter approach reporting good ringing suppression and a moderate increase in computational cost.

This section describes our effort of new ringing suppression schemes, the expectation being that the method is suitable for large scale processing as the IGA. The purpose posed several constraints: 1) the increase in computational cost should be small (compared to MCM); 2) the algorithm should not require extra prior knowledge (source strength and position) as input; and 3) it should include as few tunable parameters as possible. Also, the method should give images with good photometric accuracy. These constraints excluded almost all the methods already available. But as we shall see, the cross log entropy maximization presented in Section 2.4.2 satisfies all of these requirements.

2.4.1 Log Entropy MART [5]

Tutorial

The discussion presented here is related to and has been inspired by the critique of maximum entropy methods in Narayan (1986) and Press et al. (1992), pp. 818-826.

Among the various regularization functionals for image reconstruction is the *Burg entropy* or *log entropy*:

$$S = \sum_{j=1}^{n} \ln(f_j/U), \tag{2.17}$$

where

$$U = \sum_{j=1}^{n} f_j \tag{2.18}$$

is the total flux in the image.

Using the Burg entropy as the regularization term, the problem becomes

$$\text{maximize} - F = \ln P + \lambda S. \tag{2.19}$$

where λ is a Langrange multiplier. In the language of statistical mechanics, F corresponds to the system's Helmholtz free energy, $-\ln P$ the internal energy, λ the temperature, and S – naturally – the entropy. The goal then is to evolve the system and minimize the Helmholtz free energy F.

---

[5] Multiplicative Algebraic Reconstruction Technique.

The noiseless, exact data constraint case (solving for image f_j which gives the data D_i exactly) corresponds to a "cold" system, or zero temperature λ. In this case the $\ln P$ term can be replaced with a set of linear constraints, each with its own Lagrange multiplier (cf. Press et al. 1992, p. 822):

$$\text{maximize} \quad \sum_{i=1}^{m} \lambda_i [D_i - \sum_{j=1}^{n} r_{ij} f_j] + S. \tag{2.20}$$

Let $\bar{f} = U/n$, and set the formal derivative with respect to f_j to zero:

$$\frac{\partial S}{\partial f_j} = f_j^{-1} - \bar{f}^{-1} = \sum_{i=1}^{m} \lambda_i r_{ij}, \tag{2.21}$$

which can be rewritten as

$$f_j^{-1} = \bar{f}^{-1} + \sum_{i=1}^{m} \lambda_i r_{ij}. \tag{2.22}$$

The above equation tells us the inverse of the solution (f_j^{-1}) is a linear combination of a constant ($\bar{f}^{-1}$) and the response function grids (r_{ij}).

Now we can have a heuristic explanation why the maximum Burg entropy solution is effective in reducing ringing. Suppose the true underlying image consists of a uniform background of intensity 1, and a point source of magnitude M. Using linear regularization (i.e., the regularization functional is the Euclidean norm of the image f_j) gives the so-called *principal solution* (Press et al. 1992, p. 806), which can be thought of being obtained by adding up the response function grids (principal solution contains *only* linear combination of the response functions, Press et al. 1992, p. 806). Now the response functions r_{ij} have supports of finite width, and adding them up to achieve a distribution that satisfies the data constraint would naturally lead to ripples around the point source position. Also, the Lagrange multiplier λ_i for a data point i at the point source position scales linearly with the point source strength M, and the scaling provides a measure of how "difficult" it is to reconstruct a bright point source.

The maximum Shannon entropy solution, on the other hand, is achieved by constructing the $\ln f_j$ map with a linear combination of the response functions r_{ij}. This in effect reduces the "dynamic range" of the scene to be reconstructed (using linear combinations of r_{ij}), from M to $\ln M$, makes the reconstrution less "difficult," and reduces the ringing as compared to the principal solution.

Going a step further, we can construct the f_j^{-1} map, which corresponds to the maximum Burg entropy solution (Equation 2.22). This further reduces the "dynamic range,"

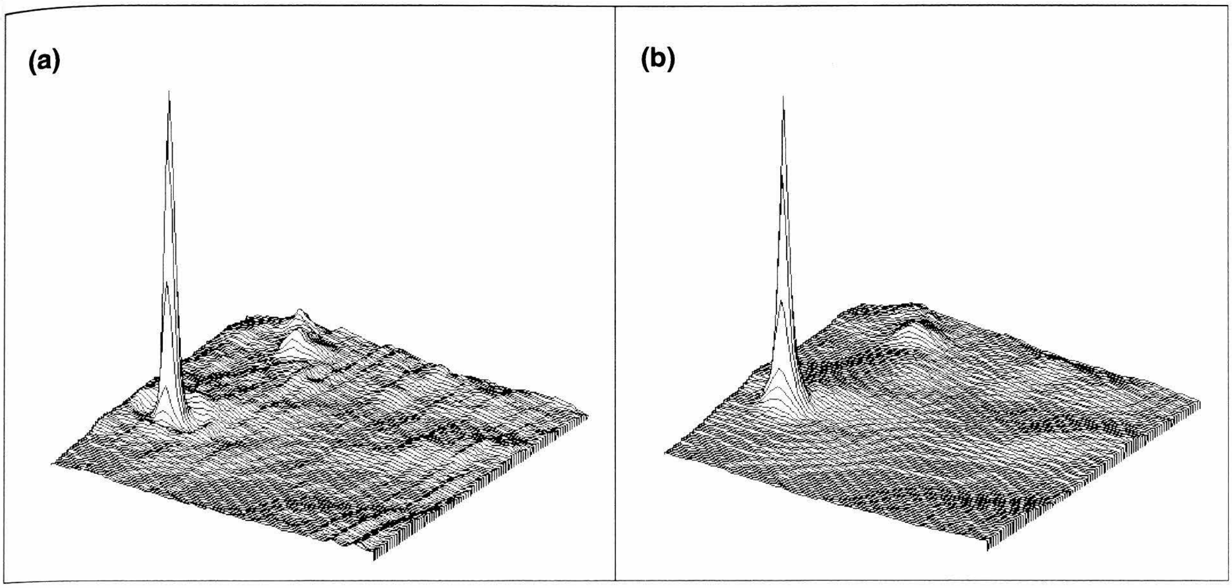

Figure 2.3: Demonstration of the log entropy MART ringing suppression algorithm. (a). Point source I16293-2422 in ρ Ophiuchi, no ringing suppression; (b). Same field, using Burg entropy prior for ringing suppression. Size of image is 1° × 1°. Peak flux in (a) is 3749 MJy sr^{-1}, and 3329 MJy sr^{-1} in (b).

which approaches a constant (but still increases) when M increases. It is also easy to understand that the maximum Burg entropy solution is as far as one can go along this vein for the purpose of ringing suppression, since the "dynamic range" may not decrease with increasing M, for sake of stability.

It is apparent that when f_j^{-1} is updated with small corrections

$$f_j^{-1} \rightarrow f_j^{-1} + \sum_{i=1}^{m} r_{ij} \delta\lambda_i, \tag{2.23}$$

f_j changes according to

$$f_j \rightarrow f_j + f_j^2 \sum_{i=1}^{m} r_{ij}(-\delta\lambda_i). \tag{2.24}$$

We will discuss such an algorithm below.

Algorithm and Results

A variant of the log entropy MART (De Pierro 1991)

$$f_j^{(k+1)} = f_j^{(k)} + (f_j^{(k)})^2 \sum_{i=1}^{m} \frac{r_{ij}}{F_i^2}(D_i - F_i) \tag{2.25}$$

was tested on *IRAS* data.

The $(f_j^{(k)})^2$ factor in the correction term indicates a Burg entropy metric in the image space: the entropy loss (Burg) involved in changing one's knowledge from f_j to $f_j + \Delta f_j$ is

$$\begin{aligned} -\Delta S &= \sum_j \frac{f_j + \Delta f_j}{f_j} - 1 - \log \frac{f_j + \Delta f_j}{f_j} \\ &= \sum_j \frac{1}{f_j^2} (\Delta f_j)^2 \end{aligned} \tag{2.26}$$

for small Δf_j, so if we define the distance as $\sqrt{|\Delta S|}$, the metric tensor becomes

$$g_{jj'} = \begin{cases} 1/f_j^2, & \text{if } j = j' \\ 0, & \text{otherwise} \end{cases} \tag{2.27}$$

The f_j^2 factor then acts to change the covariant gradient vector to contravariant. (See Skilling (1986a) for a similar analysis for the Shannon entropy.)

The Burg entropy metric effectively boosts the correction factor for brighter pixels, so the bright point source is fitted better in the earlier iterations, which circumvents the corruption of background propagated from the misfit near the point source.

The prior knowledge signified by using maximum Burg entropy estimation rule has been discussed in Jaynes (1986) and Frieden (1985). According to Frieden, the class of optical objects described by the Burg entropy prior would tend to consist of a relatively small number of randomly placed bright cells, the rest being dim, befitting the bright point source scene we're concerned with.

Although the above algorithm gave satisfactory result for some test fields (Figure 2.3), it suffers from several problems. First, boosting the correction factors for brighter pixels biases the total flux towards higher value, and when this is combined with the destriping algorithm, which essentially is a self-calibrating scheme, gives rise to bootstrapping and uncontrolled growth of flux in the image. This problem can be solved by performing a standard MCM iteration with no destriping and de-ringing applied, before writing out the image. Richardson-Lucy's good property of local flux conservation thus brings back the image flux to the correct level.

Another more serious problem lies more deeply at the heart of the Burg iterative scheme. Since the correction for fainter pixels is damped near bright ones, the Burg iteration is slower at trimming the lobes of point sources. In addition, convergence of faint source near a bright one is also suppressed, along with the formation of the ring.

These shortcomings of this algorithm prevented further application of it for *IRAS* data, and the *IRAS* Galaxy Atlas was produced using the standard Richardson-Lucy algorithm (plus local offset compensation destriping). However, the notion of reduced ringing with Burg entropy prior is a valid one. According to Eggermont (1996), there are a "zillion" possible algorithms for a given problem, [6] but almost all are "slightly off." Choosing the "right" algorithm therefore depends heavily on mathematical rigor. Although such an algorithm for the Burg entropy image prior did not present itself, we have discovered one which maximizes the cross Burg entropy between measured and modeled data (D_i and F_i), and have obtained satisfactory results.

2.4.2 Cross Log Entropy Maximization [7]

While tackling the ringing problem in *IRAS* image reconstruction, it was found that the image space reconstruction algorithm (ISRA, Daube-Witherspoon & Muehllehner 1986) gives more severe ringing than the Richardson-Lucy algorithm (or EM, which will be used in the rest of this section). In light of the fact that ISRA and EM can be integrated into the same mathematical framework (De Pierro 1993), it is natural to ask whether there is an iterative scheme in the same family, which gives even less ringing than EM.

We present such an algorithm in this section, together with a partial convergence proof and application to *IRAS* data. The algorithm is a multiplicative one that aims to minimize the cross log-entropy between observed and modeled data.

Algorithm

Consider the system of equations $Ax = b$, where A is a non-negative $n \times m$ matrix, $b \in R^n$ is the noisy non-negative data vector, and $x \in R^m$ is considered to be a "model" estimate. If the modeling and the data were exact, the system would have a non-negative solution. In light of the noisy data and the modeling, the sense in which the system $Ax = b$ is to be solved is that of minimum "cross log entropy" (cross Burg entropy, or Itakura–Saito

---

[6] This is apparent from the multitude of ways of manipulating the goodness-of-fit function, see Meinel (1986) for example.

[7] Adapted with changes from "Cross Log Entropy Maximization and Its Application to Ringing Suppression in Image Reconstruction" submitted to *IEEE Transactions on Image Processing* by Y. Cao, P. P. B. Eggermont, & S. Terebey. Used by permission of the authors.

distance), i.e., by solving

$$\begin{array}{ll} \text{minimize} & L(x) \stackrel{\text{def}}{=} \sum_{i=1}^{n} -\log \frac{b_i}{[Ax]_i} + \frac{b_i}{[Ax]_i} \\ \text{subject to} & x \geq 0. \end{array} \tag{2.28}$$

The first thing to note is that if x^* satisfies $Ax^* = b$, then $x = x^*$ solves the problem. The second thing to note is that $L(x)$ is not a convex functional of x, since the logarithmic term is concave. However, it is strictly convex on the set

$$C = \{x \in R^m : [Ax]_i \leq 2b_i, i = 1, 2, \ldots, m\}, \tag{2.29}$$

since $-\log(a/t) + a/t$ is convex on $0 < t \leq 2a$, for $a > 0$, which is non-empty.

We look at two related algorithms

ALGORITHM I.

$$\begin{aligned} x_j &= y_j \sqrt{\frac{[A^T p^k]_j}{[A^T q^k]_j}}, \\ j &= 1, 2, \ldots, m, \end{aligned} \tag{2.30}$$

and

ALGORITHM II.

$$\begin{aligned} x_j &= y_j \cdot \frac{[A^T p^k]_j}{[A^T q^k]_j}, \\ j &= 1, 2, \ldots, m, \end{aligned} \tag{2.31}$$

where

$$\begin{aligned} p_i^k &= \frac{b_i}{([Ay]_i)^2}, \\ q_i^k &= \frac{1}{[Ay]_i}, \\ i &= 1, 2, \ldots, n. \end{aligned} \tag{2.32}$$

If x^1 has positive components, then all the future x^k have all positive components as well. So expressions like x_j^{k+1}/x_j^k are always meaningful. We denote the vector with components x_j^{k+1}/x_j^k simply by x^{k+1}/x^k.

Derivation

As a first step in deriving the algorithms we show

Lemma 1.

$$L(y) - L(x) \geq \sum_{j=1}^{m} \Big\{ [A^T q^k]_j - [A^T p^k]_j \frac{y_j}{x_j} \Big\} (y_j - x_j), \tag{2.33}$$

where

$$\begin{aligned} p_i &= \frac{b_i}{([Ay]_i)^2}, \\ q_i &= \frac{1}{[Ay]_i}, \\ i &= 1, 2, \ldots, n. \end{aligned} \tag{2.34}$$

for any vectors x and y with positive components.

Proof. First of all we note that by the strict concavity of the logarithm

$$-\log \frac{b_i}{[Ay]_i} + \log \frac{b_i}{[Ax]_i} = \log [Ay]_i - \log [Ax]_i \geq \frac{[Ay]_i - [Ax]_i}{[Ay]_i}, \tag{2.35}$$

and so

$$\sum_{i=1}^{n} -\log \frac{b_i}{[Ay]_i} + \log \frac{b_i}{[Ax]_i} \geq \sum_{i=1}^{n} \frac{[A(y-x)]_i}{[Ay]_i} = \sum_{j=1}^{m} [A^T q^k]_j (y_j - x_j). \tag{2.36}$$

Also, there is equality here if and only if $Ax = Ay$. Secondly, we write

$$\frac{b_i}{[Ay]_i} - \frac{b_i}{[Ax]_i} = \frac{b_i}{[Ay]_i} \Big(1 - \frac{[Ay]_i}{[Ax]_i} \Big). \tag{2.37}$$

Now observe that

$$\frac{[Ay]_i}{[Ax]_i} = \Psi\Big(\frac{[Ax]_i}{[Ay]_i} \Big) = \Psi\Big(\frac{[A\{y(x/y)\}]_i}{[Ay]_i} \Big), \tag{2.38}$$

where $\Psi(t) = 1/t$. Now $\Psi(t)$ is strictly convex for $t > 0$, and so by Jensen's inequality

$$\Psi\Big(\frac{[Ay(x/y)]_i}{[Ay]_i} \Big) \leq \frac{[A\{y\Psi(x/y)\}]_i}{[Ay]_i} \tag{2.39}$$

with equality if and only if x_j/y_j is independent of j, for those indices j for which $a_{ij} > 0$. Consequently,

$$\begin{aligned} \sum_{i=1}^{n} \frac{b_i}{[Ay]_i} - \frac{b_i}{[Ax]_i} &\geq \sum_{i=1}^{n} \frac{b_i}{[Ay]_i} \Big(1 - \frac{A\{(y)^2/x\}}{[Ay]_i} \Big) \\ &= \sum_{i=1}^{n} \frac{b_i}{([Ay]_i)^2} [A(y - (y)^2/x)]_i \\ &= \sum_{j=1}^{m} [A^T p^k]_j \frac{y_j}{x_j} (x_j - y_j) \end{aligned} \tag{2.40}$$

with equality if and only if x/y is the constant vector. Adding (2.36) and (2.40) gives

$$L(y) - L(x) \geq \sum_{j=1}^{m} \left\{ [A^T q^k]_j - [A^T p^k]_j \frac{y_j}{x_j} \right\} (y_j - x_j) = 0. \tag{2.41}$$

Q.E.D.

Lemma 1 can be rewritten as

$$L(x) \leq L(y) + \sum_{j=1}^{m} [A^T p^k]_j \left\{ \frac{(y_j)^2}{x_j} - y_j \right\} - [A^T q^k]_j (y_j - x_j). \tag{2.42}$$

Since we want to minimize the left side of (2.42), but are unable to do this directly, let us minimize the right-hand side of (2.42). Assuming that we can do this by differentiating the right-hand side of (2.42) with respect to x_j, and setting this equal to 0 gives

$$\begin{gathered} -[A^T p^k]_j \frac{(y_j)^2}{(x_j)^2} + [A^T q^k]_j = 0, \\ j = 1, 2, \ldots, m, \end{gathered} \tag{2.43}$$

and so (2.42) suggests a way of achieving a new estimate of vector x from y

$$\begin{aligned} x_j &= y_j \sqrt{\frac{[A^T p^k]_j}{[A^T q^k]_j}}, \\ j &= 1, 2, \ldots, m. \end{aligned} \tag{2.44}$$

For this reason we call inequalities like (2.42) "tendentious inequalities" because they suggest algorithms, and much more. De Pierro (1995) calls this approach "majorizing functions algorithm."

An "accelerated" version of (2.44) can be derived if we choose x_j such that the second term in (2.42) equals zero

$$\begin{gathered} -[A^T p^k]_j \frac{y_j}{x_j} + [A^T q^k]_j = 0, \\ j = 1, 2, \ldots, m, \end{gathered} \tag{2.45}$$

which leads to

$$\begin{aligned} x_j &= y_j \cdot \frac{[A^T p^k]_j}{[A^T q^k]_j}, \\ j &= 1, 2, \ldots, m. \end{aligned} \tag{2.46}$$

Applying (2.44) or (2.46) iteratively gives rise to ALGORITHM I or ALGORITHM II.

Monotonicity Property

For ALGORITHM I, we have the following monotonicity property from (2.42)

$$\begin{aligned} L(x^{k+1}) - L(x^k) &\leq \sum_{j=1}^{m} 2x_j^k \sqrt{[A^T q^k]_j [A^T p^k]_j} - x_j^k [A^T p^k]_j - x_j^k [A^T q^k]_j = \\ &\leq -\sum_{j=1}^{m} x_j^k \left| \sqrt{[A^T p^k]_j} - \sqrt{[A^T q^k]_j} \right|^2 = \\ &\leq -\sum_{j=1}^{m} [A^T q^k]_j \frac{\left| x_j^{k+1} - x_j^k \right|^2}{x_j^k}, \end{aligned} \tag{2.47}$$

or

$$L(x^k) - L(x^{k+1}) \geq \sum_{j=1}^{m} [A^T q^k]_j \frac{\left| x_j^{k+1} - x_j^k \right|^2}{x_j^k}. \tag{2.48}$$

It shows that $L(x^k) > L(x^{k+1})$, unless $x^k = x^{k+1}$, and that if x^* solves (2.28), then it is a fixed point of ALGORITHM I.

For ALGORITHM II, it is obvious from the derivation that

$$L(x^k) \geq L(x^{k+1}), \tag{2.49}$$

i.e., the negative log entropy $L(x)$ never increases.

Convergence Speed

From test runs using *IRAS* data, it was found that ALGORITHM I and ALGORITHM II give quantitatively similar images, with ALGORITHM II converging roughly twice as fast as ALGORITHM I (see Table 2.1). This can be explained by the fact that corrections are small except in the first few iterations.

Besides ALGORITHM II's faster convergence speed, it also gives better photometric integrity in the first few iterations compared to ALGORITHM I. The first iteration result from ALGORITHM II is just the usual co-added image, identical to that from EM's first iteration, assuming the zeroth image is flat in both cases. ALGORITHM I, however, because of the square root corrections employed, gives images that have absolute scales dependent on the magnitude of the zeroth image (although the effect is washed out quadratically in the later iterations).

These considerations led us to prefer ALGORITHM II in the *IRAS* application, and we restrict our discussion to ALGORITHM II in the following (the result from ALGORITHM I being similar at twice the number of iterations anyway).

Table 2.1. Convergence Speed Comparison

ALGORITHM I		ALGORITHM II	
Iter.	$L - n$	Iter.	$L - n$
10	201.54	5	205.97
20	191.15	10	192.13
30	187.42	15	187.93
40	185.12	20	185.48
50	183.39	25	183.68

Ringing Suppression

The algorithm was tested on several fields of the *IRAS* data. For all cases, the resultant images showed weaker ringing around point sources than images made with the EM algorithm.

Figure 2.4 shows a comparison of reconstructed images using EM, ISRA, and the log entropy algorithm (ALGORITHM II), all at 20 iterations, plus a co-added image. The co-added image in Figure 2.4(a) is a simple average of detector fluxes weighted by the response function, equivalent to the first iteration image from EM, ISRA, and ALGORITHM II. The reconstructed images ((b), (c), and (d)) show enhanced resolution compared to the co-added image. The field captures one of the most luminous stars in the sky, α Ori, [8] at 60 μm. The arc to the top-left of the star is a bow shock caused by the motion of the star in the interstellar medium. In the EM and ISRA images ((b) and (c)), the severe ringing artifact disturbs the shape of the bow shock (the spurious ring is slightly brighter than the bow shock). It is also apparent that ISRA resulted in more severe ringing than EM. The image from the new log entropy algorithm ((d)) shows great improvement, effectively suppresses the ringing, reconstructs the bow shock cleanly, and even recovers a hint of the diffraction spikes around the bright star. The log entropy image also gives a sharper profile of the star than the EM image at the same number of iterations, with a peak intensity (star) 1.4 times that of the EM image. The maximum pixel intensity of the bow shock ($\sim$ 25 MJy sr^{-1}) is

---

[8] α Orionis, also called Betelgeuse, a cool red supergiant approximately 180 pc from the Earth.

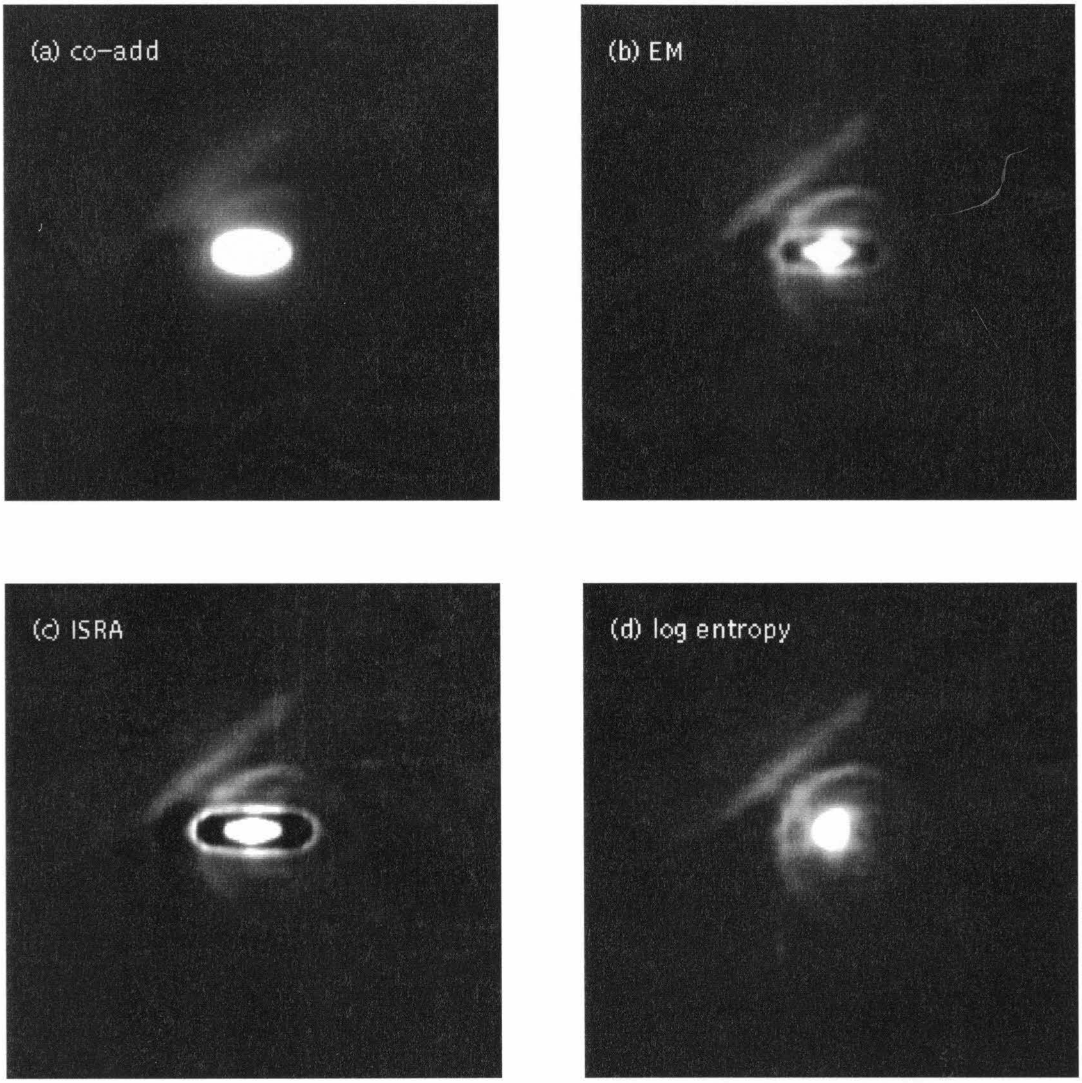

Figure 2.4: Comparison of reconstructed images using EM, ISRA, and the log entropy algorithm (α Ori, 60 μm). (a): co-add (or weighted average) of detector fluxes; (b), (c): EM and ISRA, severe ringing around the bright star is present, and the arc (bow shock) to the top-left of the star is disrupted; (d): the log entropy image suppresses the ringing and reconstructs the bow shock cleanly. Angular scale is 1° on each side. The brightest pixel in the bow shock has intensity $\sim 1/150$ of the peak intensity of the star. The spurious ring in the EM image is slightly brighter than the bow shock.

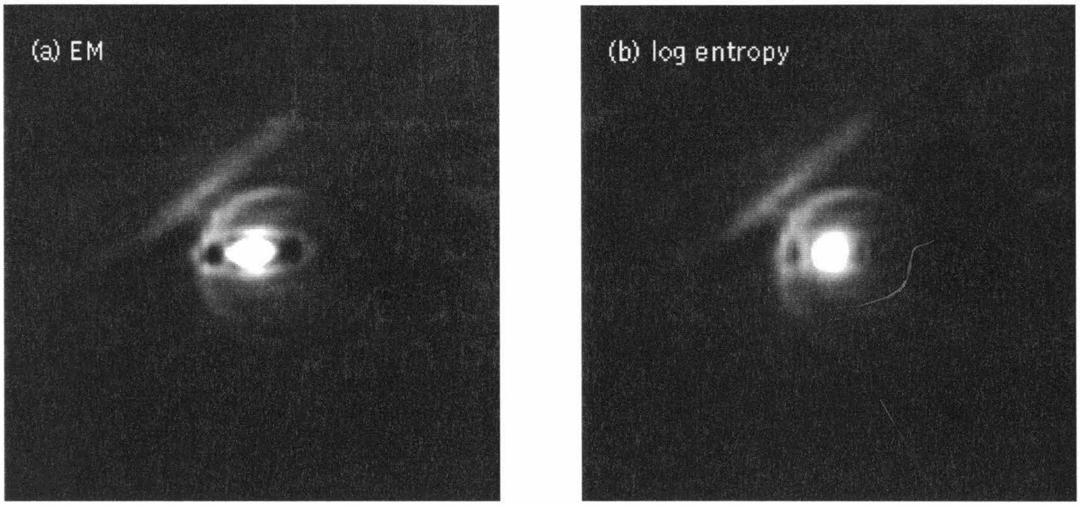

Figure 2.5: Comparison of reconstructed images from simulated data. (a): EM reconstruction; (b): log entropy reconstruction. The results verify the consistency of the log entropy algorithm.

about 1/150 of that of the star (3596 MJy sr^{-1} in the log entropy image).

Validation Using Simulated Data

To validate the authenticity of the bow shock structure and the result of reduced ringing, simulated data were constructed using the actual *IRAS* scan pattern and detector response functions, and taking the log entropy image in Figure 2.4(d) as the sky brightness. The simulated data were then processed with the EM and the log entropy algorithm respectively.

The resultant images are shown in Figure 2.5. Again, the EM image showed ringing similar to the corresponding image in Figure 2.4. The log entropy image is similar to the input from which the simulated data were made (Figure 2.4(d)), indicating the log entropy algorithm is more consistent with our preference [9] for this test case.

Also, the fact that the output images made from simulated data are similar to the ones made from real data indicates the two sets of data contain comparable amount of high spatial frequency signal, i.e., the input image that went into the simulated data can

---

[9] It should be noted that the data alone do not favor one output image or the other. Reduced ringing is preferred due to our prior knowledge that point sources do not usually come with rings.

be considered as well resolved.

Discussion

Using the notations of Section 2.1, ALGORITHM II takes the form of

$$\begin{aligned} f_j^{k+1} &= f_j^k \cdot \frac{\sum_{i=1}^m r_{ij} D_i / F_i^2}{\sum_{i=1}^m r_{ij}/F_i}, \\ j &= 1, \ldots, n. \end{aligned} \tag{2.50}$$

The ringing artifact can be seen as being caused by the propagation of data misfit at the point source. The new algorithm attenuates the propagation by the $1/F_i$ weighting factor, compared to EM, which results in better determination of the background.

In the reconstructed image, the point source has a finite width profile due to the finite resolution achieved, while in the true scene the point source mimics a delta function. This causes the modeled data F_i to have a longer "tail" than the measured data D_i. While trying to compensate for the misfit ($F_i \gg D_i$), the correction factors push down the pixels around the point source, giving the first dip in the ripples. The dip then causes misfit further away from the point source, which in turn results in the bright ring, so on and so forth.

The reduction in ringing by the log entropy algorithm can be traced to the concavity of L at large F_i. Similar to *M*-estimators in robust estimation (cf. Press et al. 1992, pp. 699–702), the derivative of L decreases in absolute value as F_i increases (at fixed D_i), i.e., the cost function curve flattens out at large values of F_i (Table 2.3). Therefore, the data points that have F_i mixing the blurred point source and the background ($F_i \gg D_i$) are seen as "outliers," and the corrections incurred on the image pixels by these data points are weighted down.

Figure 2.6 shows a plot of the negative log entropy and the negative log Poisson likelihood as a function of F_i. The negative log Poisson likelihood is convex, while the negative log entropy is concave for large values of F_i.

Maximizing the log entropy functional corresponds to maximum likelihood estimation from Gamma distributions. The Gamma likelihood has a "fatter tail" than the Poisson or Gaussian, [10] making the log entropy algorithm more tolerant of bright point

---

[10] It is well known that the Poisson and Gamma distributions approach the Gaussian when the mean values are large (central limit theorem). This does not contradict the fact that the Gamma distribution has a fatter tail than the Poisson or Gaussian (even when the mean is large), as different parts of the distribution converge to the Gaussian form at different rates (Press et al. 1992, p. 659).

Table 2.2. Comparison of ISRA, EM, and the Log Entropy Algorithm

Algorithm	Cost Function L	Update Rule
ISRA *	$\sum_i (D_i - F_i)^2$	$f_j^{k+1} = f_j^k \frac{\sum_i r_{ij} D_i}{\sum_i r_{ij} F_i}$
EM	$\sum_i -(D_i - F_i) + D_i \log D_i/F_i$	$f_j^{k+1} = f_j^k \frac{\sum_i r_{ij} D_i/F_i}{\sum_i r_{ij}}$
Log Entropy	$\sum_i - \log D_i/F_i + D_i/F_i$	$f_j^{k+1} = f_j^k \frac{\sum_i r_{ij} D_i/F_i^2}{\sum_i r_{ij}/F_i}$

*The update rule here corresponds to least squares estimates when all the data samples have the same variance. When the different data samples i have different noise deviation σ_i, a simple rescaling of the variables leads to the following update rule: $f_j^{k+1} = f_j^k \left[\sum_i \frac{r_{ij}}{\sigma_i^2} D_i\right] / \left[\sum_i \frac{r_{ij}}{\sigma_i^2} F_i\right]$. This is recommended as the proper way to weight data samples with different noise magnitude, instead of the MCM form shown in Section 2.1.

Table 2.3. Comparison of Cost Functions and Derivatives

Cost Function L	$\partial L/\partial F_i$	$\partial^2 L/\partial F_i^2$
$\sum_i (D_i - F_i)^2$	$2(F_i - D_i)$	$2 > 0$
$\sum_i -(D_i - F_i) + D_i \log D_i/F_i$	$1 - D_i/F_i$	$D_i/F_i^2 > 0$
$\sum_i - \log D_i/F_i + D_i/F_i$	$1/F_i - D_i/F_i^2$	$-1/F_i^2 + 2D_i/F_i^3 < 0$ (F_i large)

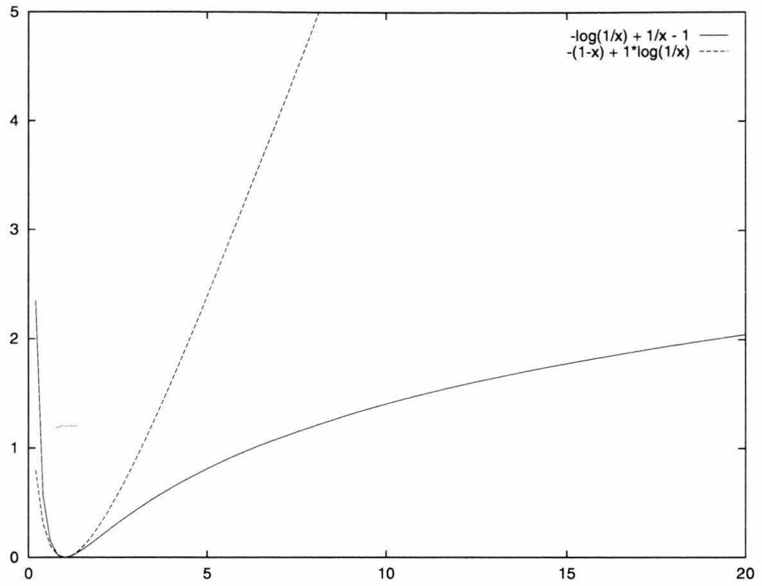

Figure 2.6: Comparison of the negative log entropy and the negative log Poisson likelihood. Solid curve: negative log entropy; Dashed curve: negative log Poisson likelihood. Horizontal axis: F_i. $D_i = 1$.

source scenes than the EM and ISRA, which are suitable for maximum Poisson likelihood and least squares estimates (De Pierro 1987; Eggermont 1990). The choice of Gamma likelihood (which is invariant under scaling of D_i and F_i), has some justification for astronomical scenes, where it is reasonable to assume that no preferred absolute magnitude scale exists (which is not true for the Gaussian or Poisson distributions). It appears natural to use the Gamma likelihood when the misfit between model and data is dominated by the mixing of signal on different magnitude scales in the model (like the bright point source case), instead of photon counting statistics (Poisson) or read-out noise (Gaussian).

Quantifying the ringing magnitude (and the reduction from EM to the log entropy algorithm) is not a trivial task, as the ringing depends on such parameters as the background intensity, the point source strength, and the position of the data samples. First we look at the asymptotic behavior of minimum modeled data (F_i) when the point source strength is large, assuming the point source sits on a flat background of fixed intensity.

Assume an image pixel j is covered by only two data samples, 1 and 2. Both are centered far enough from the point source, so that

$$D_1 = D_2 = f_B \sum_j r_{1j} \overset{\text{def}}{=} B, \tag{2.51}$$

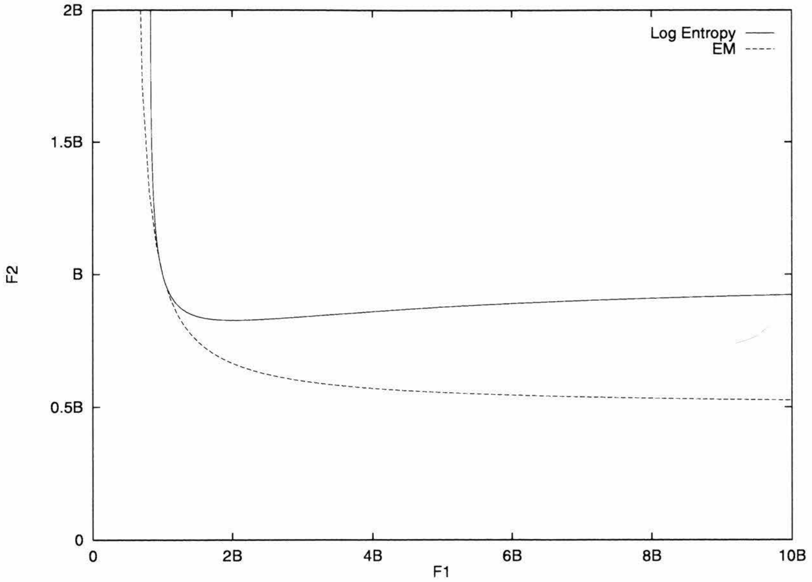

Figure 2.7: Comparison of the inter-dependence of modeled data. Solid curve: log entropy case, F_2 approaches B when F_1 is large; Dashed curve: EM, F_2 approaches $B/2$.

where f_B is the background intensity. Also, we assume sample 1 covers part of the side lob of the (finite sized) point source in the reconstructed image, and sample 2 lies further apart from the point source and does not overlap with the reconstructed point source.

We then look at the dependence of F_1 and F_2 on each other when the iteration has proceeded near convergence. Convergence is achieved when the correction terms from the two samples on the image pixel j cancel each other.

Under the EM scheme, we would then have

$$r_{1j}D_1/F_1 + r_{2j}D_2/F_2 = r_{1j} + r_{2j}. \tag{2.52}$$

While if the log entropy algorithm was used, we would have

$$r_{1j}D_1/F_1^2 + r_{2j}D_2/F_2^2 = r_{1j}/F_1 + r_{2j}/F_2. \tag{2.53}$$

A schematic comparison of (2.52) and (2.53) is shown in Figure 2.7 (r_{1j} and r_{2j} were assumed to be equal in the plots).

When the point source is very bright, $F_1 \gg B$ (because sample 1 covers part of the reconstructed point source), and as can be seen from Figure 2.7, F_2 approaches the correct background flux B with the log entropy algorithm, but only a fraction of B with EM

Table 2.4. Comparison of Minimum Modeled Data

Point Source Magnitude (Jy)	Minimum F_i with EM	Minimum F_i with log entropy
10	4.72	4.73
10^2	4.51	4.59
10^3	4.01	4.37
10^4	2.96	4.38
10^5	2.41	4.54

(reflecting the dip around the point source). F_2 is taken to be an estimate of the minimum F_i.

The different characteristic behavior of minimum F_i was replicated in simulations, using images reconstructed from synthetic data. A point source with varying strength was planted onto a constant background (30 MJy sr^{-1}), and the actual *IRAS* scan pattern was run through the artificial image, and a set of synthetic data was generated. After that EM and the log entropy algorithm were used to process the data separately. Table 2.4 shows the comparison of minimum modeled data F_i after 100 iterations. For EM, the minimum F_i keeps decreasing with increasing point source strength. And for the log entropy algorithm, the minimum F_i first decreases, then climbs back towards B as the point source strength increases, showing good agreement with the curve shown in Figure 2.7.

In these simulations it was found the rings from the log entropy algorithm have smaller sizes than those from EM (which are in turn smaller than those from ISRA). Also, the peak intensity of the reconstructed star is the highest with the log entropy algorithm. These observations are consistent with the fact that the log entropy algorithm requires more high spatial frequency power in the image than EM and ISRA.

Unlike some other ringing suppression schemes, the log entropy algorithm does not require extra prior information (such as point source position and/or strength) as input, and does not require the fine tuning of parameters. It is also structurally similar to EM and ISRA, making it very easy to incorporate in existing image reconstruction software. These

Table 2.5. Comparison of Maximum Pixel Intensity

Point Source Magnitude (Jy)	Maximum f_j (MJy sr^{-1}) with EM	with Log Entropy	Ratio
10	4.63×10	4.91×10	1.06
10^2	7.16×10^2	1.08×10^3	1.51
10^3	1.26×10^4	3.01×10^4	2.39
10^4	1.63×10^5	7.39×10^5	4.54
10^5	1.73×10^6	8.12×10^6	4.70

advantages make it likely to be applied to a wide range of problems where ringing artifact is a concern.

References

Aumann, H. H., Fowler, J. W., and Melnyk, M. 1990. A maximum correlation method for image construction of *IRAS* survey data. *Astron. J.*, **99**, 1674.

Bontekoe, T. R., Koper, E., & Kester, D. J. M. 1994. Pyramid maximum-entropy images of *IRAS* survey data. *Astron. & Astrophys.*, **284**, 1037.

Burch, S. F., Gull, S. F., & Skilling, J. 1983. Image restoration by a powerful maximum-entropy method. *Computer Vision, Graphics, and Image Processing*, **23**, 113.

Cao, Y. & Prince, T. A. 1994. Constraints as a destriping tool for HIRES images. In *Science with High Spatial Resolution Far-Infrared Data,* ed. S. Terebey & J. Mazzarella (Pasadena: JPL 94-5), 55.

Cao, Y., Prince, T. A., Terebey, S., & Beichman, C. A. 1996. Parallelization and algorithmic enhancements of high resolution *IRAS* image construction. *Pub. Astron. Soc. Pacific*, **108**, 535.

Cao, Y., Eggermont, P. P. B., & Terebey, S. 1996. Cross log entropy maximization and its application to ringing suppression in image reconstruction. *IEEE Trans. Image Proc.*, submitted.

Daube-Witherspoon, M. E. & Muehllehner, G. 1986. An iterative image space reconstruction algorithm suitable for volume ECT. *IEEE Trans. Med. Imaging*, **5**, 61.

Dempster, A. D., Laird, N. M., & Rubin, D. B. 1977. Maximum likelihood from incomplete data via the EM algorithm. *J. Royal Stat. Soc. B*, **39**, 1.

De Pierro, A. R. 1987. On the convergence of the iterative image space reconstruction algorithm for volume ECT. *IEEE Trans. Med. Imaging*, **6**, 174.

De Pierro, A. R. 1991. Multiplicative iterative methods in computed-tomography. *Lecture Notes in Mathematics*, **1497**, 167.

De Pierro, A. R. 1993. On the relation between the ISRA and the EM algorithm for positron emission tomography. *IEEE Trans. Med. Imaging,* **12**, 328.

De Pierro, A. R. 1995. A modified expectation maximization algorithm for penalized likelihood estimation in emission tomography. *IEEE Trans. Med. Imaging,* **14**, 132.

Eggermont, P. P. B. 1990. Multiplicative iterative algorithms for convex-programming. *Linear Algebra Appl.*, **130**, 25.

Eggermont, P. P. B. 1996. Private communication.

Faisal, M., Lanterman, A. D., Snyder, D. L., & White, R. L. 1995. Implementation of a modified Richardson-Lucy method for image-restoration on a massively-parallel computer to compensate for space-variant point-spread of a charge-coupled-device camera. *J. Opt. Soc. Amer.* A, **12**, 2593.

Fowler, J. W. & Aumann, H. H. 1994. HIRES and beyond. In *Science with High Spatial Resolution Far-Infrared Data,* ed. S. Terebey & J. Mazzarella (Pasadena: JPL 94-5), 1.

Fowler, J. W., & Melnyk, M. 1990. *LAUNDR Software Design Specifications* (Pasadena: JPL).

Frieden, B. R. 1985. Estimating occurrence laws with maximum probability, and the transition to entropic estimators. In *Maximum-Entropy and Bayesian Methods in Inverse Problems*, ed. C. R. Smith & W. T. Grandy, Jr. (Dordrecht: Reidel), 133.

Geman, G. & McClure D. 1987. Statistical methods for tomographic image reconstruction. *Bull. Int. Stat. Inst.*, **LII-4**, 5.

Gull, S. F. 1989. Developments in maximum entropy data analysis. In *Maximum Entropy and Bayesian Methods*, ed. J. Skilling (Dordrecht: Kluwer), 53.

Hanisch, R. J. & White, R. L. 1994a. *HST* image-restoration – current capabilities and future prospects. *IAU Symposia*, **158**, 61.

Hanisch, R. J. & White, R. L. 1994b. *The Restoration of HST Images and Spectra – II* (Baltimore: STScI).

Hurt, R. L. & Barsony, M. 1996. A cluster of class-0 protostars in Serpens – an *IRAS* HIRES study. *Astrophys. J.*, **460**, L45.

IRAS Catalogs and Atlases: Explanatory Supplement 1988. Beichman, C. A., Neugebauer, G., Habing, H. J., Clegg, P. E., & Chester, T. J. (eds.) (Washington, DC: GPO).

Jaynes, E. T. 1986. Monkeys, kangaroos, and N. In *Maximum Entropy and Bayesian Methods in Applied Statistics*, ed. J. H. Justice (Cambridge: Cambridge U. Press), 26.

Lange, K. & Carson, R. 1984. EM reconstruction algorithms for emission and transmission tomography. *J. Comput. Assisted Tomography,* **8**, 306.

Levitan, E. & Herman G. 1987. A maximum *a posteriori* probability expectation maximization algorithm for image reconstruction in emission tomography. *IEEE Trans. Med. Imaging,* **6**, 185.

Llacer, J. & Veklerov, E. 1989. Feasible images and practical stopping rules for iterative algorithms in emission tomography. *IEEE Trans. Med. Imaging,* **8**, 186.

Lucy, L. B. 1974. An iterative technique for the rectification of observed distributions. *Astron. J.*, **79**, 745.

Lucy, L. B. 1994. Image restorations of high photometric quality. In *The Restoration of HST Images and Spectra – II*, ed. R. J. Hanisch & R. White (Baltimore: STScI), 79.

Meier, D. L. 1990. Optical interferometers in space: what the program can do for *HST*; what *HST* can do for the program. In *The Restoration of HST Images and Spectra*, ed. R. L. White & R. J. Allen (Baltimore: STScI), 113.

Meinel, E. S. 1986. Origins of linear and nonlinear recursive restoration algorithms. *J. Opt. Soc. Amer.* A, **3**, 787.

Molina, R., Del Olmo, A., Perea, J., & Ripley, B. D. 1992. Bayesian deconvolution in optical astronomy. *Astron. J.*, **103**, 666.

Narayan, R. 1986. Maximum entropy image restoration in astronomy. *Ann. Rev. Astron. Astrophys.*, **24**, 127.

Núñez, J. & Llacer, J. 1990. Bayesian image-reconstruction in astronomy. *Astrophys. & Space Sci.*, **171**, 341.

Núñez, J. & Llacer, J. 1993. A general Bayesian image-reconstruction algorithm with entropy prior – preliminary application to *HST* data. *Pub. Astron. Soc. Pacific*, **105**, 1192.

Perry, K. M. & Reeves, S. J. 1994. Generalized cross-validation as a stopping rule for the Richardson-Lucy algorithm. In *The Restoration of HST Images and Spectra – II*, ed. R. J. Hanisch & R. White (Baltimore: STScI), 97.

Press, W. H., Teukolsky, S. A., Vetterling, W. T., & Flannery, B. P. 1992. *Numerical Recipes in C: The Art of Scientific Computing*, 2nd ed. (Cambridge: Cambridge U. Press).

Richardson, W. H. 1972. Bayesian-based iterative method of image restoration. *J. Opt. Soc. Amer.*, **62**, 55.

Shepp, L. A. & Vardi, Y. 1982. Maximum likelihood reconstruction in positron emission tomography. *IEEE Trans. Med. Imaging*, **1**, 113.

Skilling, J. & Bryan, R. K. 1984. Maximum-entropy image reconstruction – general algorithm. *Mon. Not. R. Astron. Soc.*, **211**, 111.

Skilling, J. & Gull, S. F. 1985. Algorithms and applications. In *Maximum Entropy and Bayesian Methods in Inverse Problems*, ed. C. R. Smith & W. T. Grandy (Dordrecht: Reidel), 83.

Skilling, J. 1986. The Cambridge maximum entropy algorithm. In *Maximum Entropy and Bayesian Methods in Applied Statistics*, ed. J. H. Justice (Cambridge: Cambridge U. Press), 26.

Skilling, J. 1986. Theory of maximum entropy reconstruction. In *Maximum Entropy and Bayesian Methods in Applied Statistics*, ed. J. H. Justice (Cambridge: Cambridge U. Press), 156.

Snyder, D. L. & Miller, M. I. 1985. The use of sieves to stabilize images produced with the EM algorithm for emission tomography. *IEEE Trans. Nucl. Sci.*, **32**, 3864.

Snyder, D. L., Miller, M. I., Thomas, L. J. Jr., & Politte, D. G. 1987. Noise and edge artifacts in maximum-likelihood reconstructions for emission tomography. *IEEE Trans. Med. Imaging*, **6**, 228.

Snyder, D. L. 1990. Modifications of the Lucy-Richardson iteration for restoring *Hubble Space-Telescope* imagery. In *The Restoration of HST Images and Spectra*, ed. R. L. White & R. J. Allen (Baltimore: STScI), 56.

Snyder, D. L., Helstrom, C. W., Lanterman, A. D., Faisal, M., & White, R. L. 1995. Compensation for readout noise in CCD images. *J. Opt. Soc. Amer.* A, **12**, 272.

Starck, J.-L. & Murtagh, F. 1994. Image-restoration with noise suppression using the wavelet transform. *Astron. & Astrophys.*, **288**, 342.

Ter-Pogossian, M. M., Raichle, M. E., & Sobel, B. E. 1980. Positron emission tomography. *Sci. Amer.*, **243**, 170.

Vardi, Y., Shepp, L. A., & Kaufman, L. 1985. A statistical model for positron emission tomography. *J. Amer. Stat. Assoc.*, **80**, 8.

Veklerov, E. & Llacer, J. 1987. Stopping rule for the MLE algorithm based on statistical hypothesis-testing. *IEEE Trans. Med. Imaging*, **6**, 313.

Veklerov, E. & Llacer, J. 1990. The feasibility of images reconstructed with the method of sieves. *IEEE Trans. Nucl. Sci.*, **37**, 835.

Weir, N. & Djorgovski, S. 1990. MEM: new techniques, applications, and photometry. In *The Restoration of HST Images and Spectra*, ed. R. L. White & R. J. Allen (Baltimore: STScI), 31.

White, R. L. 1994. Image restoration using the damped Richardson-Lucy method. In *The Restoration of HST Images and Spectra – II*, ed. R. J. Hanisch & R. White (Baltimore: STScI), 104.

White, R. L. & Allen, R. J. (eds.) 1990. *The Restoration of HST Images and Spectra* (Baltimore: STScI).

Wu, C. F. J. 1983. On the convergence properties of the EM algorithm. *Annals of Statistics*, **11**, 95.

Chapter 3

The *IRAS* Galaxy Atlas *

3.1 Overview

In 1983 *IRAS* fundamentally changed our view of the infrared sky when it conducted the first infrared all sky survey. The *IRAS* data have proven important to the study of many astrophysical phenomena, including star formation, the interstellar medium, Galactic structure, late-type stars, supernova remnants, external galaxies, infrared cirrus and debris disks around nearby stars (Beichman 1987; Soifer, Houck, & Neugebauer 1987; *IRAS* Catalogs and Atlases: Explanatory Supplement 1988). New spacecraft missions such as *ISO* (*Infrared Space Observatory*, Kessler 1995), *MSX* (*Midcourse Space Experiment*, Price 1995; Mill & Guilmain 1996), and *IRTS* (*Infrared Telescope in Space*, Matsumoto 1995) now provide higher sensitivity and spatial resolution. However, by design they observe only a small fraction of the sky, thus ensuring that *IRAS* will provide a fundamental archive for many years to come.

The native spatial resolution of the *IRAS* co-added data is several by five arcminutes. Various image reconstruction techniques have been applied to the *IRAS* data in the quest to extract higher spatial resolution (Terebey & Mazzarella 1994). These include maximum entropy techniques, among them the HIRAS package developed at Gröningen (Assendorp et al. 1995; Bontekoe et al. 1994). Making use of an alternate approach, the production of the *IRAS* Galaxy Atlas is based on the well-known HIRES processor, first developed in 1991 and made available to the scientific community by the Infrared Process-

---

*Adapted from "The High Resolution *IRAS* Galaxy Atlas" submitted to *The Astrophysical Journal Supplement Series*, by Y. Cao, S. Terebey, T. A. Prince, & C. A. Beichman. Used by permission of the authors.

ing and Analysis Center (IPAC). HIRES implements the iterative maximum correlation method (MCM; Aumann, Fowler, & Melnyk 1990), a variant of the Richardson-Lucy algorithm which has been optimized for *IRAS* data. The advantages of HIRES include flux conservation, speed of processing, and the ability to work reliably on faint sources. HIRES images have been successfully used for a variety of Galactic and extra-Galactic studies (Rice 1993; Surace et al. 1993; Terebey & Mazzarella 1994).

The parallel supercomputing facilities available at Caltech and the development of new artifact reduction algorithms made possible a large-scale high-resolution *IRAS* mapping of the Galactic plane (Cao et al. 1996a). The new *IRAS* Galaxy Atlas (IGA) maps, which have $1' - 2'$ resolution, provide a ten-fold improvement in areal resolution over the *IRAS* Sky Survey Atlas (ISSA; *IRAS* Sky Survey Atlas Explanatory Supplement 1994), and covers more than 3300 square degrees of the Galactic plane ($-4.7° < b < 4.7°$), plus more than 1100 square degrees of the Orion, ρ Ophiuchi, and Taurus-Auriga molecular clouds (see Chapter 1). Aside from the parallelization of the HIRES program, the IGA incorporates several important differences from HIRES processing at IPAC. Foremost is improved destriping and zodiacal emission subtraction, which lead to reduced artifacts, enhanced structure, and the ability to mosaic images without edge discontinuities. The IGA is well-suited to high-resolution studies of extended structure and will be valuable for a wide range of scientific studies, including: the structure and dynamics of the interstellar medium (ISM); cloud core surveys within giant molecular clouds; detailed studies of H II regions and star forming regions; determination of initial mass functions (IMFs) of massive stars; and study of supernova remnants (SNRs). The IGA will be especially useful for multi-wavelength studies using the many Galactic plane surveys that have similar ($\sim 1'$) resolution. These include the new FCRAO CO J=1–0 spectral line (Heyer et al. 1994) and DRAO H I line/21 cm continuum surveys (Normandeau, Taylor, & Dewdney 1997).

Most image reconstruction algorithms have their quirks. This chapter describes and characterizes the IGA so that it will be useful for quantitative scientific study. Section 3.2 describes the geometry and information content of the atlas images. Section 3.3 gives a description on the various processing stages, namely the basic algorithm, subtraction of zodiacal emission, and coordinate transform and reprojection. Section 3.5 discusses the characteristics of the images, including resolution, photometric and positional accuracy, mosaic properties, and calibration. Discussion of image artifacts is given in Section 3.6.

The IGA images are available upon request from IPAC (`info@ipac.caltech.edu`) or through the NSSDC. The IGA home page is available at `http://www.cacr.caltech.edu/~yucao/iga.html`.

3.2 Description of the Atlas

The atlas consists of images (1st and 20th iteration of HIRES) and ancillary maps in FITS (Wells, Greisen, & Harten 1981) format covering $0^\circ \leq l < 360^\circ, -4.7^\circ < b < 4.7^\circ$ in the 60 and 100 μm wavelength bands. The 1st iteration images are co-added *IRAS* images with no resolution enhancement. For the fields covering the Galactic plane, the field of view for each image is $1.4^\circ \times 1.4^\circ$, on 1° centers in both the Galactic longitude and latitude directions, the pixel size is $15''$, and Galactic coordinates and Cartesian projection are used. For the molecular cloud fields (Orion, ρ Ophiuchi, Taurus-Auriga), the images are $2.5^\circ \times 2.5^\circ$ on 2° centers, using Equatorial coordinates (B1950) and Cartesian projection. The regions covered by the Atlas in these fields are as follows: $05^{\rm h}08^{\rm m} < \alpha < 06^{\rm h}12^{\rm m}$, $-13^\circ < \delta < +18^\circ$ (Orion); $15^{\rm h}31^{\rm m} < \alpha < 17^{\rm h}00^{\rm m}$, $-33^\circ < \delta < -17^\circ$ (ρ Ophiuchi); and $03^{\rm h}48^{\rm m} < \alpha < 05^{\rm h}12^{\rm m}$, $+12^\circ < \delta < +33^\circ$ (Taurus-Auriga).

The 1st iteration images correspond to co-added *IRAS* images at the native *IRAS* resolution of approximately $2.0' \times 4.7'$ at 60 μm and $3.8' \times 5.4'$ at 100 μm. After MCM processing to 20 iterations the typical spatial resolution improves to $1.0' \times 1.7'$ at 60 μm and $1.7' \times 2.2'$ at 100 μm (see Section 3.5.1). Note that the images at 60 and 100 μm have inherently different resolutions. Ratio maps should be attempted only after correcting the images to a common resolution (see Chapter 4).

The images are on the same absolute flux level as ISSA except for a constant factor (see Section 3.5.3).

The ancillary maps include the correction factor variance (CFV) map, the photometric noise (PHN) map, coverage (CVG) map, the detector track (DET) map, and the beam sample map (BEM) (see Section 3.7 for example images). The FWHM*.txt text file gives beam sizes derived from the corresponding BEM map.

Table 3.1 shows the quantities represented by the ancillary maps (Aumann, Fowler, & Melnyk 1990). The correction factor variance (CFV) map gives an estimate of level of convergence at a certain pixel, measuring the agreement of correction factors projected onto it from different detector footprints. The photometric noise (PHN) map signifies the photometric noise at a pixel, propagated from noise in the detector measurements. The

Table 3.1. Image and Ancillary Maps

Abbr. Name	Name of Map	Quantity
IMG	image	f_j
PHN	photometric noise	$(\sum_i r_{ij}/\sigma_{ij}^2)^{-1/2}$, where $\sigma_{ij} = \sigma_i[f_j/\sum_j(r_{ij}f_j)]$
CFV	correction factor variance	$[\sum_i(r_{ij}/\sigma_i^2)C_i^2]/[\sum_i(r_{ij}/\sigma_i^2)] - c_j^2$
CVG	coverage	$\sum_i r_{ij}$
DET	detector track	index of detector whose center falls at pixel j
BEM	beam sample map	reconstructed image from data made from spiked scene

coverage (CVG) map is the sum of the response function grids of all footprints within the field. The detector track (DET) map registers the footprint centers and helps visualize the detector scanning pattern. Artifacts due to low coverage may be diagnosed using the coverage maps. The remaining ancillary maps provide diagnostics for other less frequent artifacts.

The effective beam size in HIRES images depends on the response function and sample density in a complicated fashion, and may vary by factors of three over distances of several arcminutes (Fowler & Aumann 1994). In order to estimate the beam size at any given position and to see typical variation over the field, "beam sample maps" (BEM) are provided. These are produced from simulated detector data based on actual coverage geometry, with the simulation scene being a collection of spike sources against a smooth background. An image of the reconstructed spikes (beam sample map) is generated with all the same processing options as the actual image.

For more detailed information on the HIRES ancillary maps, see `http://www.ipac.caltech.edu/ipac/iras/hires_maps.html`.

3.3 Description of Processing

For an overview of the HIRES processing developed at IPAC, see `http://www.ipac.caltech.edu/ipac/iras/hires_over.html`. This section emphasizes the unique problems encountered in the *IRAS* Galaxy Atlas production.

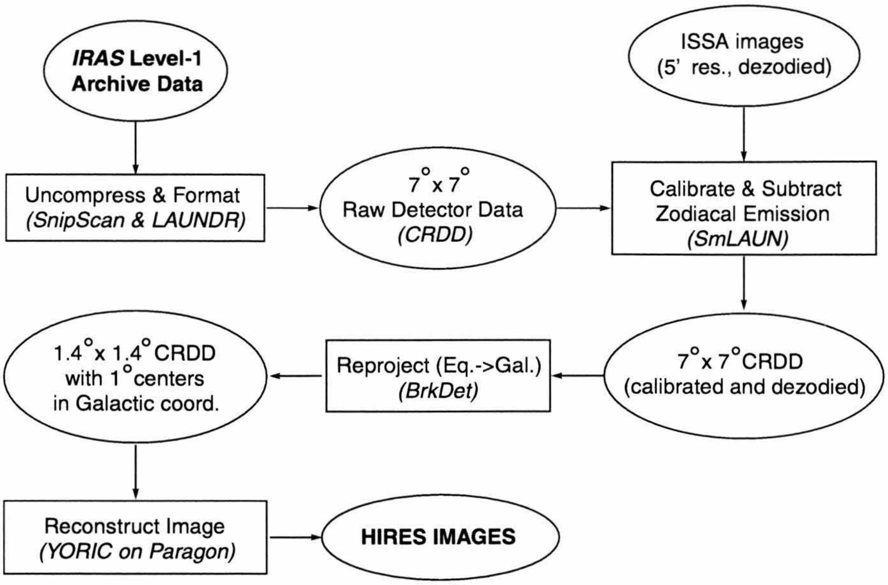

Figure 3.1: Outline of the IGA production pipeline.

3.3.1 Overview of the Production Pipeline

IRAS detector data, known as CRDD (calibrated, reconstructed detector data), grouped in 7° × 7° plates, reside in the *"Level 1 Archive"* at IPAC. The first step in the pipeline for mass production of HIRES images is to extract data covering a specific field from the archive and then perform calibration and various other preprocessing.

We take the 7° × 7° preprocessed and calibrated plates and use the algorithm described in Section 3.3.2 to subtract the zodiacal background emission. This step requires the corresponding ISSA image as supplement input (SmLAUN in Figure 3.1, Section 3.3.2).

Following the calibration and zodiacal subtraction, the detector files are broken into 1.4° × 1.4° fields, and reprojected into Galactic coordinates (from Equatorial) if required, with field centers separated by 1° (BrkDet in Figure 3.1, Section 3.3.3). The factor-of-two overlap is a conservative insurance against discontinuity across field boundaries (see Section 3.5.7), as local destriping and different flux bias (see Section 3.3.4) will be applied to each small field. The 1.4° × 1.4° size is also the maximal field size with complete coverage allowed within one Level 1 plate, given the 2 degree redundancy of the plates and arbitrary location and orientation of the small field relative to the Level 1 plate. Figure 3.2 illustrates the overlapping IGA fields, and the geometry and orientation of the Level 1 plates that determine the allowed IGA field size.

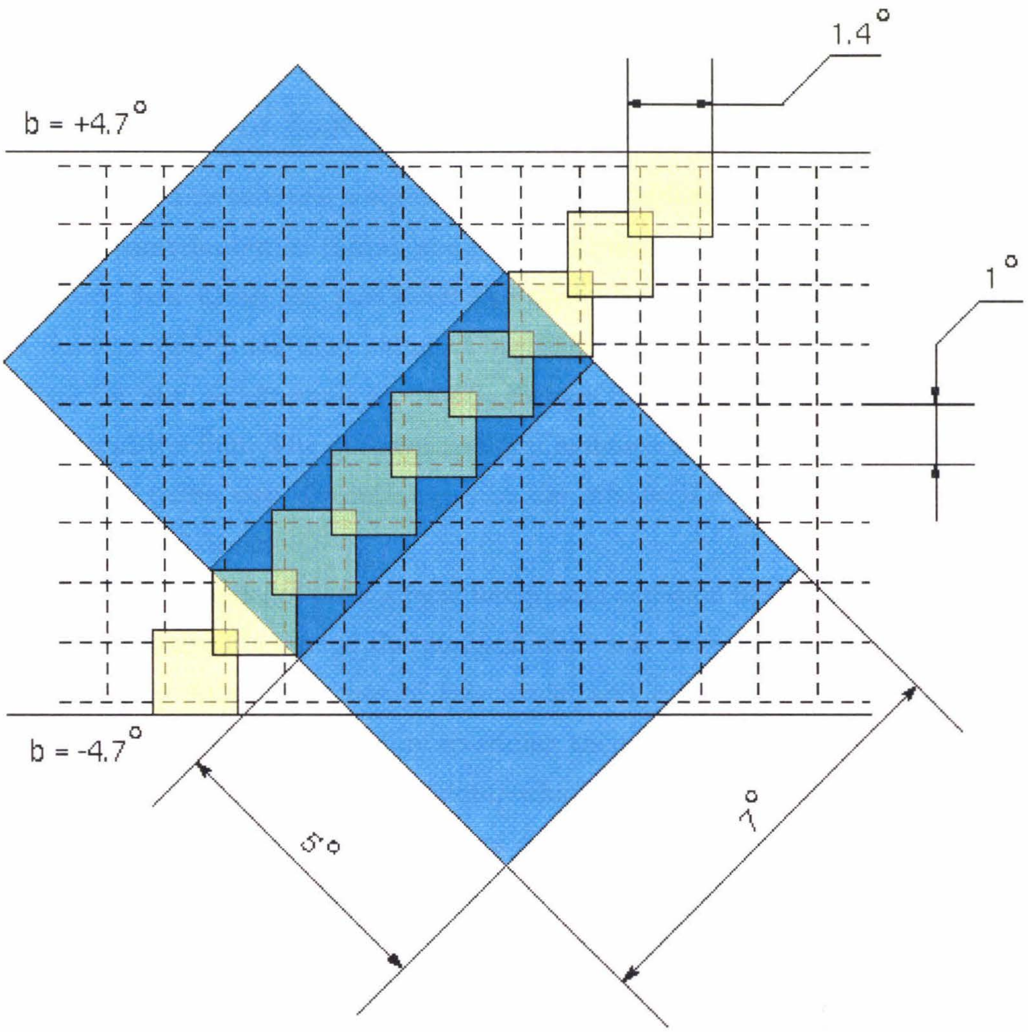

Figure 3.2: Geometry of IGA fields and Level 1 plates. The Atlas covers $-4.7° < b < 4.7°$. The small shaded areas represent IGA fields (1.4° × 1.4° on 1° centers), while the large ones represent Level 1 plates (7° × 7° on 5° centers). The configuration shows, in an extreme case, 1.4° × 1.4° is the largest IGA field that can be fully covered by any single Level 1 plate.

All operations described above are carried out on workstations.

The small field (1.4° × 1.4°) detector files are then processed into HIRES images, which is done on the Intel Paragon supercomputer. The basic algorithm for image reconstruction is described in Section 2.1, and the destriping algorithm in Section 2.3. The parallelization strategy is discussed in Section 3.4.

3.3.2 Subtraction of Zodiacal Emission

Zodiacal dust emission is a prominent source of diffuse emission in the *IRAS* survey. The zodiacal contribution to the observed surface brightness depends on the amount of interplanetary dust along the particular line-of-sight, an amount which varies with the Earth's position within the dust cloud. Consequently, the sky brightness of a particular location on the sky, as observed by *IRAS*, changes with time as the Earth moves along its orbit around the Sun. The different zodiacal emission level in different scanlines, if not subtracted, can cause step discontinuities in the images if adjacent patches of sky were observed at different times.

A physical model of the zodiacal foreground emission based on the radiative properties and spatial distribution of the zodiacal dust was developed by Good (1994). The *IRAS* Sky Survey Atlas made use of this model and subtracted the predicted zodiacal emission from the detector data before co-adding them.

However, the *IRAS* detector data, which serve as input to the IGA and other *IRAS* image products, still contain zodiacal emission. A preprocessing method has been developed to bring the raw detector data flux to a common level with the ISSA images, effectively subtracting the zodiacal emission component (Cao et al. 1996a). Nearby ISSA images (12.5° × 12.5°, 1.5′ pixels) were reprojected and mosaicked to cover the same field-of-view as a Level 1 plate (7° × 7°, 1′ pixels). A set of simulated data is then calculated from the mosaicked image, by running the actual *IRAS* scan pattern through this image,

$$F_i^{\mathrm{ISSA}} = \sum_j r_{ij} f_j^{\mathrm{ISSA}} \tag{3.1}$$

The difference between these simulated data and the real data is then used to determine the local zodiacal emission

$$D_i^{\mathrm{ZODY}} = \mathrm{median}(D_i - F_i^{\mathrm{ISSA}}) \tag{3.2}$$

where the median is taken for nearby footprints in the same scanline with a total spatial range of 1°. The zodiacal component is then subtracted

$$D_i^{\mathrm{NEW}} = D_i - D_i^{\mathrm{ZODY}} \tag{3.3}$$

and the new data output for use in image construction.

Because of the large spatial scale used in Eq. (3.2), the resulting zodiacal emission flux D_i^{ZODY} varies smoothly with a characteristic scale of $\sim 1°$. Therefore, the zodiacal subtraction process does not interfere with the high spatial frequency information inherent in the raw data, which is needed for the image reconstruction and resolution enhancement.

When the input ISSA image contains significant striping (at width around $7'$, that is, the distance of neighboring scan tracks, a much larger scale than the HIRES stripes), it is necessary to first smooth the ISSA image with a large kernel ($15'$) before doing the zodiacal subtraction. Otherwise, the calibrated detector data would retain the large distance scale offsets, and the gain compensation destriping described in Section 2.3 would not be able to estimate the gain variations correctly and would leave the wide stripes at different flux levels.

For validation of this procedure see the comparison of surface brightness (output HIRES vs. ISSA) described in Section 3.5.6.

3.3.3 Coordinate Transform and Reprojection

Each Level 1 plate covers a field of view of 7° × 7°, using a projection center local to the plate. The positions of detector footprints are stored in Equatorial coordinates using Cartesian projection (Greisen & Calabretta 1996; FITS keywords `RA---CAR, DEC--CAR`, B1950):

$$\begin{aligned} x &= \phi, \\ y &= \theta, \end{aligned} \tag{3.4}$$

where θ and ϕ are angles in the native coordinate system (Euler angles with respect to local great circles). Each Level 1 plate has its own projection center (C in Figure 3.3).

For the *IRAS* Galaxy Atlas, the Cartesian projection (FITS keywords `GLON-CAR` and `GLAT-CAR`) with reference point at the Galactic center is convenient, in which case l and b map linearly to x and y.

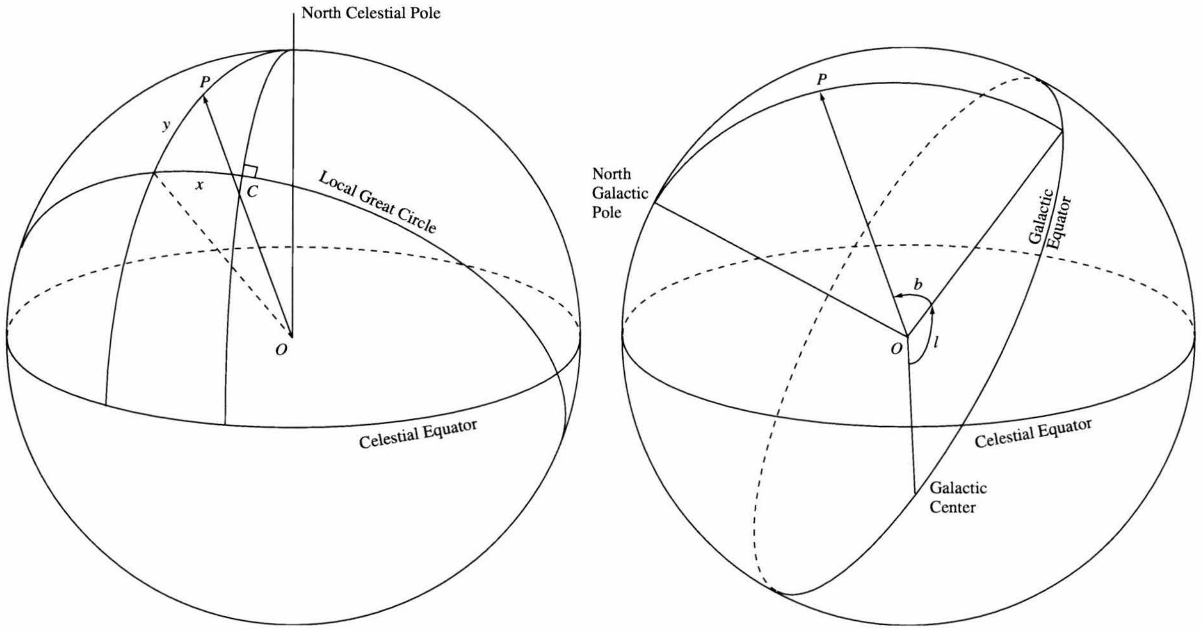

Figure 3.3: Reprojection of footprint coordinates. In the diagram on the left, RA and Dec are known for the Level 1 plate center C, and x (negative as shown here) and y are known for the footprint P. The components of the unit vector OP is then computed (in Equatorial system). As shown on the right, the vector OP is rotated to Galactic system, from which l and b of the footprint are obtained.

To transform the Equatorial coordinates of footprints stored in the Level 1 archive to Galactic, the following steps are done in BrkDet. For each footprint centered at P, a unit vector OP is computed in the equatorial system, using RA and Dec of the projection center C, and the x and y of P in the Cartesian projection system centered at C. Then the unit vector is rotated to the Galactic system (e.g., Green 1985), and l and b are obtained (see Figure 3.3). Coordinates and fluxes of footprints falling in each 1.4° × 1.4° field of view are grouped together and written out for the final image reconstruction step.

The tilt angle for each scan line, which is necessary for calculating the response function grid during image reconstruction, also needs to be redetermined in the Galactic coordinate system. For a scan line with n footprints located at $(x_i, y_i), i = 1, ..., n$, this was done by fitting a straight line through the x and y values, by minimizing $\sum_i \Delta_i^2$, where Δ_i is the distance from footprint i to the line. This gives the estimate for the tilt angle Φ, measured relative to the x axis

$$\Phi = \frac{1}{2} \arctan \frac{2 \sum_i x_i y_i - \overline{x}\,\overline{y}}{\sum_i x_i^2 - \overline{x}^2 - y_i^2 + \overline{y}^2} \tag{3.5}$$

where

$$\begin{aligned} \overline{x} &= \sum_i x_i / n \\ \overline{y} &= \sum_i y_i / n. \end{aligned} \tag{3.6}$$

For the molecular cloud fields (Orion, ρ Ophiuchi, and Taurus-Auriga), Equatorial coordinates were used (FITS keywords `RA---CAR` and `DEC--CAR`, B1950), and the Level 1 archive geometry was retained (no reprojection of the footprint data was performed). Each Level 1 plate (7° × 7° on 5° centers) was divided into 3 × 3 subfields of 2.5° × 2.5° each, on 2° centers, with the projection center the same as the Level 1 plate center. Therefore, the subfield images belonging to the same Level 1 plate are mosaickable without the need of reprojection, but special care needs to be taken when mosaicking subfields from different Level 1 plates. The use of Cartesian projection for Equatorial coordinates is closest to the native format of the *IRAS* data, but differs from the more commonly used orthographic projection (`SIN`) by about 7.5″ (0.5 pixels) at the edge of a Level 1 plate.

3.3.4 Issues Related to Flux Bias

Because of the nonlinear nature of the MCM algorithm, the resolution achieved by HIRES processing is not invariant under application of an additive *flux bias*:

$$D_i \longrightarrow D_i + F_{\mathrm{BIAS}}. \tag{3.7}$$

Generally, the closer to zero the data, the higher the resolution obtained. Alternatively, the more iterations, the higher the resolution obtained. To maximize both spatial resolution and throughput a flux bias is usually applied before the image reconstrution step, to bring the data close to zero and to achieve higher resolution at a given iteration. The applied flux bias is, however, subtracted from the output image, so that the surface brightness of the output image matches the original data.

For IGA processing, the flux bias is calculated in the BrkDet step, using the negative of the first percentile from the flux histogram in each $1.4^\circ \times 1.4^\circ$ field. In other words, the first percentile is used as the zero point in subsequent HIRES processing. The detector data having flux below the first percentile are discarded, since negative data are known to cause instabilities in the algorithm.

3.4 Parallelization

A flow chart of one iteration of the parallelized program is shown in Figure 3.4.

Profiling [1] a typical HIRES process showed that more than 95% of the total execution time was spent within the code which calculates the footprint and image correction factors (see Figure 3.4). In the parallel decomposition of the problem, each processor takes care of footprints from a set of scanlines. The reasons for doing this are as follows:

1. Small programming effort. The essence of the original HIRES architecture is left untouched.

2. Footprints in one leg share the same response function grid, except for a translation, which is basically the reason the original code processes the data one leg at a time. Keeping the whole leg in one processor is therefore a natural choice, which minimizes local memory usage.

3. As we discussed in Section 2.3, *IRAS* detectors have gain differences which are

---

[1] Profiling stands for timing analysis of subroutines in the program.

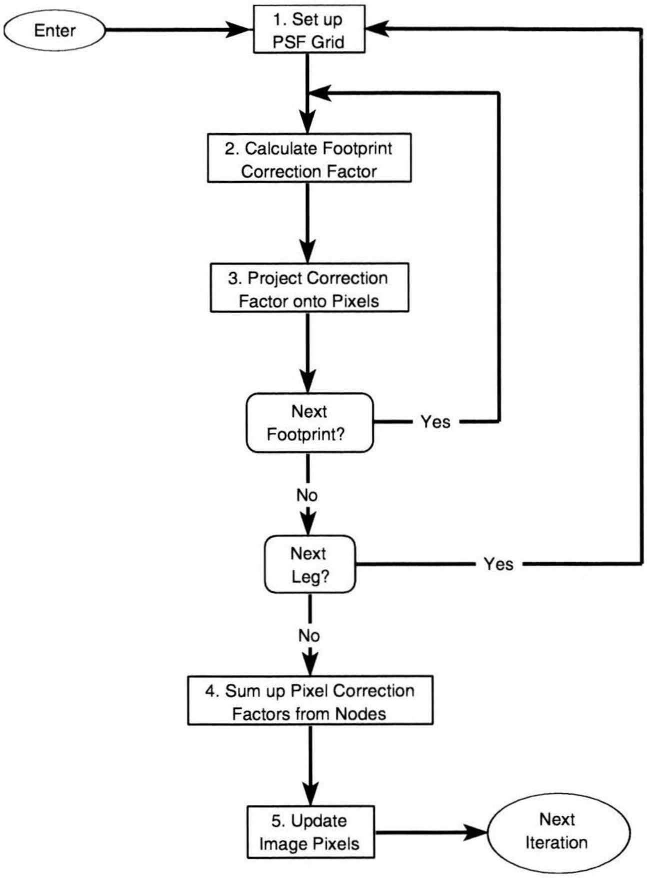

Figure 3.4: Flow chart of one iteration in the parallel program.

especially prominent for the 60 and 100 μm bands. The gain offset can be estimated from correction factors in the same leg, which came from the same detector.

Intermediate disk files for footprint data (D_i) and response function grids (r_{ij}) in the sequential program are replaced by arrays held in memory of the processors (step 1 in Figure 3.4), for the sake of easier programming and reduction in I/O. This is feasible in the parallel implementation as each processor now holds only a fraction of the entire data set.

Each node calculates the correction factor C_i's for its share of footprints (step 2), and projects them onto the pixels covered by the footprints (step 3). A global sum over all processors for the correction factor c_j's for each image pixel is performed at the end of each iteration (step 4), and the weighted average is taken, which is then applied to the image pixel value (step 5).

Decomposition in the image domain was not carried out for the $1^\circ \times 1^\circ$ field, eliminating the need for ghost boundary communication, which would be significant and complicated to code, due to the large size and irregular shape of the detector response function. This helped maintaining the parallel code similar in structure to the sequential one, making simultaneous upgrades relatively easy. The efficiency of the parallel program depends on the scan coverage of the field processed. The computation time is roughly proportional to the total coverage (i.e., total number of footprints), while the communication overhead is not related to footprints and is only dependent upon the image array size. So the efficiency is higher for a field with higher coverage.

For a large field (e.g., $7^\circ \times 7^\circ$), the detector measurements are broken into $1.4^\circ \times 1.4^\circ$ pieces with overlap 0.4°. Each $1.4^\circ \times 1.4^\circ$ field is loaded onto a subgroup of 8 or 16 processors. The overlap was chosen conservatively so that cropping the overlap after HIRES ensures smoothness at the boundaries. Mosaicked images made from adjacent fields turn out to be seamless to the human eye.

Currently the parallel program runs on the Paragon using Intel's NX communication routines under the OSF/1 operating system. It also runs on the Sandia-UNM Operating System along with the provided communication library (SUNMOS, Maccabe, McCurley, & Riesen 1993), which is available on Paragon and nCUBE, and provides significant performance increase.

The output images from the parallel computers are compared with those from the standard HIRES program running on a Sun SPARCstation. The differences are well within the range of numerical round-off errors. At the 20th iteration, the standard deviation of

Table 3.2. Speed Comparisons for 60 μm Band of M51

Platform	Execution Time
Sun SPARCstation 2	720 sec
Single node of the Paragon	640 sec
8 nodes of the Paragon	137 sec

(NewImage - OldImage) / OldImage averages to about 10^{-4}.

The global sum operation, which collects pixel correction factors from different nodes, is the primary source of communication overhead in the parallel program.

The executable code was compiled and linked with a math library conformant to the IEEE 754 standard, and the compiler options were fine-tuned to give the best execution speed. For the 60 μm band of M51 (baseline removed data), a time comparison is shown in Table 3.2.

A speed increase of about 7 times is achieved with 16 processors and 5 times with 8 processors for a 1° × 1° field. Equivalently, a 64 square degree field can be processed using 512 nodes, with a speedup factor of 320. For production runs on the Paragon, we customarily use 128 nodes to process 16 small fields simultaneously. Each band-plate would therefore take roughly 1.5 hours of real time. Various scripts are used to automate the data transfer and program launching.

3.5 Characteristics of the Images

To test the authenticity of high resolution features produced by the MCM algorithm, Aumann, Fowler, and Melnyk (1990) compared the 60 μm HIRES image of M101 with the *IRAS* Point Source Catalog and previously known H II regions (based on observations at ultraviolet, infrared, and radio wavelengths). Also Rice (1993) examined the structural reliability of HIRES maps for three test galaxies: M51, M33, and NGC 6822 using the following truth tables: (1) a far-infrared KAO [2] map of M51, (2) optical light

---

[2] Kuiper Airborne Observatory, an airplane operated by NASA Ames Research Center that flies in the Earth's stratosphere carrying a 36-inch reflecting telescope.

photographic images of the three test galaxies, (3) four additional types of "high-resolution" maps constructed from independent *IRAS* data, and (4) a simulated map of the radio emission of bright H II regions in M33 constructed from a catalog of 20 cm radio continuum sources in the galaxy. We've compared the gain compensation destriped images with the original HIRES images for the above fields (and numerous others), and have found good agreement in the reconstructed features (except for the lack of striping).

In this section "IGA(1)" denotes the 1st iteration IGA images, and "IGA(20)" the 20th. The resolution, photometric accuracy, positional accuracy, surface brightness accuracy, mosaic property, and residual hysteresis effect of the images are discussed and quantified.

3.5.1 Resolution

The diffraction limit of the *IRAS* 0.6m telescope is $50''$ and $84''$ at 60 and 100 microns, respectively. The effective beam of the co-added *IRAS* data is much larger, typically $2.0' \times 4.7'$ at 60 μm and $3.8' \times 5.4'$ at 100 μm due to the large and rectangular *IRAS* detectors. The MCM algorithm makes use of the geometric information in the large number of redundant tracks with differing scan angles to extract higher spatial resolution, which in some cases can approach the diffraction limit of the telescope (Rice 1993). The effective beam size in HIRES images depends on the response function and sample density in a complicated fashion. The resolution also depends on the magnitude of the point source relative to the effective background (see also Section 3.3.4).

The effective resolution of a given field can be estimated from the corresponding BEM maps produced from simulated data (also see Section 2.1 and Table 3.1). To generate the BEM maps artificial point sources are added to the smoothed data, which then undergo HIRES processing. Specifically, point sources are identified and removed from IGA(20) image: the image, further smoothed, provides a model background to which regularly spaced ($12'$) point sources are added. The magnitude of the planted point sources is adjusted according to the dynamic range of the IGA(20) image: the pixel intensity is set to 20 × (99% quantile − 50% quantile) of the IGA image histogram (plus the background). The numerical value of 20 approximately converts the flux from per unit beam to flux per unit pixel. This arbitrary choice of flux is meant to represent a typical point source which is strong enough with respect to the local Galactic background to benefit from high-resolution

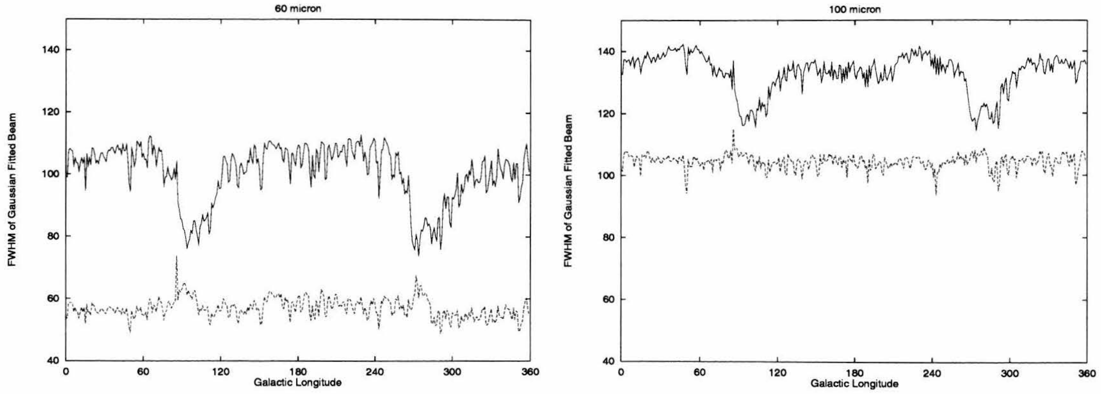

Figure 3.5: Dependence of beam size on Galactic longitude. Left and right plots are for 60 and 100 μm respectively. The top and bottom curves in each figure are the FWHM of Gaussian fitted beam along the major and minor axes respectively. The regions in the Galactic plane which had intersecting scan lines in the *IRAS* survey are seen as two dips in the major axis curves (better resolution due to extra geometrical information).

processing. A set of simulated data is then generated from the artificial image, from which the BEM map is reconstructed through HIRES.

A Gaussian profile is fitted to the reconstructed point sources in the BEM maps, and the FWHM along the major and minor axes are taken as the measure for the achieved resolution.

Figure 3.5 demonstrates the dependence of the resolution upon longitude across the Galactic plane. The plotted major and minor axis FWHM were averaged over latitude. Two obvious dips are seen in the major axis curves, both in 60 and 100 μm, near $l = 100°$ and $l = 280°$. These two areas in the Galactic plane featured near-perpendicular intersecting scanlines in the *IRAS* survey, and the extra geometric information in the data gives rise to the increased resolution.

The typical resolution of the IGA images (20th iteration) is seen to be $1.0' \times 1.7'$ at 60 μm and $1.7' \times 2.2'$ at 100 μm, which represents a substantial improvement over the co-added images. However, the HIRES processing has not been pushed to its limit in the trade off to complete the IGA Atlas in a timely manner. HIRES reprocessing using more than 20 iterations can be expected to push the resolution closer to the diffraction limit, at least in cases where the point source ringing artifact is minor.

To investigate the dependence of resolution on source strength relative to background level, BEM maps were generated for simulated point sources ranging from 1 to

10,000 Jy in strength. The background intensity level of the test field near $l = 120°$ was 53.94 MJy sr^{-1} and 165.05 MJy sr^{-1} at 60 and 100 μm, respectively. Integrated over the effective solid angle of the *IRAS* detectors, 6.25×10^{-7} and 13.54×10^{-7} sr, the detector fluxes due to the local background become 33.7 and 223 Jy, respectively. To find the effective background during HIRES processing, the flux bias value from the FITS header (see Section 3.3.4) can be converted from W m^{-2} to Jy through division by the conversion factors 2.58×10^{-14} or 1.00×10^{-14} at 60 and 100 μm, respectively, and then subtracted from the corresponding local background flux. In this test case, zero flux bias was used, giving simply 33.7 and 223 Jy for the processing background at 60 and 100 μm, respectively, which is the effective local background felt by the point source during HIRES processing.

The results plotted in Figure 3.6 show that the IGA(20) resolution is at least a factor of two better than the co-added IGA(1) resolution. Also, the resolution significantly improves for point sources stronger than the processing background of 33.7 and 223 Jy at 60 and 100 μm, respectively. Furthermore, when source-to-background contrast reaches about 20, the achieved resolution becomes insensitive to the background. The resolution in other fields/regions should behave in the same qualitative fashion when the local processing background is computed as above.

Figure 3.6 also shows the additional effect that offset compensation destriping (Section 2.3) gives comparable but slightly poorer resolution than standard HIRES destriping, especially along the major axis (cross scan) direction.

It should also be noted that the actual beams of the IGA images are not Gaussian. The most prominent deviation of the beam from a two-dimensional Gaussian is due to the ringing artifact (Section 3.6.2). Rice (1993) gave a detailed account of the HIRES beams.

3.5.2 Photometric Accuracy

To test photometric accuracy, thirty-five relatively isolated point sources (with a well-defined background) were selected. All sources have flux density > 10 Jy and are spatially unresolved as measured by the Correlation Coefficient (CC) flag in the Point Source Catalog. The IGA point source flux densities were measured using an aperture photometry program developed at IPAC, in which the median pixel intensity within an annulus (radius $5'$–$7'$) centered at the point source position (taken from the PSC) is taken as the background intensity. Two estimates of the point source flux density are then made, using the total

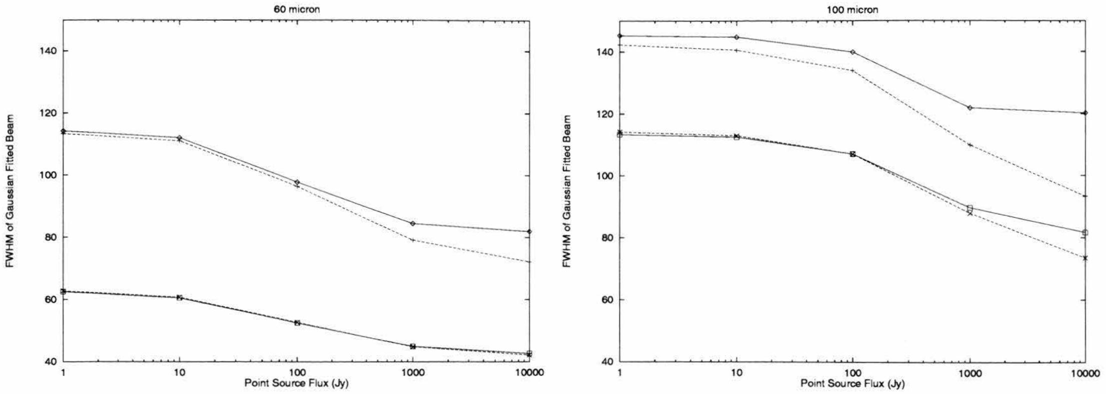

Figure 3.6: Dependence of beam size on source flux density. Resolution significantly improves for sources stronger than the local processing background of 33.7 Jy at 60 μm and 223 Jy at 100 μm. Results with destriping (solid lines), and non-destriping (dashed lines) show the IGA destriper has comparable resolution to standard HIRES, the most notable difference being along the 100 μm major axis.

fluxes within $5'$ and $7'$ radius from the PSC position (minus the background intensity × the number of pixels). For sources chosen for the photometry test, these two values are usually sufficiently close to each other, indicating a well-defined background level. The average of these two values is taken as the point source flux density from the IGA image, and compared against the value from the PSC.

The result of the comparison is shown in Table 3.3. Table 3.4 summarizes the statistic correlation between IGA and PSC flux density values.

An overall offset (12%) between the IGA(1) and PSC flux densities is seen at 60μm, which is however, not present at 100 μm (1%). One possible explanation for the 60 μm offset is the different data calibration used, specifically the hysteresis correction. The IGA and other recent *IRAS* image products are based on the final *IRAS* Pass 3 calibration (described in detail in *IRAS* Sky Survey Atlas Explanatory Supplement 1994). This calibration includes a hysteresis correction at both 60 and 100 μm (see Section 3.5.8). The PSC however is based on *IRAS* Pass 2 CRDD data, which were corrected after the fact to the Pass 3 calibration. One significant difference is the way in which hysteresis was treated: the PSC applied a hysteresis correction only at 100 μm (*IRAS* Catalogs and Atlases: Explanatory Supplement 1988). The lack of hysteresis correction at 60 μm for PSC sources, particularly important for the Galactic plane where hysteresis is strongest, provides one explanation for why there is a systematic offset at 60 μm, but not at 100 μm,

Table 3.3. Comparison of PSC and IGA Flux Densities

Source (IRAS PSC)	PSC Position (Galactic)	Flux Density (Jy) PSC		IGA(1)		IGA(20)	
		60μm	100μm	60μm	100μm	60μm	100μm
00270 + 6334	G120.5608 + 1.0782	59.91	97.30	76.248	119.645	79.770	132.628
00338 + 6312	G121.2980 + 0.6587	356.60	685.00	404.131	780.675	405.239	823.987
01243 + 6212	G127.1116 − 0.1152	31.30	72.97	36.112	64.307	36.292	73.700
07519 − 3404	G250.0056 − 3.3432	14.41	18.46	14.162	15.688	14.846	14.086
08011 − 3627	G253.0220 − 2.9951	26.12	11.96	27.792	17.614	29.650	16.778
08005 − 2356	G242.3643 + 3.5825	29.83	10.35	27.492	8.575	29.297	11.050
02071 + 6235	G131.8557 + 1.3320	32.90	57.23	40.276	64.815	45.801	75.912
02044 + 6031	G132.1572 − 0.7257	387.60	465.70	422.677	457.721	444.238	480.292
01304 + 6211	G127.8138 − 0.0226	194.00	50.18	190.435	47.181	197.142	51.815
02541 + 6208	G137.0688 + 3.0025	74.87	127.80	80.658	121.714	84.828	126.268
02175 + 5845	G134.2729 − 1.8974	32.44	61.79	38.913	66.829	39.420	85.632
02192 + 5821	G134.6198 − 2.1962	40.59	14.99	44.688	16.592	43.510	18.510
01420 + 6401	G128.7764 + 2.0125	128.80	234.40	164.751	231.846	171.442	251.556
01160 + 6529	G125.8047 + 3.0469	33.46	41.47	37.664	43.549	37.131	39.226
01145 + 6411	G125.7773 + 1.7256	57.71	80.60	72.848	94.677	74.204	95.384
20180 + 3558	G074.4973 − 0.1138	165.30	272.10	180.903	236.454	186.116	275.078
20306 + 3749	G077.4760 − 1.0817	187.00	316.30	194.880	272.214	183.857	319.383
20145 + 3645	G074.7535 + 0.9127	166.20	173.20	193.853	230.194	191.798	260.233
20116 + 3605	G073.8752 + 1.0260	242.20	267.00	247.650	234.989	242.372	347.049
20193 + 3448	G073.6944 − 0.9990	98.64	87.49	85.756	67.030	89.240	74.476
20144 + 3526	G073.6522 + 0.1946	432.60	364.10	503.915	355.433	417.726	268.931
20134 + 3444	G072.9526 − 0.0254	47.08	112.90	51.390	88.165	54.138	108.333
20142 + 3615	G074.2961 + 0.6794	42.29	83.16	53.566	75.882	42.222	67.248
04365 + 4717	G157.6277 + 0.5289	32.51	55.33	34.552	63.570	36.884	67.212
07466 − 2631	G242.9404 − 0.4496	18.38	37.21	26.107	44.276	27.876	51.822
07466 − 2607	G242.5847 − 0.2401	13.28	28.25	12.806	23.050	13.404	31.760
07427 − 2400	G240.3153 + 0.0713	619.40	745.40	674.641	778.032	675.000	816.299
12437 − 6218	G302.3893 + 0.2788	408.40	679.60	475.944	686.172	457.197	711.096
12405 − 6219	G302.0211 + 0.2543	250.70	429.60	276.257	446.146	320.096	496.692
12377 − 6237	G301.7102 − 0.0561	123.90	196.80	141.933	163.958	158.350	204.141
12413 − 6332	G302.1507 − 0.9487	240.70	259.80	259.115	269.452	277.910	302.102
05378 + 2928	G178.9940 − 0.5414	9.46	22.36	10.740	23.204	10.744	23.257
16251 − 4929	G334.7223 − 0.6527	520.00	710.80	661.577	675.769	642.504	587.205
12268 − 6156	G300.4020 + 0.5459	193.00	269.60	237.519	317.504	248.148	349.192
12091 − 6129	G298.2623 + 0.7401	628.30	796.40	670.887	858.152	661.079	864.247

Table 3.4. Photometry Comparison Statistics

Band (μm)	Quantity	Mean	Std. Dev.
60	IGA(1)/PSC	1.12	0.11
60	IGA(20)/PSC	1.14	0.13
60	IGA(20)/IGA(1)	1.02	0.07
100	IGA(1)/PSC	1.01	0.16
100	IGA(20)/PSC	1.11	0.19
100	IGA(20)/IGA(1)	1.10	0.15

between the IGA(1) and PSC fluxes.

In addition, Table 3.4 shows there is a growth in flux from 1st to 20th iteration which is small (2%) for the 60 μm band, but significant (10%) for the 100 μm band. Analysis shows the effect is caused by depression of the background due to the ringing artifact. In the Galactic plane, where the background emission is strong and structured, the largest contributor to the flux uncertainty is the background determination (Fich & Terebey 1996). The total flux within the selected aperture is comprised of the source flux plus a background contribution (background × area). For the photometry sample, the ratio of background flux to source flux is 1.8 at 60 μm and 6.7 in the 100 μm band. In addition the background level systematically decreases on average by 1.7% for 60 μm, and 1.8% at 100 μm due to ringing in the $5' - 7'$ annulus. This leads to an apparent flux increase from 1 to 20 iterations of $1.8 \times 1.7\% = 3\%$ at 60 μm and $6.7 \times 1.8\% = 12\%$ in the 100 μm band, which is in good agreement with results of Table 3.4.

To compensate for the systematically low background levels we recomputed the IGA(20) source fluxes using IGA(1) background levels. The resulting fluxes show no systematic offset (mean of IGA(20)/IGA(1) = 0.99) and better correlation with IGA(1) fluxes (standard deviation = 0.10). This technique of using IGA(1) backgrounds to calculate IGA(20) fluxes is recommended whenever the most stable and accurate photometry is required.

The growth in flux found for IGA point sources is not a universal property of

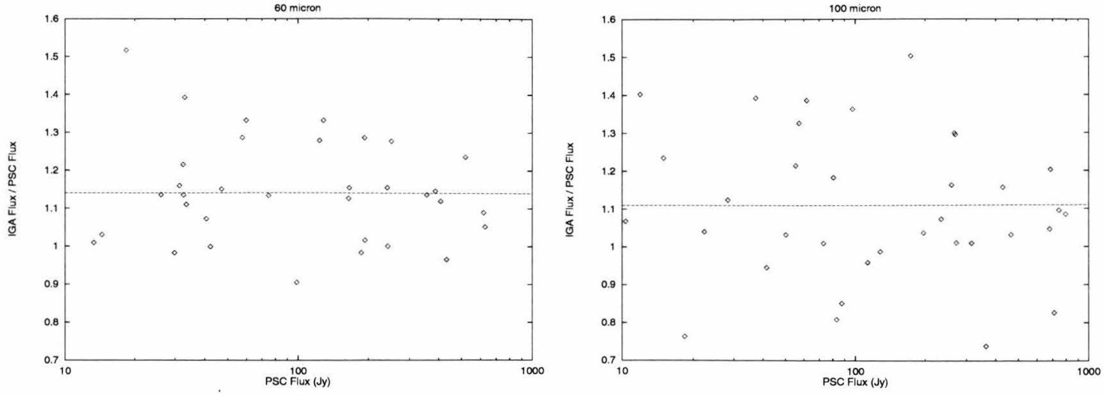

Figure 3.7: The ratio of (IGA(20) Flux / PSC Flux) vs. PSC Flux shows no trend with source strength. Offsets are discussed in text. Thirty-five sources are plotted in each wavelength band.

HIRES processing. In a HIRES study of interacting galaxy pairs, Surace et al. (1993) found HIRES fluxes systematically decreased by 20% from iteration = 1 (FRESCO) to iteration = 20, a result they attributed to the small extended nature of the sample. Since the MCM algorithm fundamentally conserves flux, the effect is either due to a systematic increase in the background, or to redistribution of flux outside the photometric aperture. The use of the IGA(1) background to compute the IGA(20) flux is a technique that can help determine the cause of such systematic trends.

Figure 3.7 plots the dependence of (IGA(20) flux / PSC flux) on the PSC flux. There is no trend with source flux, apart from the previously discussed offsets.

3.5.3 Size Dependent Flux Correction

The estimation of flux for extended sources ($> 4' - 40'$) may involve a size dependent flux correction, also known as the AC/DC correction. The *IRAS* detectors had a dwell-time dependent responsivity change. Hence, the gain changes as a function of source size: at the *IRAS* survey speed of 3.85 arcmin/s, the gains leveled off for structure on the order of $40'$ in extent. This effect was band-dependent and largest at 12 μm. Thus, there are two calibrations for the *IRAS* data, the calibration appropriate for point sources, known as the AC calibration, and the calibration appropriate to very extended structure, known as the DC calibration. To bring point source fluxes measured from DC-calibrated products to the AC (same as the PSC) calibration, the fluxes must be divided by 0.78, 0.82, 0.92 and 1.0 at 12, 25, 60 and 100 μm, respectively. The *IRAS* Galaxy Atlas uses the AC calibration, while the ISSA images are on the DC scale.

Point source fluxes obtained by aperture photometry with appropriate background subtraction on AC calibrated images should be consistent with the PSC. It should be noted that neither calibration is strictly correct for structure on spatial scales intermediate between point sources and 30′ in size. Intermediate-scale corrections and uncertainties can be estimated from the plots in the *IRAS* Catalogs and Atlases: Explanatory Supplement (1988).

3.5.4 Calibration Uncertainty

The measurement uncertainty derived from point sources (Table 3.4) for the IGA(1) images is 11% and 16% at 60 and 100 μm, respectively. Given the isolated nature of the sources, these uncertainties represent a best case. A better estimate of the measurement uncertainty in more complex regions is given by Fich & Terebey (1996), who find 17% and 18% for the flux measurement uncertainty of at 60 and 100 μm, respectively, for a sample of outer Galaxy star forming regions.

In some cases systematic instrumental effects also contribute significantly to the flux uncertainty. The *IRAS* calibration for point sources is accurate, albeit affected by residual hysteresis at 60 and 100 μm in the Galactic plane. As described in the previous section, there is a 12% systematic uncertainty at 60 μm between the IGA(1) and PSC. At 100 μm the uncertainty due to residual hysteresis is less than 5% over most of the Galactic plane, but approaches a maximum of 20% near the Galactic center.

For small but extended (5′ – 20′) sources the situation is complex. The size-dependent flux correction, the so-called AC/DC effect (see Section 3.5.3) is typically about 10% or less. However the detector response is not well-behaved for bright extended sources: above 100 Jy the *IRAS* Explanatory Supplement quotes uncertainties of 30% at 60 μm and 70% at 100 μm (*IRAS* Catalogs and Atlases: Explanatory Supplement 1988).

Prominent in the IGA is diffuse Galactic emission associated with H I, which varies on a scale of a few degrees. The *IRAS* – *COBE* comparison gives an indication of the calibration uncertainty. Over angular scales larger than 10° the *IRAS* calibration differs systematically from that of *COBE* by 13% and 28% at 60 and 100 μm, respectively (*IRAS* Sky Survey Atlas Explanatory Supplement 1994).

The ISSA survey was used as large scale surface brightness truth table for the

IGA. This implies that defects or uncertainties introduced by the ISSA processing extend to the IGA as well (see Section 3.6.4). At 60 and 100 μm, residuals associated with zodiacal emission model can approach 1 – 2 MJy sr^{-1} in the ecliptic plane (Galactic center and anti-center directions), but are typically far less (e.g., Fich & Terebey 1996). For more information consult the ISSA Explanatory Supplement (*IRAS* Sky Survey Atlas Explanatory Supplement 1994).

3.5.5 Positional Accuracy

IRAS Point Source Catalog positions were used as "truth tables" for positional accuracy test of the *IRAS* Galaxy Atlas.

Positions were computed for the same sample of thirty-five sources used in the photometry comparison. For each source, a circular area with radius $5'$ was defined (centered at the PSC position), and the area's flux weighted centroid was taken as the point source position implied by the IGA image and compared against the PSC position.

Table 3.5 shows the result of the comparison. For the 60 μm band, the distances between the IGA position and PSC position have an average of $7.6''$ and standard deviation $5.6''$, while for 100 μm, there is a $7.1'' \pm 4.1''$ difference.

The PSC quoted error ellipses corresponding to 95% confidence level for the source positions. The major and minor axes of the error ellipse correspond approximately to the cross- and in-scan directions. For each source, we projected the IGA position along the major and minor axes of the error ellipse centered at the PSC position. The mean deviations from the PSC position were found to be similar along the major and minor axis directions, and do not scale with the length of the major and minor axes. This indicates the positional errors produced by the MCM alrogithm are due to non-systematic effects unrelated to the *IRAS* scan pattern and detector geometry.

The HIRES algorithm can cause systematic positional shifts if the coverage changes abruptly. In cases where positional accuracy is important, the CVG maps should be checked for the presence of discontinuities or steep ($< 5'$) coverage gradients. The sense of the artifact is to shift source positions sytematically down and along the coverage gradient.

Table 3.5. Comparison of PSC and IGA Positions

Source	Position (Galactic, °)						|PSC − IGA|	
(IRAS PSC)	PSC		IGA 60μm		IGA 100μm		(″)	
	l	b	l	b	l	b	60μm	100μm
00270 + 6334	120.5608	1.0782	120.5622	1.0797	120.5628	1.0804	7.4	10.7
00338 + 6312	121.2980	0.6587	121.2974	0.6561	121.2990	0.6590	9.6	3.8
01243 + 6212	127.1116	−0.1152	127.1108	−0.1155	127.1110	−0.1163	3.1	4.5
07519 − 3404	250.0056	−3.3432	250.0030	−3.3412	250.0032	−3.3421	11.8	9.5
08011 − 3627	253.0220	−2.9951	253.0210	−2.9960	253.0216	−2.9951	4.8	1.4
08005 − 2356	242.3643	3.5825	242.3653	3.5846	242.3619	3.5831	8.4	8.9
02071 + 6235	131.8557	1.3320	131.8539	1.3314	131.8544	1.3325	6.8	5.0
02044 + 6031	132.1572	−0.7257	132.1584	−0.7257	132.1581	−0.7243	4.3	6.0
01304 + 6211	127.8138	−0.0226	127.8140	−0.0210	127.8123	−0.0202	5.8	10.2
02541 + 6208	137.0688	3.0025	137.0696	3.0039	137.0695	3.0037	5.8	5.0
02175 + 5845	134.2729	−1.8974	134.2700	−1.8954	134.2703	−1.8938	12.7	16.0
02192 + 5821	134.6198	−2.1962	134.6205	−2.1954	134.6206	−2.1963	3.8	2.9
01420 + 6401	128.7764	2.0125	128.7749	2.0115	128.7740	2.0118	6.5	9.0
01160 + 6529	125.8047	3.0469	125.8044	3.0469	125.8053	3.0462	1.1	3.3
01145 + 6411	125.7773	1.7256	125.7733	1.7210	125.7764	1.7234	21.9	8.6
20180 + 3558	74.4973	−0.1138	74.4978	−0.1129	74.4970	−0.1125	3.7	4.8
20306 + 3749	77.4760	−1.0817	77.4765	−1.0828	77.4758	−1.0829	4.3	4.4
20145 + 3645	74.7535	0.9127	74.7529	0.9116	74.7531	0.9111	4.5	5.9
20116 + 3605	73.8752	1.0260	73.8739	1.0237	73.8741	1.0239	9.5	8.5
20193 + 3448	73.6944	−0.9990	73.6956	−0.9984	73.6943	−0.9988	4.8	0.8
20144 + 3526	73.6522	0.1946	73.6542	0.1962	73.6547	0.1971	9.2	12.7
20134 + 3444	72.9526	−0.0254	72.9543	−0.0244	72.9542	−0.0245	7.1	6.6
20142 + 3615	74.2961	0.6794	74.2965	0.6776	74.2963	0.6784	6.6	3.7
04365 + 4717	157.6277	0.5289	157.6315	0.5351	157.6299	0.5323	26.2	14.6
07466 − 2631	242.9404	−0.4496	242.9418	−0.4529	242.9410	−0.4526	12.9	11.0
07466 − 2607	242.5847	−0.2401	242.5900	−0.2424	242.5891	−0.2428	20.8	18.6
07427 − 2400	240.3153	0.0713	240.3157	0.0707	240.3153	0.0709	2.6	1.4
12437 − 6218	302.3893	0.2788	302.3894	0.2779	302.3888	0.2764	3.2	8.8
12405 − 6219	302.0211	0.2543	302.0208	0.2546	302.0208	0.2542	1.5	1.1
12377 − 6237	301.7102	−0.0561	301.7098	−0.0550	301.7096	−0.0550	4.2	4.5
12413 − 6332	302.1507	−0.9487	302.1501	−0.9483	302.1485	−0.9485	2.6	8.0
05378 + 2928	178.9940	−0.5414	178.9968	−0.5401	178.9960	−0.5414	11.1	7.2
16251 − 4929	334.7223	−0.6527	334.7210	−0.6520	334.7213	−0.6518	5.3	4.8
12268 − 6156	300.4020	0.5459	300.4012	0.5441	300.4003	0.5446	7.1	7.7
12091 − 6129	298.2623	0.7401	298.2631	0.7411	298.2616	0.7415	4.6	5.6

Table 3.6. Comparison of Surface Brightness *

Position	Band (μm)	IGA(1) vs. ISSA	IGA(20) vs. ISSA
G000.5 + 0.5	60	0.024 ± 0.064	0.013 ± 0.100
G121.5 + 0.5	60	0.017 ± 0.035	0.008 ± 0.112
G126.5 − 0.5	60	0.007 ± 0.040	−0.010 ± 0.119
G218.5 − 0.5	60	0.006 ± 0.033	−0.002 ± 0.080
G000.5 + 0.5	100	0.031 ± 0.057	0.020 ± 0.083
G121.5 + 0.5	100	0.003 ± 0.016	−0.003 ± 0.068
G126.5 − 0.5	100	0.008 ± 0.028	−0.004 ± 0.081
G218.5 − 0.5	100	0.005 ± 0.016	0.000 ± 0.047

* Comparison was done for 1° radius circles centered at positions shown in first column. Differences are represented by mean ± standard deviation of the quantity log(IGA/ISSA). AC/DC correction was applied before the comparison.

3.5.6 Surface Brightness Accuracy

To test the surface brightness of zodiacal-subtracted IGA images, they were rebinned to ISSA geometry (using boxcar averaging) and compared pixel-by-pixel against the ISSA images. The AC/DC correction was applied, i.e., the IGA surface brightness was multiplied by 0.92 and 1.0 at 60 and 100 μm, respectively, before calculating the surface brightness correlation (see Section 3.5.3). The standard deviation of the pixel-by-pixel ($1.5'$) difference is less than 6% for IGA(1) vs. ISSA, and less than 12% for IGA(20) vs. ISSA (see Table 3.6). The difference is larger at 20th iteration as the rebinned IGA images are still sharper than ISSA, while the 1st iteration IGA images have a resolution similar to the $4'$ to $5'$ of ISSA. No systematic offset was found between IGA and ISSA after applying the AC/DC correction.

Figure 3.8 shows typical scatter plots of log(IGA/ISSA) vs. ISSA intensities.

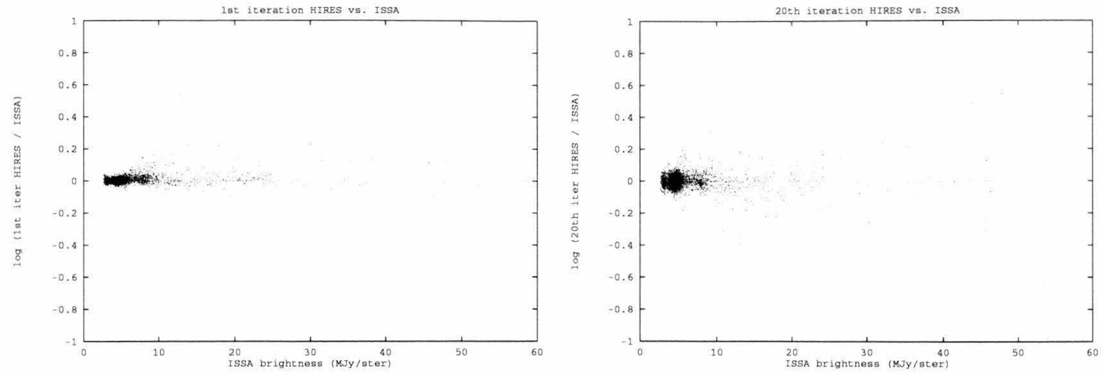

Figure 3.8: Comparison of IGA and ISSA surface brightness in a 1° radius circular area centered at G218.5 − 0.5 (60 μm) shows no systematic offset. Left: comparison of IGA(1) vs. ISSA; right: comparison of IGA(20) vs. ISSA. Vertical: log of IGA/ISSA ; horizontal: ISSA intensity in MJy sr^{-1}. The AC/DC correction was applied before calculating surface brightness ratio.

3.5.7 Mosaic Property

The geometry of the IGA images allows them to be mosaicked without any reprojection, hence no smoothing is required and the original resolution can be retained in the mosaicked images. To reduce edge discontinuities, the images should first be cropped to 1° × 1° from 1.4° × 1.4° with the centers unshifted before mosaicking. No intensity offset needs to be applied to the different subfields. In most cases the mosaicked image is seamless to the human eye.

Quantitatively, within a chosen Level 1 plate in the W3-5 region, pixel intensity ratios were calculated for 1-pixel wide edges covered by neighboring subfields after cropping the subfields to slightly larger than 1°×1°. Table 3.7 summarizes the intensity ratio statistics for both the 1st and 20th iteration images.

A total of 10122 pixels in 42 1° edges were used in the calculation. For 20th iteration images, the standard deviation of the ratio amounts to 0.51% and 0.23% for 60 μm and 100 μm respectively.

Intensity ratio statistics were also calculated for cross-Level 1-plate boundaries, using a total of 8194 pixels in 34 edges, each being 1° long. Again for 20th iteration images, the standard deviations are 1.5% and 0.46% for band 3 and 4. The match is worse than that of intra-plate edges, since the zodiacal subtraction was done separately for each Level 1 plate (see Section 3.3.2).

Table 3.7. Statistics of Pixel Intensity Ratios for Neighboring Subfields

Iteration	Band (μm)	Cross Level 1 Plate	Number of Pixels	Std. Dev. of Ratio
1	60	no	10122	0.14%
1	60	yes	8194	0.52%
1	100	no	10122	0.08%
1	100	yes	8194	0.18%
20	60	no	10122	0.51%
20	60	yes	8194	1.5%
20	100	no	10122	0.23%
20	100	yes	8194	0.46%

The better boundary match (smaller deviation) at 100 μm can be understood from the poorer resolving power of HIRES at 100 μm than at 60 μm, which decreases the resolution difference between subfields caused by the different flux bias levels used in the image reconstruction process (see Section 3.3.4).

3.5.8 Residual Hysteresis

The *IRAS* detectors showed photon induced responsivity enhancement, known as the hysteresis effect, especially in the 60 and 100 μm bands. The effect is prominent when the scan lines pass the Galactic plane (e.g., *IRAS* Catalogs and Atlases: Explanatory Supplement 1988, Chapter VI) and thus a concern for the IGA survey. The final *IRAS* Pass 3 calibration, on which both the IGA and ISSA are based, employed a physically based detector model to correct for the hysteresis. However the technique could not correct variations that were more rapid than $\sim 6°$ in spatial scale (*IRAS* Sky Survey Atlas Explanatory Supplement 1994, Chap. III). This section quantifies the residual hysteresis near the Galactic plane in the ISSA data, which should also describe the residual hysteresis present in the IGA.

In the *IRAS* survey, a given region can be covered by up to 3 scans carried out at different times, known as Hours CONfirming (HCON) scans. HCON 1 and HCON 2 were separated by up to several weeks, while HCON 3 was taken roughly 6 months after. [3] This meant HCON 3 usually passed the Galactic plane along the opposite direction of HCON 1 and 2, since *IRAS* followed a Sun-synchronous orbit and the telescope always pointed approximately 90° away from the Sun.

Figure 3.9 illustrates the effect on quoted flux values from the different HCONs caused by the photon induced responsivity change. At the starting and ending points of a scan, *IRAS* detectors were lit up by an internal flash, which determined the responsivity of the detectors at these two points. In the early calibration schemes, a linear interpolation of the responsivity was done between the two points, and assumed to represent the responsivity change, which is clearly discrepant from the actual effect when the scan passes through bright regions like the Galactic plane (Figure 3.9(a)). Figure 3.9(b) shows the deviation of quoted fluxes from true values, and 3.9(c) shows the variation of the flux ratio of fluxes obtained on descending and ascending scans.

To quantify the residual hysteresis effect of the ISSA images (which were used as large scale surface brightness truth table for the IGA), ISSA images made from HCON 1 and 3 were compared at $l = 0^\circ, 10^\circ, 20^\circ, 60^\circ, 120^\circ, 180^\circ, 240^\circ, 300^\circ, 340^\circ$, and 350°. Images covering $\pm 5^\circ$ latitude and $\pm 2.5^\circ$ longitude were first smoothed with a $4.5'$ boxcar kernel, roughly the ISSA resolution, and then summed over 5° longitude intervals to increase signal to noise. Pixel intensity ratios (HCON 1/HCON 3) were computed then averaged over each 5° $(l) \times 4.5'$ (b) box.

Figures 3.10 and 3.11 plot the average intensity (left column) and HCON 1/HCON 3 ratio (right column) versus Galactic latitude. Plots made versus Galactic latitude are sufficient for our purpose, although strictly speaking ecliptic latitude better represents the *IRAS* scanning direction. [4] The hysteresis signature is seen clearly near $l = 0^\circ$ with an amplitude of about 20% at 100 μm. As expected, the peak of the average intensity plot corresponds to the appearance of the hysteresis signature in the ratio plot. Hysteresis may also be present in the $l = 60^\circ$ and 300° graphs but below the 5% level. Other small ($<$ 5%) but systematic variations in the ISSA ratio are likely due to destriping differences. Figure 3.12 shows the maximum and minimum HCON 1/HCON 3 ratio found at each

---

[3] Most (96%) of the sky was covered by at least two HCONs, and 2/3 of the sky was covered by a third HCON.

[4] As the *IRAS* scan lines follow approximately lines of constant ecliptic longitude, it may appear that the ecliptic coordinate system should be used for the hysteresis analysis. However, the regions of interest are in the Galactic plane, and using the Galactic system emphasizes the effect due to brightness changes along the Galactic latitude.

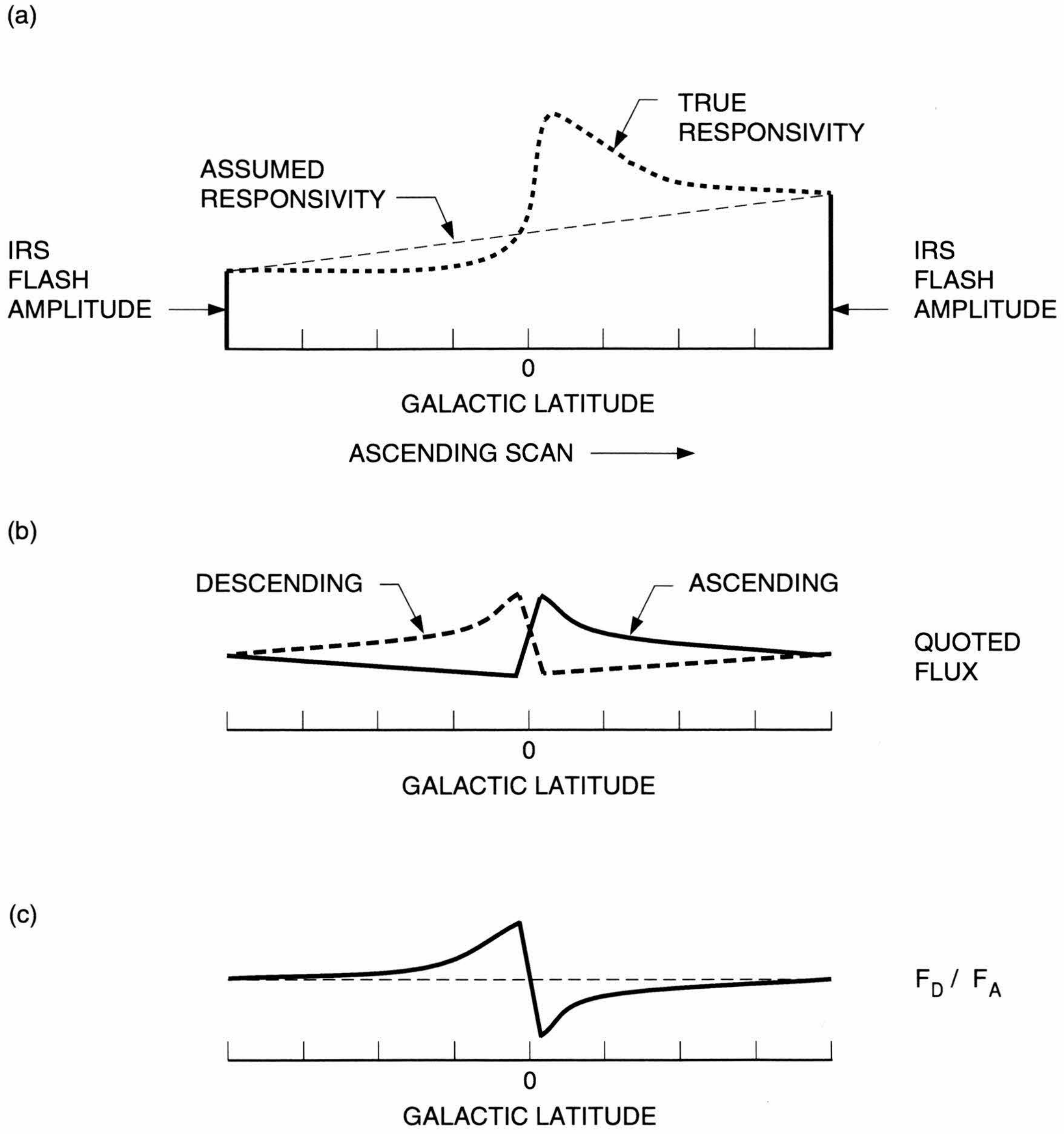

Figure 3.9: Illustrations of the hysteresis effect. (a). Internal flashes of known magnitude were used at the starting and ending points of a scanline, in an effort to determine the responsivity change (dashed line, assumed responsivity). The true responsivity is shown in the dashed curve, due to photon induced responsivity enhancement; (b). Quoted fluxes from ascending and descending scans deviate from the true values; (c). The ratio of quoted fluxes varies with Galactic latitude. (Adapted with changes from Figure VI.B.2, *IRAS* Catalogs and Atlases: Explanatory Supplement 1988.)

longitude. At 100 μm and within 60° of the Galactic center, residual hysteresis becomes larger than systematic differences due to destriping and noise.

3.6 Artifacts

For general descriptions on artifacts produced by HIRES processing, see `http://www.ipac.caltech.edu/ipac/iras/hires_artifacts.html`.

3.6.1 Striping Artifacts

Stripes were formerly the most prominent artifacts in HIRES images. HIRES takes as input the *IRAS* detector data, and if not perfectly calibrated, would try to fit the gain differences in the detectors by a striped image. The striping builds up in amplitude and sharpness along with the HIRES iterations, as the algorithm refines the "resolution" of the stripes.

An algorithm was developed (Section 2.3) to eliminate the striping artifacts. The basic technique involved is to estimate gain variations in the detectors and compensate for them within the image reconstruction process. Observation of the Fourier power spectrum of resulting images shows that the algorithm eliminates striping signal after roughly ten iterations. Therefore, striping artifacts have been virtually eliminated from the IGA images.

3.6.2 Ringing Artifacts

"Ringing" is a prominent artifact in the IGA images. When there is a point source superimposed on a non-zero background, the artifact known as *ringing* or ripples appears in many image reconstruction algorithms. For a detailed discussion of the ringing artifact and suppression algorithms, see Section 2.4.

The magnitude of the ringing depends on the strength of the point source, the level of residual background intensity (after the application of flux bias), and the detector scan pattern. For nonlinear algorithms (such as MCM) the dependence is complicated and difficult to quantify.

The ringing artifact adds uncertainty to the level of background emission around point sources, thus hinders the increase of photometric accuracy with smaller aperture (see Section 3.5.2). The ringing may also interfere with the lower intensity structures present in

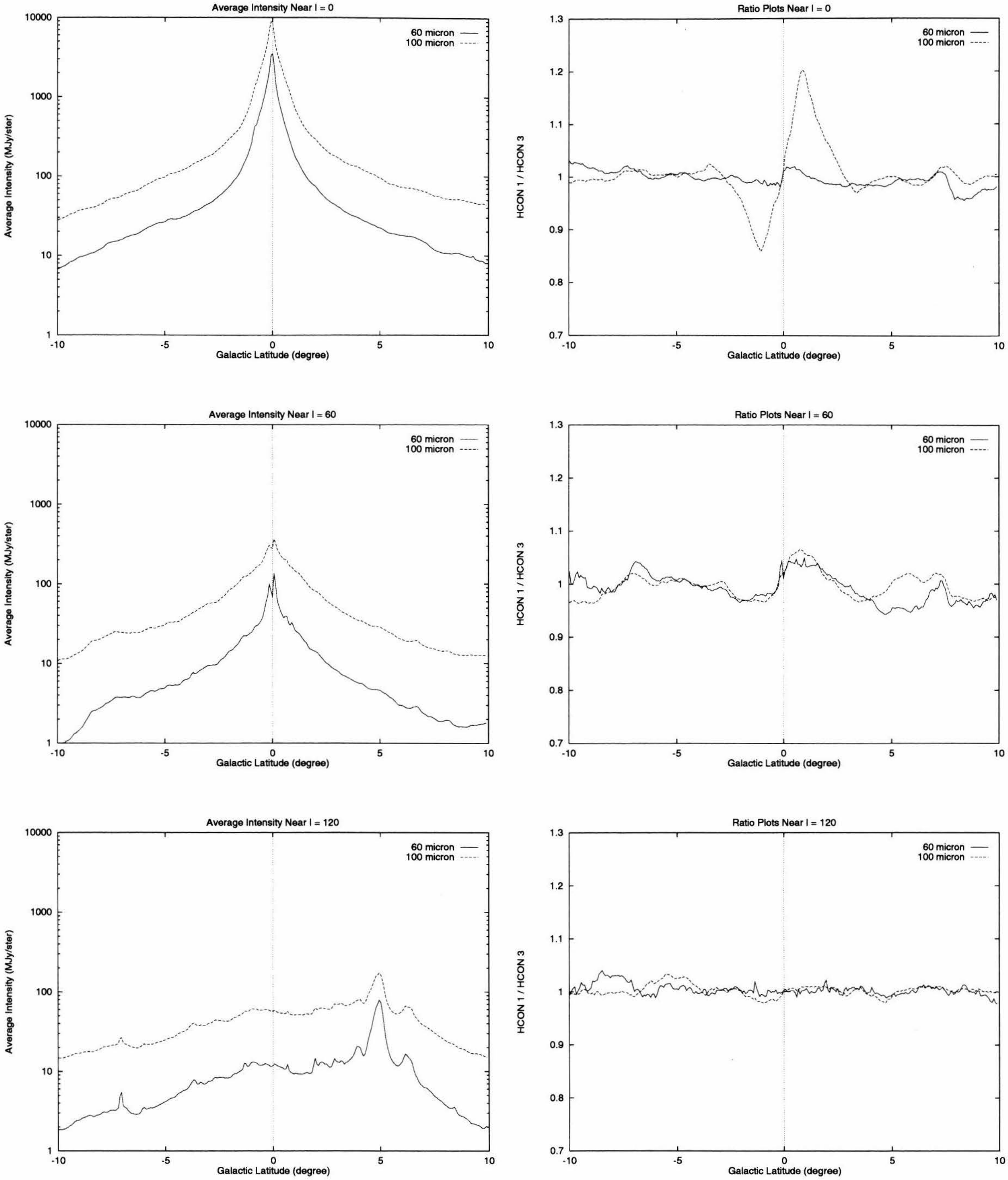

Figure 3.10: Average intensity and ratio of ISSA intensities from opposite scans, $l = 0°$, $60°$, and $120°$. The hysteresis signature is seen clearly near $l = 0°$ with an amplitude about 20% at 100 μm. Hysteresis may also be present in the $l = 60°$ and $300°$ graphs but below the 5% level. Other small (< 5%) but systematic variations in the ISSA ratio are likely due to destriping differences.

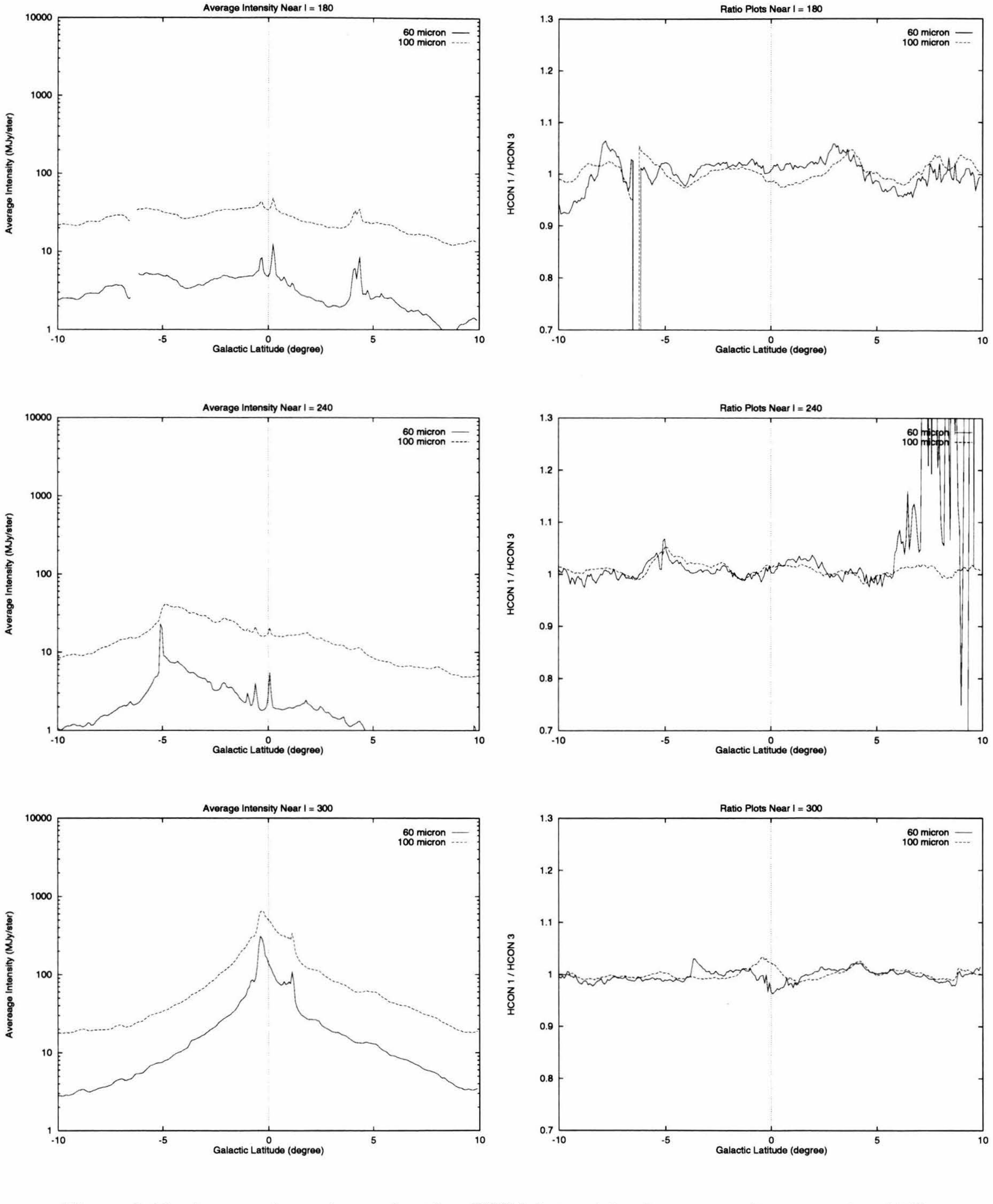

Figure 3.11: Average intensity and ratio of ISSA intensities from opposite scans, $l = 180°$, $240°$, and $300°$.

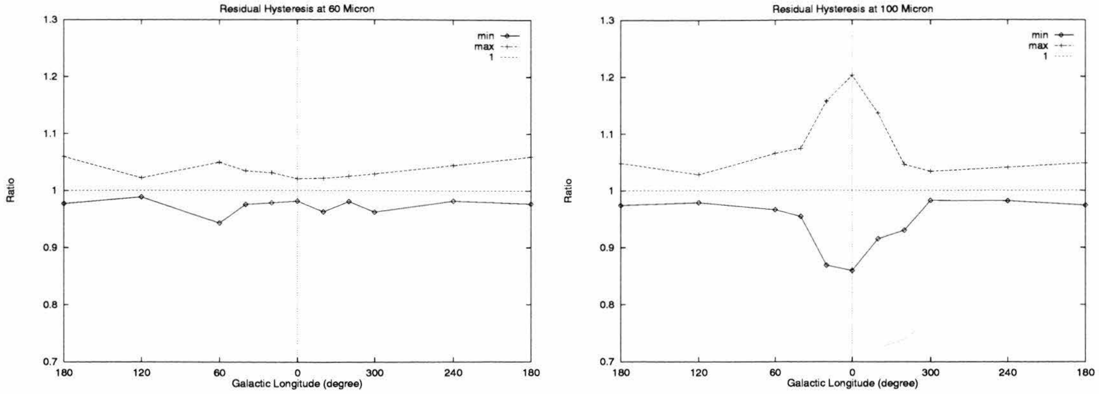

Figure 3.12: Minimum and maximum intensity ratios vs. Galactic longitude. Left: 60 μm; Right: 100 μm. At 100 μm and within 60° of the Galactic center, residual hysteresis becomes larger than systematic differences due to destriping and noise.

the background.

The cross log entropy maximization algorithm (Section 2.4.2) which gave satisfactory ringing suppression results for many test fields was developed after the IGA image production had started; therefore, the IGA used the standard MCM algorithm, which is known to give good photometry and has gone through rigorous testing. This left point source ringing as the only type of persisting major artifacts in the IGA images.

Figure 3.13 demonstrates the ringing around several point sources. At the 1st iteration, the point sources are poorly resolved and no ringing is seen. At the 20th iteration, low intensity rings (the shape of which is roughly elliptical and determined primarily by the detector response functions) surround the point sources. Further away from the point source, a brighter ring is usually visible.

3.6.3 Glitches

Glitches are caused by hits on individual detectors by cosmic rays or trapped energetic particles. The IPAC utility LAUNDR passes the flux values in each scan line through two filters, one detecting point sources and one glitches. If the ratio of the power in the point source filter to that in the glitch filter is greater than a certain threshold (default is 1), the phenomenon is taken to be a point source, otherwise a glitch.

In a few regions found by visual inspection, glitches were mistaken as point sources and leaked into the image reconstruction stage. In such cases reprocessing with a higher point source to glitch power threshold in LAUNDR sufficed to eliminate the artifact. How-

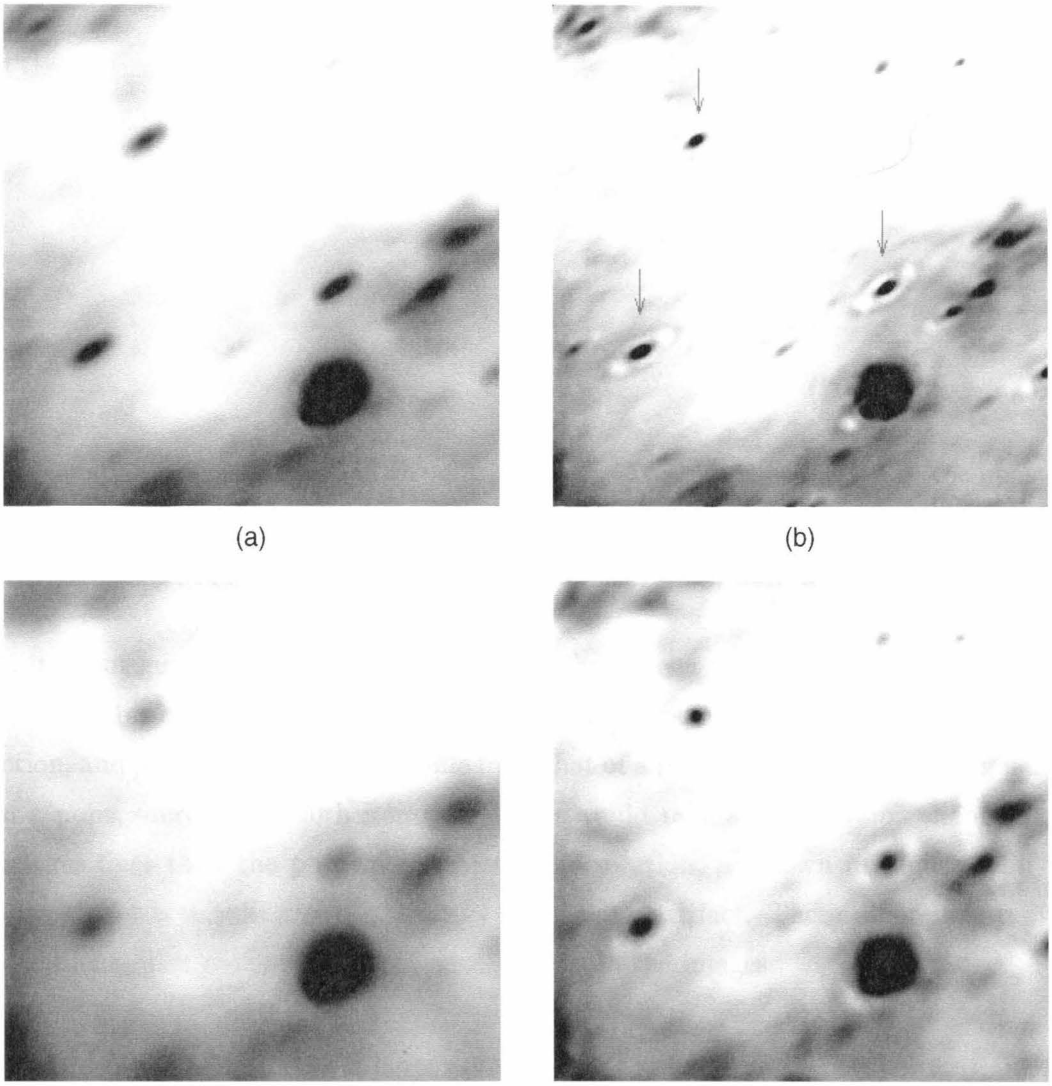

(a)

(b)

(c)

(d)

Figure 3.13: Demonstration of the ringing artifact. (a). 1st iteration, 60 μm; (b). 20th iteration, 60 μm; (c). 1st iteration, 100 μm; (d). 20th iteration, 100 micron. Ringing is not seen for the 1st iteration images, but are prominent in the 20th. Field center is at $l = 75°, b = 1°$; field size is 1.4° on each side. Black is brighter in the images.

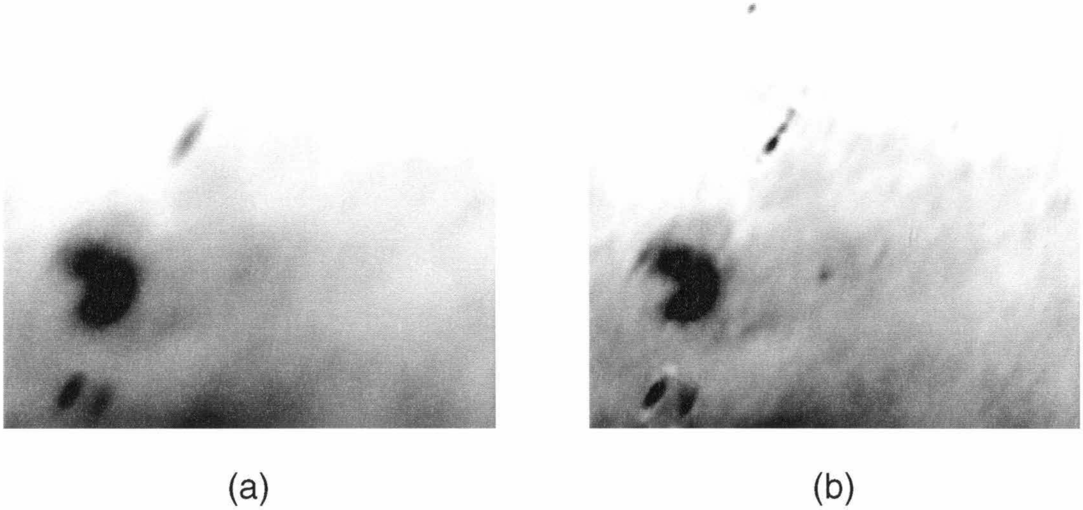

Figure 3.14: Demonstration of the glitch artifact. The elongated feature to the upper-left of the field center is a glitch. (a) and (b) show the glitch at 1st and 20th iteration respectively. At 20th iteration, the glitch takes a "broken-up" shape. Black is brighter in the images. Field center is $l = 7°, b = 1°$; field size is 1.4° on each side.

ever, it is not guaranteed that all such artifacts have been uncovered.

In 1st iteration images, a glitch traces out the shape of a single detector response function, and possesses a different profile from that of a point source (a glitch being narrower than a point source). At 20th iteration, glitch would take a "broken-up" shape, showing structures finer than the physically achievable resolution, as shown in Figure 3.14, while a point source is usually characterized by the ringing artifact. These differences provide a way to distinguish real point sources and glitches in the images.

3.6.4 Discontinuities

The ISSA images employed both global and local destriping techniques, and the local destriping left some amount of intensity discrepancy in adjacent ISSA plates (*IRAS* Sky Survey Atlas Explanatory Supplement 1994).

When reprojecting and mosaicking the ISSA images to the Level 1 geometry (against which the detector data are calibrated and zodiacal emission removed), care was taken to adjust the cropping of neighboring ISSA plates to minimize the discontinuity. In a small number of cases, however, some discontinuity remained which eventually affected

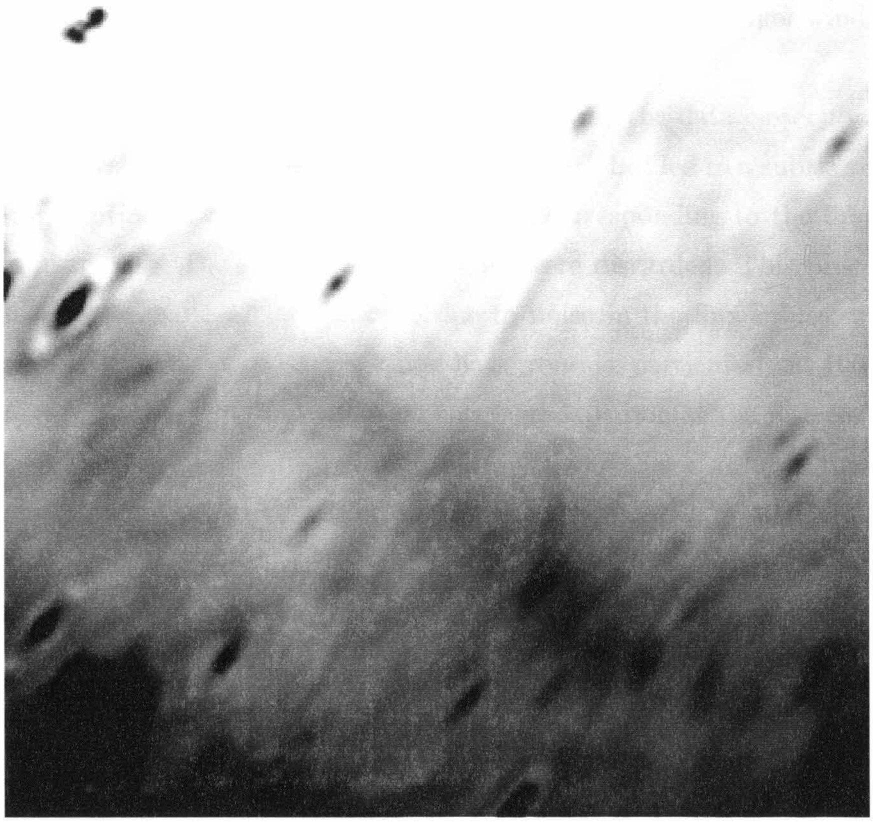

Figure 3.15: Discontinuity across one subfield. 60 μm, 20th iteration, field is centered at $l = 48°, b = 1°$, 1.4° on each side. The difference in intensity is approximately 5 MJy sr^{-1}.

the final IGA image. The discontinuity is not seen in the 1st iterations, but is sharpened and visible in the 20th. Less than 0.5% of all the 1.4° × 1.4° subfields are affected by this artifact. Figure 3.15 shows one instance of the discontinuity across a subfield (60 μm, 20th iteration). The difference in intensity is approximately 5 MJy sr^{-1}.

The different flux bias values used in different 1.4° × 1.4° fields also affect the mosaicking property of nearby images, since different resolutions are achieved in the overlap region from the two images. See Section 3.5.7 for a detailed discussion.

3.6.5 Coverage Artifacts

After the processing of the mini-survey ($-1.7° < b < 1.7°$), it was found the data processing window was too small, causing coverage depletion, and therefore unreliable structure near window boundaries. A border of at least 5′ should be cropped from images within the mini-survey. For the extended survey (1.3°$< |b| <$ 4.7°), a larger window (1.67° × 1.67°) was used in BrkDet to avoid coverage depletion.

The use of a flux bias (see Section 3.3.4), to bring the data closer to zero during processing, and thereby increase throughput, was necessary but led to a subtle artifact. The IGA processing subtracted a flux bias from the data corresponding to the first percentile from the flux histogram. Data below the threshold were discarded. This procedure effectively assumes the lower 1% of the data are due to noise in the flux values, which is not always justified. In fields which had structured backgrounds, particularly at 100 μm, it was found that discarding data resulted in severe coverage depletion at the intensity minimum of an image. All images where the coverage fell below a value of 5 in the coverage map were reprocessed with a smaller flux bias. However problems, such as anomalous structure near the image intensity minimum, may remain. The ancillary CVG map can help diagnose problems associated with inadequate coverage.

3.7 Example Images

To illustrate the image quality of the *IRAS* Galaxy Atlas, mosaics at 60 μm of a restricted latitude range ($-1.7° < b < 1.7°$) were made for regions between Galactic longitude 280° and 80° (approximately 16% of the total area covered by the atlas), and are shown in Figures 3.16, 3.17, 3.18, and 3.19. Most of the emission is from stellar heated dust and shows a wealth of star-forming regions, H II regions, and diffuse infrared cirrus (e.g., Fich & Terebey 1996). Extended Galactic infrared emission, long associated with the Galactic H I layer, is readily apparent as enhanced emission near the midplane (e.g. Terebey & Fich 1986; Sodroski et al. 1989). Each panel covers 11° in longitude. The dynamic range is much larger than can be displayed, therefore the stretch is logarithmic, with the range chosen separately for each panel to emphasize the most structure.

The complete set of available images and ancillary maps is illustrated for an individual 1.4° × 1.4° field near IC-1805 in the second Galactic quadrant. Figure 3.20 shows the co-added and resolution enhanced images plus beam sample maps. Figure 3.21 shows the associated diagnostic ancillary maps (see Section 3.2). The source IC-1805, an OB cluster exhibiting strong winds and ionizing radiation, is located near the brightest far-infrared emission. To the north, a cloud suffering erosion from the IC-1805 cluster appears in the

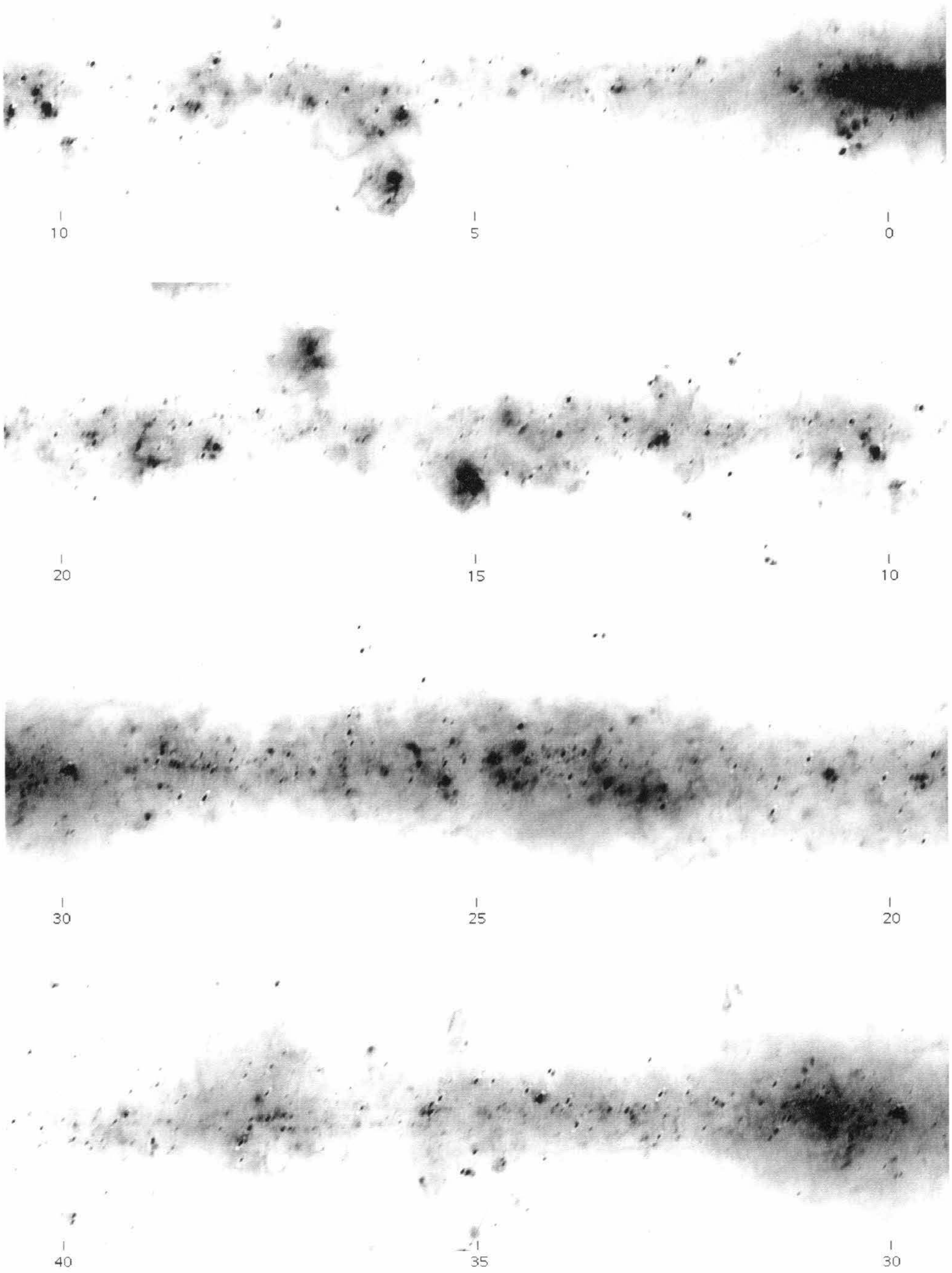

Figure 3.16: *IRAS* Galaxy Atlas images of the Galactic plane at 60 μm, Longitude 0° – 40° show a variety of star-forming regions, H II regions, and the diffuse infrared emission associated with the Galactic H I layer. Each panel covers 11° in longitude and $-1.7°$ $< b < 1.7°$ in latitude, with logarithmic stretch chosen to emphasize structure.

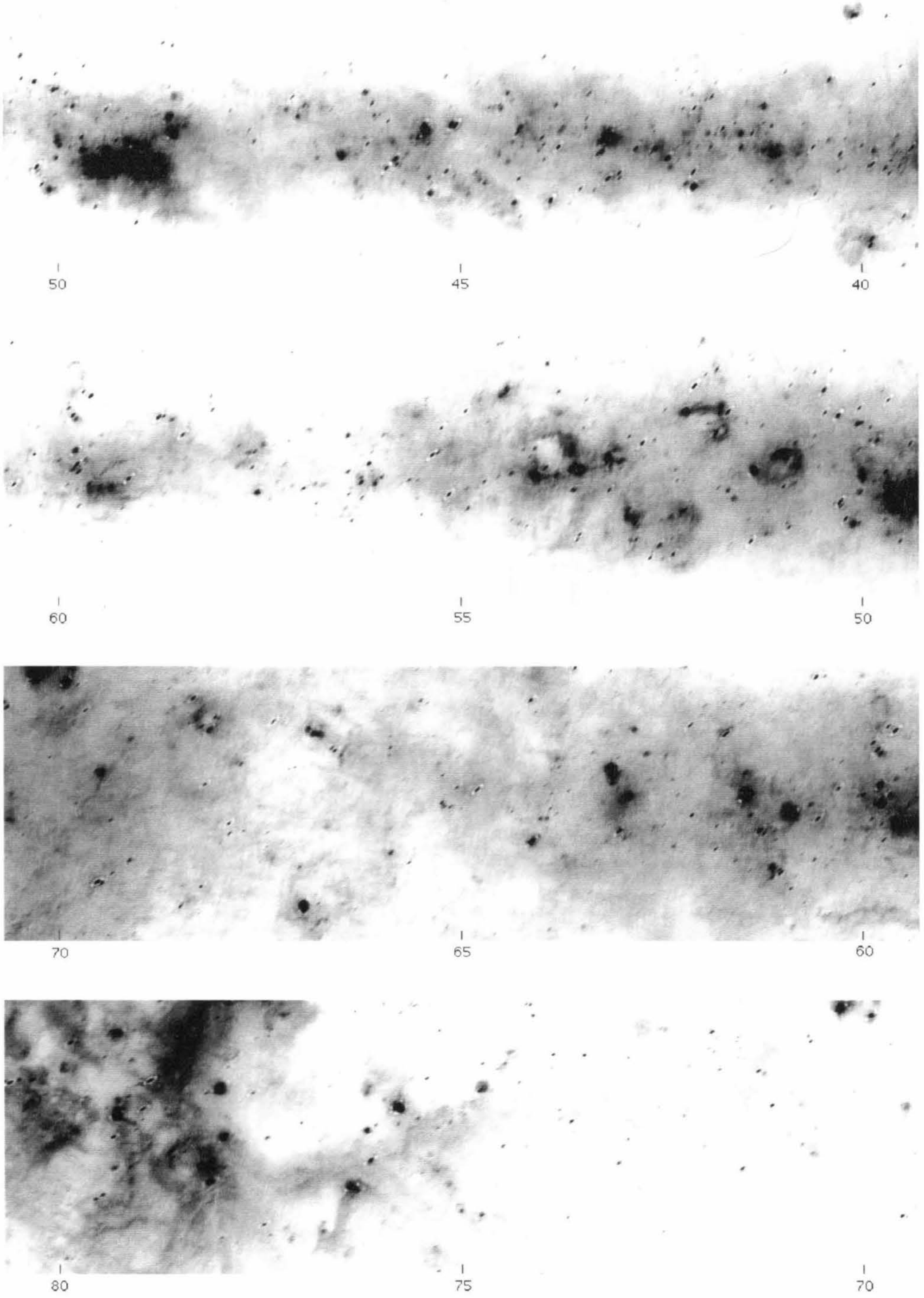

Figure 3.17: The Galactic plane at 60 μm, longitude 40° - 80°.

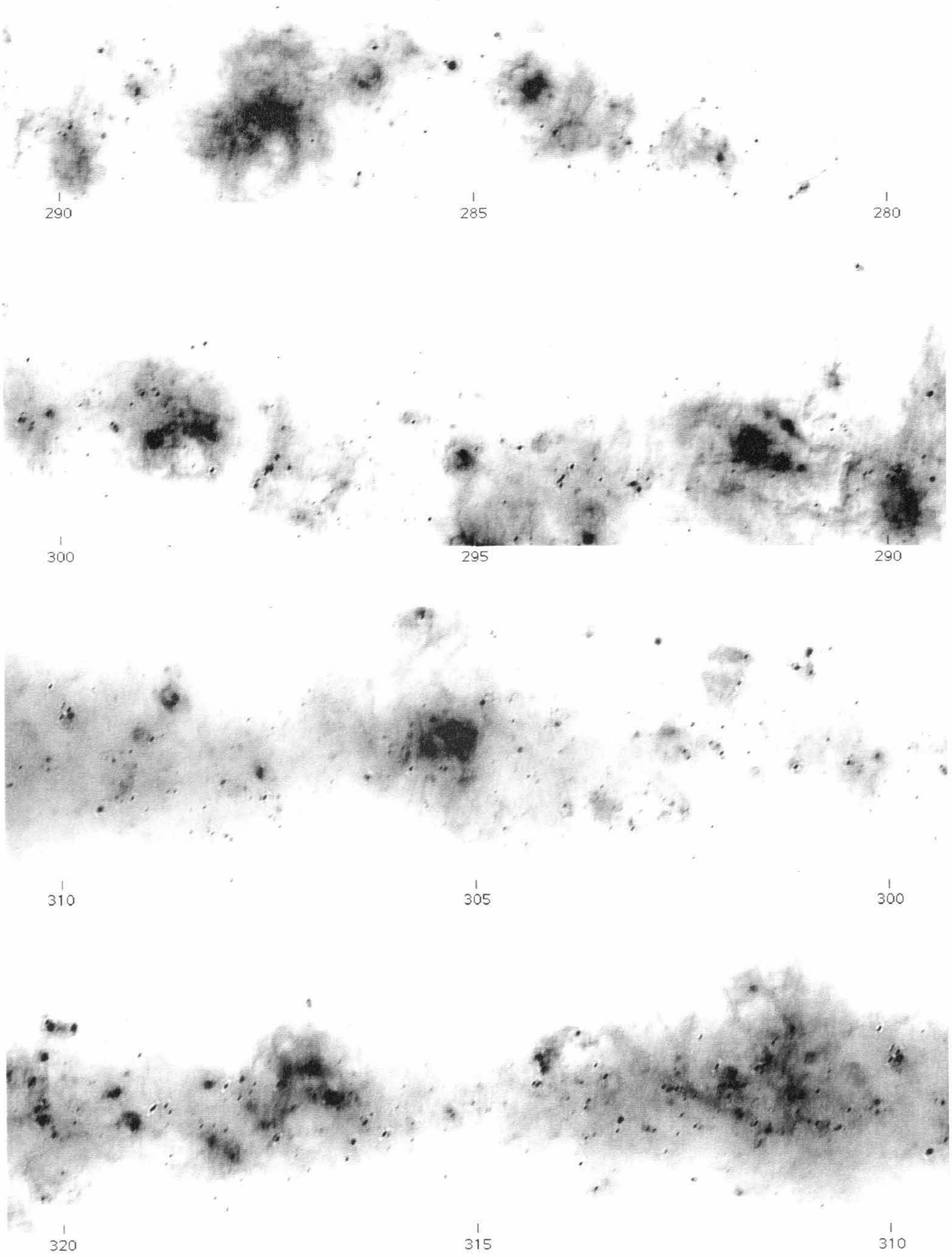

Figure 3.18: The Galactic plane at 60 μm, longitude 280° – 320°.

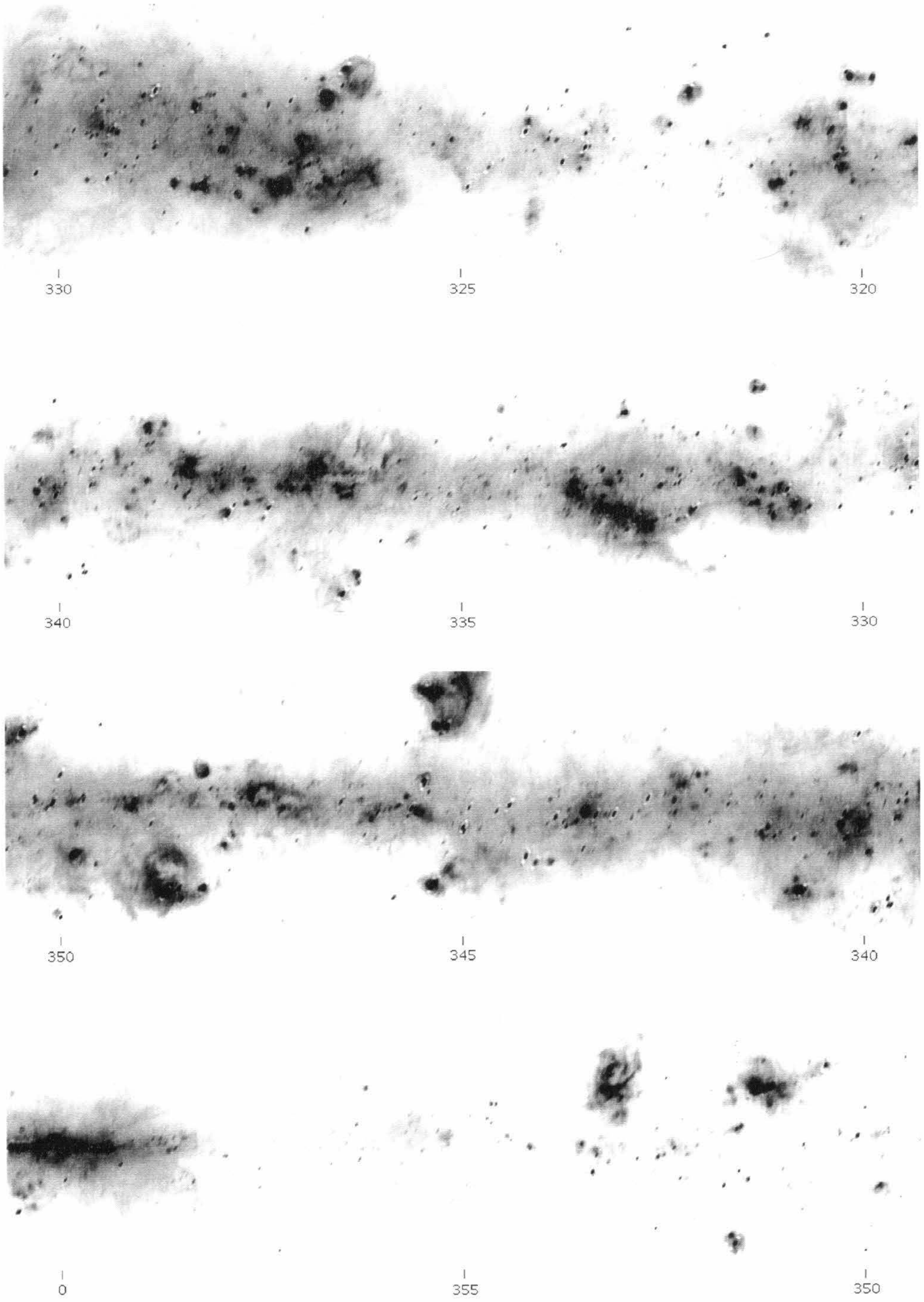

Figure 3.19: The Galactic plane at 60 μm, longitude 320° – 0°.

infrared as a cometary shaped arc (Heyer et al. 1996). An H I survey of the region shows that the OB cluster appears to fuel a Galactic chimney (Normandeau, Taylor, & Dewdney 1996).

3.8 Summary

The *IRAS* Galaxy Atlas, an atlas of the Galactic plane ($-4.7^\circ < b < 4.7^\circ$) plus the molecular clouds in Orion, ρ Ophiuchi, and Taurus-Auriga has been produced at 60 and 100 μm from *IRAS* data. The HIRES processor, which incorporates the MCM resolution enhancement algorithm, was ported to the Caltech parallel supercomputers for the CPU intensive task.

At 60 μm the typical resolution is $2.0' \times 4.7'$ for co-added IGA(1) (iteration = 1) images, and $1.0' \times 1.7'$ for resolution enhanced IGA(20) images, which compares favorably with the $50''$ diffraction limit of the *IRAS* telescope and the $5'$ resolution of the previously released *IRAS* Sky Survey Atlas (ISSA). At 100 μm, where the diffraction limit is $84''$, the typical IGA(1) resolution is $3.8' \times 5.4'$ and IGA(20) resolution is $1.7' \times 2.2'$, again compared with the $5'$ ISSA resolution.

The *IRAS* Galaxy Atlas contains images, beam sample maps to assess local resolution, and ancillary diagnostic maps in FITS format. Field sizes are $1.4^\circ \times 1.4^\circ$ in the Galactic plane, and $2.5^\circ \times 2.5^\circ$ in the Orion, ρ Ophiuchi, and Taurus-Auriga molecular clouds.

Zodiacal emission has been removed from the images. The result is images which are easily mosaicked by simple cropping and contain negligible seams. Stripes in the images, long the limiting artifact of standard HIRES processing, have been eliminated by algorithmic improvements to the destriping procedure. "Ringing" around point sources is the major artifact remaining in the IGA images.

Photometry on the IGA images is accurate to roughly 25%, depending on the wavelength and size scale, while positions agree with the *IRAS* Point Source Catalog to better than $8''$ standard deviation.

The *IRAS* Galaxy Atlas, combined with other Galactic plane surveys of similar ($\sim 1'$) resolution, provides a powerful venue for multi-wavelength studies of the interstellar medium, star formation and large scale structure in our Galaxy.

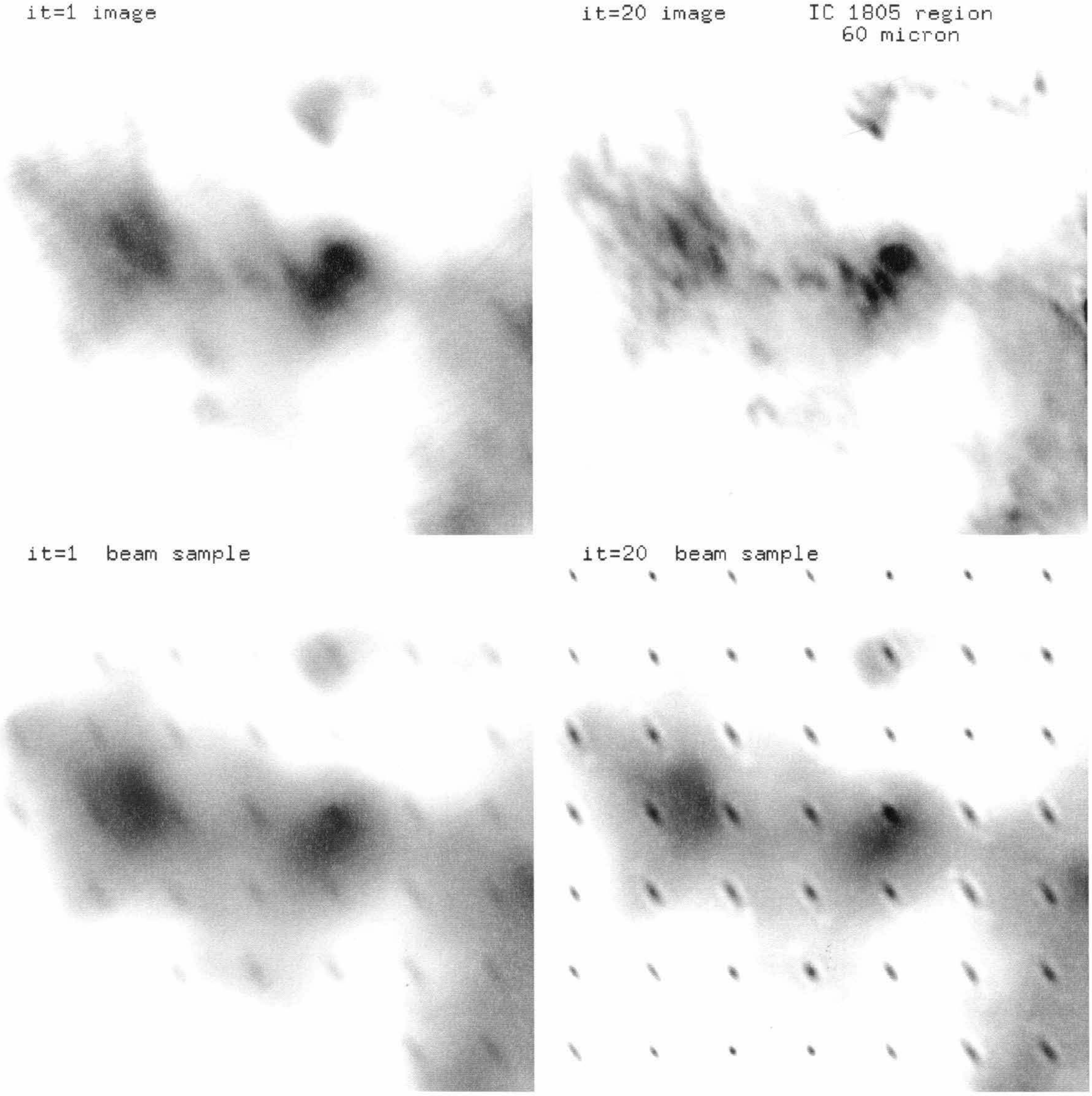

Figure 3.20: Image (IMG) and beam sample maps (BEM) for the IC-1805 OB cluster, 60 μm.

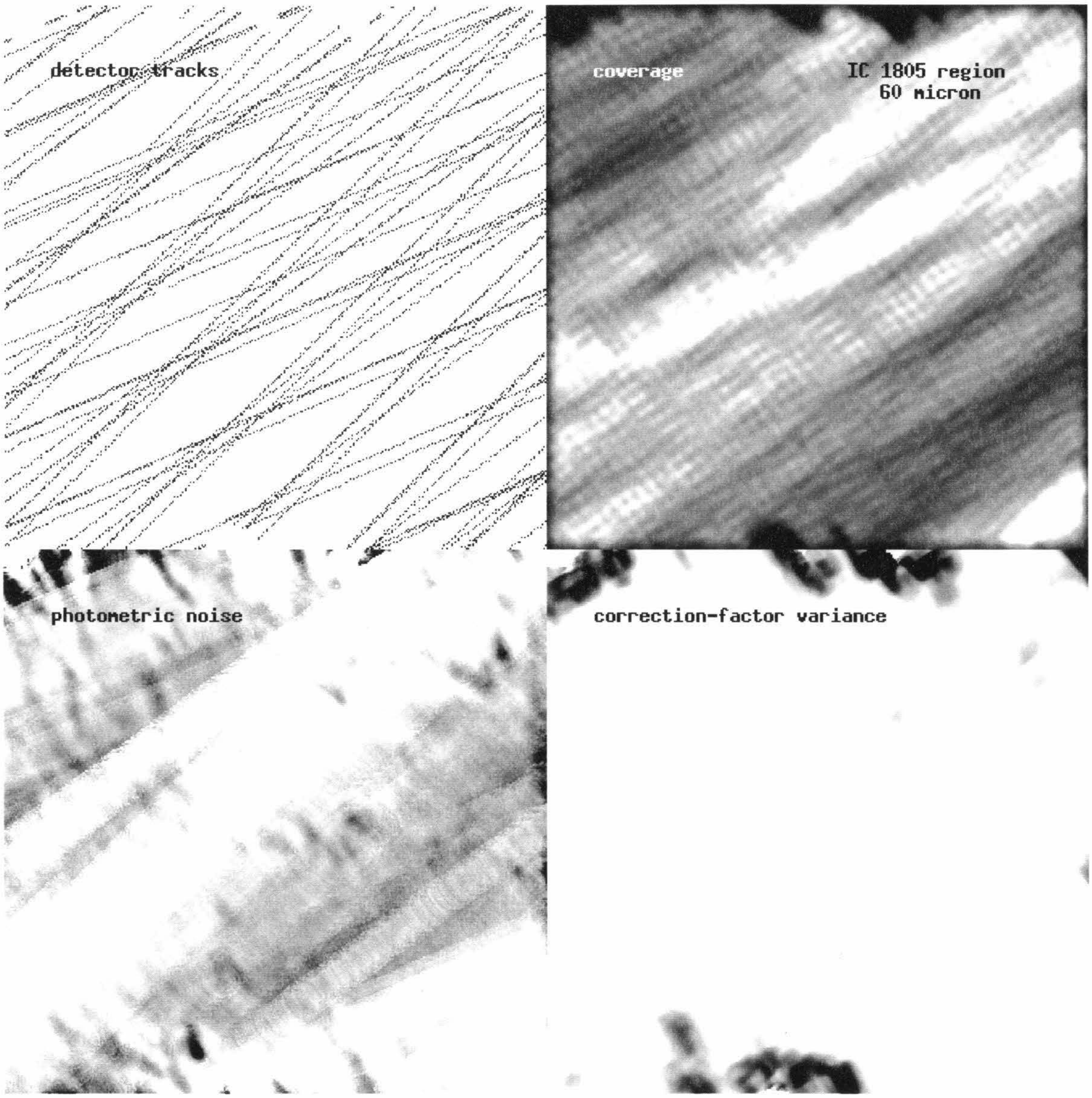

Figure 3.21: Detector track (DET), coverage (CVG), photometric noise (PHN), and correction-factor variance (CFV) maps for IC-1805, 60 μm.

References

Assendorp, R., Bontekoe, T. R., Dejonge, A. R. W., Kester, D. J. M., Roelfsema, P. R., & Wesselius, P. R. 1995. The Gröningen *IRAS* imaging software (IST). *Astron. & Astrophys. Suppl.*, **110**, 395.

Aumann, H. H., Fowler, J. W., and Melnyk, M. 1990. A maximum correlation method for image construction of *IRAS* survey data. *Astron. J.*, **99**, 1674.

Beichman, C. A. 1987. The *IRAS* view of the Galaxy and the solar-system. *Ann. Rev. Astron. Astrophys.*, **25**, 521.

Beichman, C. A. 1988. The infrared universe revealed by *IRAS*. *Astrophys. L. & Comm.*, **27**, 67.

Cao, Y., Prince, T. A., Terebey, S., & Beichman, C. A. 1996. Parallelization and algorithmic enhancements of high-resolution *IRAS* image construction. *Pub. Astron. Soc. Pacific*, **108**, 535.

Cao, Y., Terebey, S., Prince, T. A., & Beichman, C. A. 1996. The high resolution *IRAS* Galaxy Atlas. *Astrophys. J. Suppl.*, submitted.

Fich, M. & Terebey, S. 1996. *IRAS* observations of the outer Galaxy. 1. discrete sources and large-scale (diffuse) emission. *Astrophys. J.*, **472**, 624.

Fowler, J. W. & Aumann, H. H. 1994. HIRES and beyond. In *Science with High Spatial Resolution Far-Infrared Data,* ed. S. Terebey & J. Mazzarella (Pasadena: JPL 94-5), 1.

Good, J. 1994. Zodiacal dust cloud modeling using *IRAS* data. In *IRAS Sky Survey Atlas Explanatory Supplement*, ed. S. L. Wheelock et al. (Pasadena: JPL 94-11), G-1.

Green, R. M. 1985. *Spherical Astronomy* (Cambridge: Cambridge U. Press).

Greisen, E. W. & Calabretta, M. 1996. *Astron. & Astrophys.*, submitted.

Heyer, M. H., Carpenter, J., Snell, R. L., & Schloerb, F. P. 1994. FCRAO CO Survey of the Second Quadrant. *Bull. Amer. Astron. Soc.*, **184**, 27.05.

Heyer, M. H., Brunt, C., Snell, R. L., Howe, J., Shloerb, F. P., Carpenter, J. M., Normandeau, M., Taylor, A. R., Dewdney, P. E., Cao, Y., Terebey, S., & Beichman, C. A. 1996. A massive cometary cloud associated with IC-1805. *Astrophys. J.*, **464**, L175.

IRAS Catalogs and Atlases: Explanatory Supplement 1988. Beichman, C. A., Neugebauer, G., Habing, H. J., Clegg, P. E., and Chester, T. J. (eds.) (Washington, DC: GPO).

IRAS Point Source Catalog, Version 2, 1988. Joint *IRAS* Science Working Group (Washington, DC: GPO).

IRAS Sky Survey Atlas Explanatory Supplement, 1994. Wheelock, S. L., Gautier, T. N., Chillemi, J., Kester, D., McCallon, H., Oken, C., White, J., Gregorich, D., Boulanger, F., Good, J. and Chester, T. (Pasadena: JPL 94-11).

Kessler, M. F. 1995. The *Infrared Space Observatory (ISO)*. *Space Sci. Rev.*, **74**, 57.

Maccabe, B., McCurley, K. S., & Riesen, R. 1993. *SUNMOS for the Intel Paragon*, `ftp://ftp.cs.sandia.gov/pub/sunmos/doc`.

Matsumoto, T. 1995. *Infrared Telescope in Space - IRTS*. *Space Sci. Rev.*, **74**, 73.

Mill, J. D. & Guilmain, B. D. 1996. The *MSX* mission objectives. *Johns Hopkins Apl. Tech. Digest*, **17**, 19.

Normandeau, M., Taylor, A. R., & Dewdney, P. E. 1996. A Galactic chimney in the Perseus arm of the Milky Way. *Nature*, **380**, 687.

Normandeau, M., Taylor, A. R., & Dewdney, P. E. 1997. The Dominion Radio Astrophysical Observatory Galactic plane survey pilot project: the W3/4/5/HB3 region. *Astrophys. J. Suppl.*, **108**, 279.

Price, S. D. 1995. Infrared astronomy on the *Midcourse Space Experiment*. *Space Sci. Rev.*, **74**, 81.

Rice, W. 1993. An atlas of high-resolution *IRAS* maps of nearby galaxies. *Astron. J.*, **105**, 67.

Sodroski, T. J., Dwek, E., Hauser, M. G., & Kerr, F. J. 1989. Large-scale Galactic dust morphology and physical conditions from *IRAS* observations. *Astrophys. J.*, **336**, 762.

Soifer, B. T., Houck, J. R., & Neugebauer, G. 1987. The *IRAS* view of the extragalactic sky. *Ann. Rev. Astron. Astrophys.*, **25**, 187.

Wells, D. C., Greisen, E. W. and Harten, R. H. 1981. FITS — a flexible image transport system. *Astron. & Astrophys. Suppl.*, **44**, 363.

Chapter 4

Analysis Example: W3-5

4.1 Introduction

The *IRAS* Galaxy Atlas, in conjunction with the DRAO [1] H I line/21 cm continuum (Normandeau, Taylor, & Dewdney 1996; Normandeau, Taylor, & Dewdney 1997) and FCRAO [2] CO J=1–0 line (Heyer et al. 1994) Galactic plane surveys, both with similar ($\sim 1'$) resolution, provide a powerful venue for studying the interstellar medium and large scale structure in our Galaxy.

The University of Calgary Radio Astronomy Laboratory is imaging the H I distribution of our Galaxy using the DRAO synthesis telescope. Previous surveys of Galactic H I have employed single dish radio telescopes, giving resolution of $10'$ or poorer, and most were spatially undersampled. The DRAO survey would have a resolution of $1'$ and will fully sample spatial structures down to that limit. The survey is expected to be completed by 1998.

As of 1996, FCRAO is carrying out the CO survey for the second quadrant of the Galaxy. The survey will cover 320 square degrees at $50''$ sampling using the 15 element focal plane array receiver QUARRY. The survey is planned to be extended to the entire Galactic plane.

The three surveys have coordinated observations of a pilot region, an $8^\circ \times 6^\circ$ field covering the W3-5 star-forming regions in the outer Galaxy.

---

[1] Dominion Radio Astrophysical Observatory, Penticton, British Columbia. Web page can be found at `http://ftp.drao.nrc.ca/`.

[2] Five College Radio Astronomy Observatory, Amherst, Massachusetts. Web page is at `http://fcrao1.phast.umass.edu/`.

Figure 4.1 demonstrates a striking feature of the W3-5 data, namely, the exquisite correspondence of the far-infrared to the 21 cm continuum emission. The top and bottom panels of Figure 4.1 illustrate the similarity of the IGA 60 μm and DRAO 21 cm continuum fields.

4.2 Beam Matching with Cross Band Simulation

As discussed in Section 3.5.1, the 60 μm HIRES images have higher resolution (smaller beams) than the 100 μm images. For many astronomical purposes, beam matched images are desired (for example, when constructing a color ratio map between 60 and 100 μm, in which case simply computing the color ratios in each pixel by employing the two HIRES images typically yields prominent artifacts due to the incompatible resolutions).

Fowler & Aumann (1994) developed a technique, called "cross band simulation," to produce beam matched HIRES images. First, images are constructed in the two bands. Then the 60 μm image is "scanned" with the 100 μm detectors, using the same geometry and measurement locations as the real 100 μm image. The simulated data are then used to construct an image. In the same way, the real 100 μm image is used to produce simulated 60 μm detector data, which is used to construct an image. The two simulation images then have compatible resolution, and may be used to create a color ratio map or a multi-band intensity image.

Test runs were carried out for the 1.4° × 1.4° field centered at G135+0. In order to quantify the resolution achieved with cross band simulation, the BEM map (see Section 3.2) from one band was scanned and reconstructed with another band's detectors, and the resultant beam sizes were estimated through a Gaussian fit. The estimates represents the effective beam sizes achieved through two consecutive processes of scanning and reconstruction. For identical input maps (100 Jy point sources planted on smooth background), the beam comparison is summarized in Table 4.1, which lists the average ratios between beams achieved through different processing.

It can be seen from Table 4.1 that the 60_100 and 100_60 images both have beam sizes similar to that of the 100 μm image. This can be expected from the higher resolution achieved by reconstruction from 60 μm detector data (scanning and reconstructing the 100 μm image with 60 μm detector response functions would result in little resolution loss, while the resolution of the 60_100 image is determined primarily by the 100 μm processing

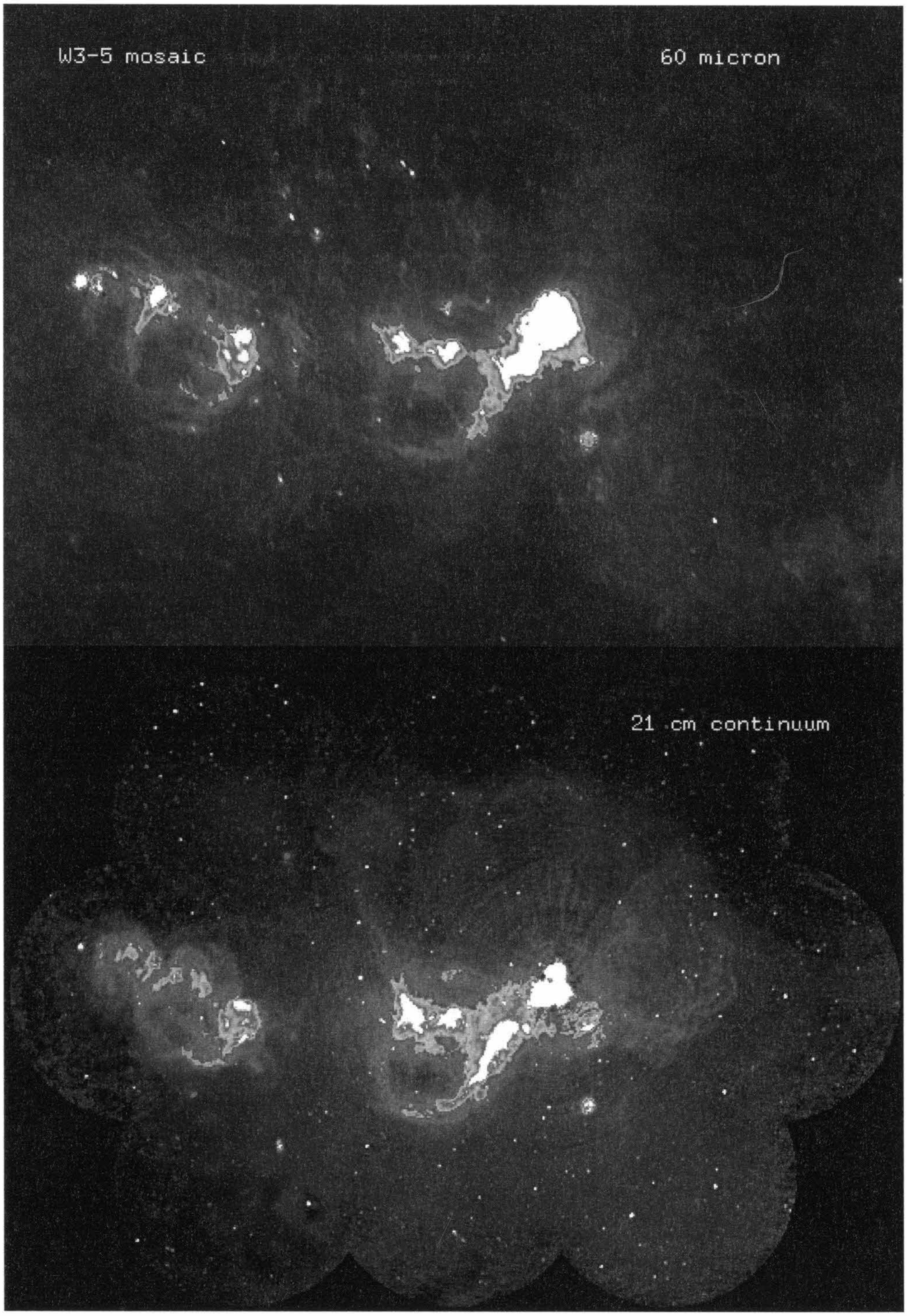

Figure 4.1: Comparison of 60 μm and 21 cm emission for W3-5. Top: W3-5 at 60 μm; bottom: 21 cm continuum (image courtesy of DRAO and the University of Calgary Radio Astronomy Laboratory). Angular scale is 8° × 6° for each panel.

Table 4.1. Beam Comparison for Cross Band Simulation

	Average Beam Ratio (maj, min) 100	100_60 [a]
over 60	1.326, 1.842	-
over 60_100	0.936, 0.967	1.012, 0.964
over 100	-	1.085, 0.996

[a] 100_60 stands for 100 μm image reconstructed from 60 μm detectors.

step).

Although the beam size analysis indicates the 60_100 and 100_60 images appear to be the best matched pair, the following considerations led to the decision of using the 60_100 and 100 images (instead of the more symmetrical 60_100 and 100_60 pair) in the W3-5 study: 1) reduced amount of processing; 2) in one test field, processing the 100 μm image with 60 μm response functions seems to have produced some amount of over-resolution and very subtle striping; 3) the beam sizes of the 60_100 and 100 pair are close enough (difference is within 7%) for our purpose.

For demonstrations of reconstructed images and beam sample maps from the cross band simulation technique, see Figure 4.2 and 4.3. It is apparent that the 100μm, 60_100, and 100_60 images all have very similar resolution.

A 10° × 7° field covering the W3-5 pilot region was processed with the cross-band simulation technique (60 μm emission reconstructed through 100 μm detectors). A two-channel color image of the field is shown in Fig 4.2. The 60 μm image is coded in green, and 100 μm in red; logarithmic stretch is used for each channel. The hotter dust (e.g., regions close to the IC-1805 OB cluster in W4) is clearly seen to have a more greenish hue, while the presumably colder halo outside the wind-swept loop appears red.

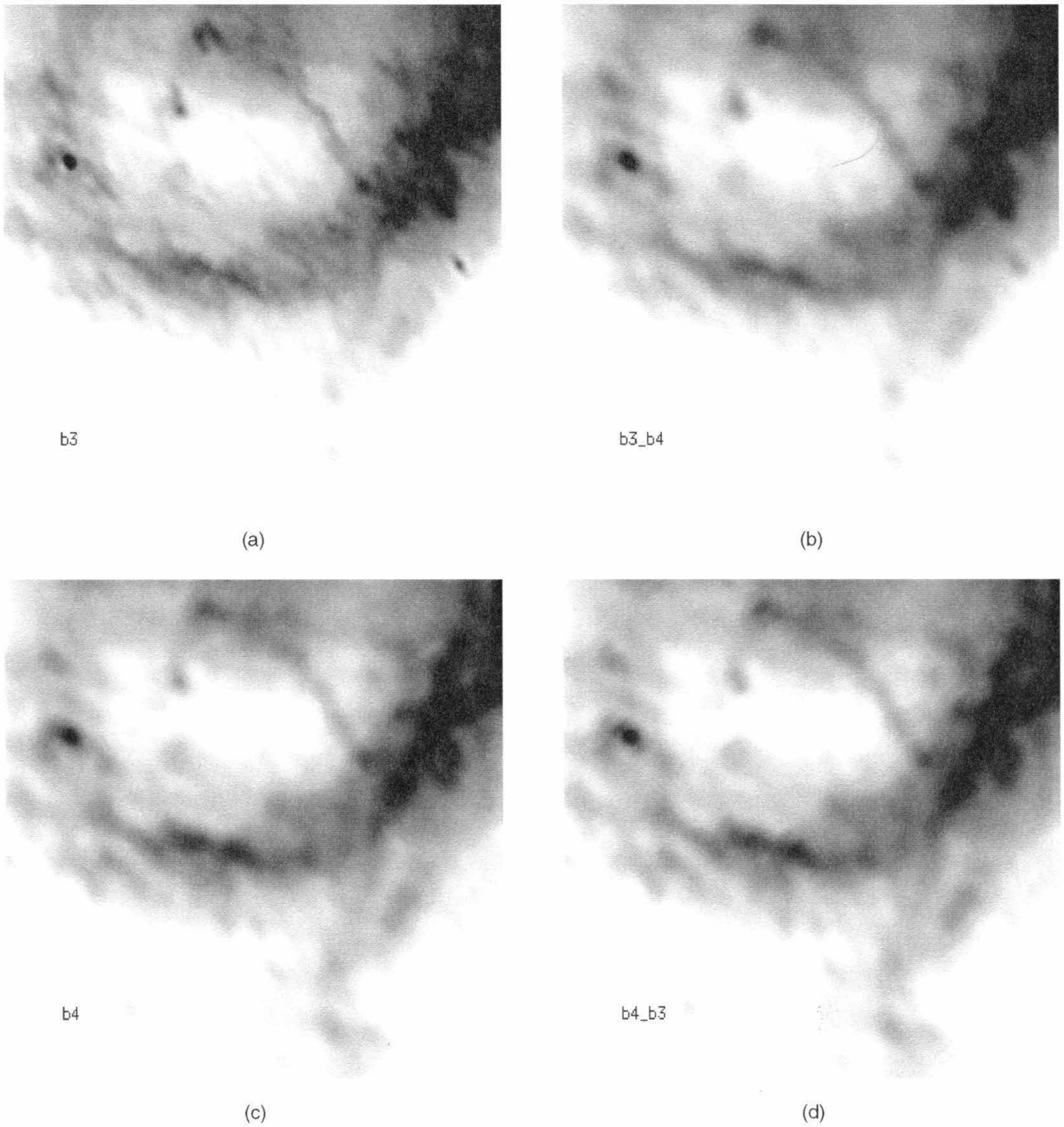

(a) (b)

(c) (d)

Figure 4.2: Comparison of HIRES and cross-band simulated images. All images are 20th iteration. The field depicts a wind-blown loop in W4. Spatial scale is 1.4° on each side; field center is at G135+0.

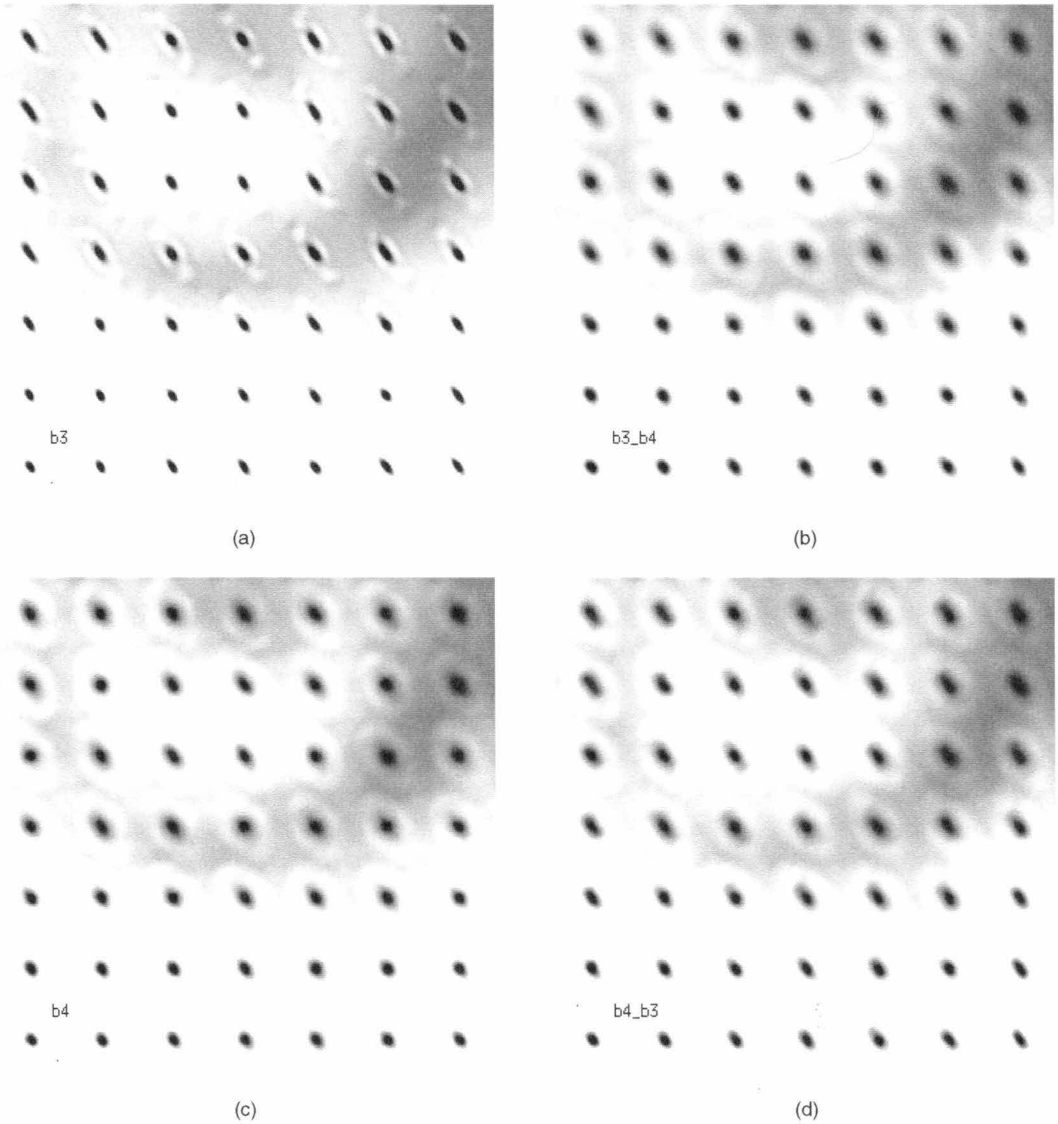

(a) (b) (c) (d)

Figure 4.3: Comparison of HIRES and cross-band simulated beam sample maps. All images are 20th iteration. Input scene is the same for each type of processing. Spatial scale is 1.4° on each side; field center is at G135+0.

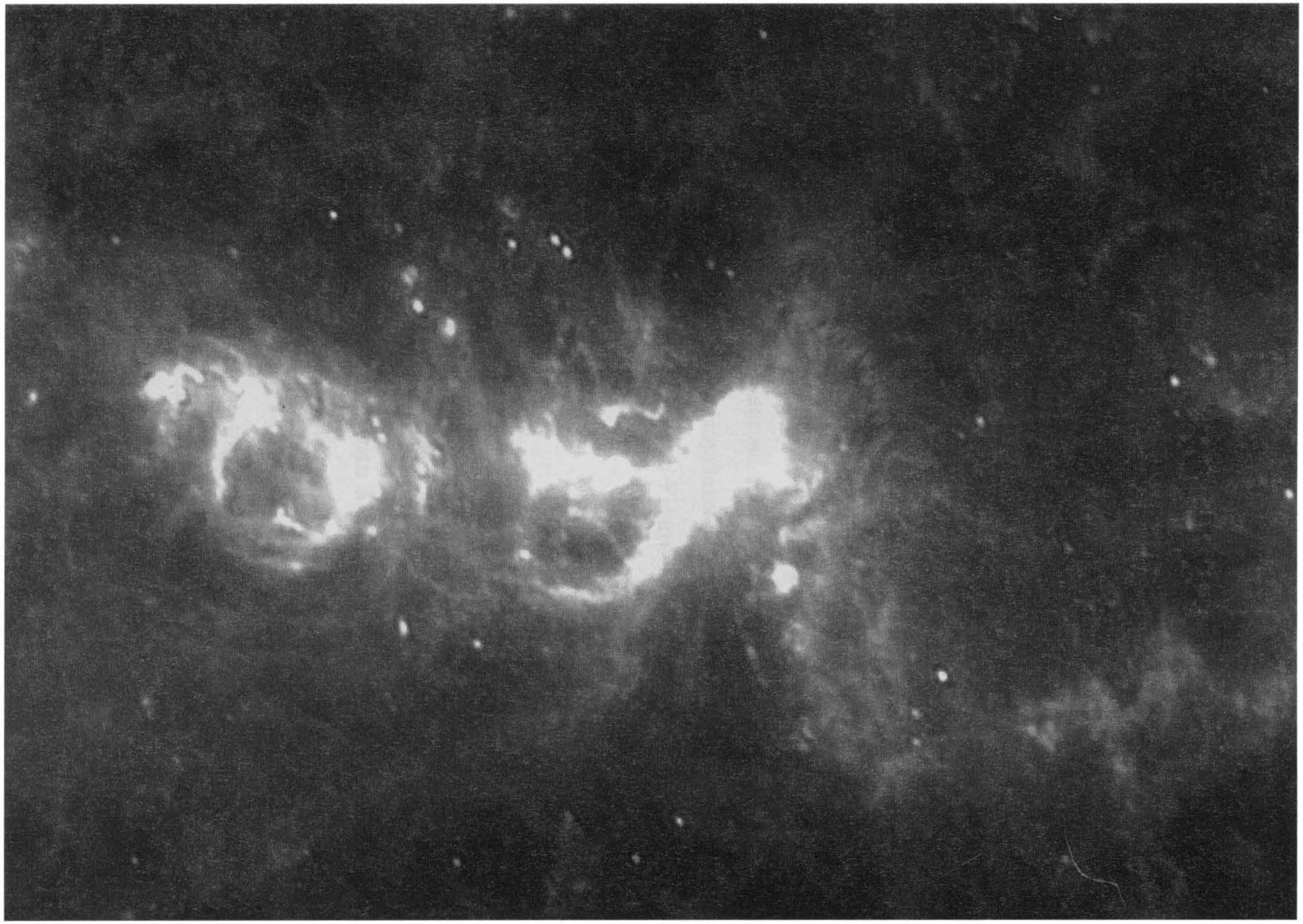

Figure 4.4: Multi-channel (60 and 100 μm) image of W3-5. 60 μm intensity is coded in green, 100 μm in red; the stretch is logarithmic in each channel. The hotter dust (e.g., regions close to the IC-1805 OB cluster in W4) is clearly seen to have a more greenish hue, while the presumably colder halo outside the wind-swept loop appears red. The red arc to the top-right of W-4 is spurious, and is probably due to imperfect hysteresis correction in the 100 μm data.

4.3 Geometrical Model of the W4 Loop

The loop in the W4 is powered by the wind from the ionizing stars in the IC-1805 OB cluster (Massey, Johnson, & DeGioia-Eastwood 1995). We built a simple geometrical model for the loop, assuming the real structure is a limb-brightened shell.

Figure 4.5 illustrates the limb-brightening effect for a spherical shell. The apparent thickness of the shell along any particular line-of-sight is larger around the edge than near the center of the shell (with the thickest region corresponding to the inner radius of the shell).

The center of the shell is taken to be at G134.9875+0.4833, and the angular radius of the shell is approximately $35'$. The distance from W4 to the Earth is 2.1 kpc, giving a shell diameter of ~ 40 pc.

We tried to fit the image intensities (slices through the radius) to the shell model, varying the radii of the inner and outer spheres, and assuming uniform density of material inside the shell. Multiple slices across the shell were made and averaged. The intensity model was smoothed with the appropriate HIRES beam (a Gaussian with $1'$ FWHM for the 60μm band. The best fit is shown in Figure 4.6, giving an inner radius of $33'$, and outer radius $40.5'$.

4.4 Discussion

Previously, Whiteoak (1994) studied the Carina nebula in radio continuum (0.843 GHz) and far inrared (also using HIRES processed *IRAS* images). The ionization front was found to form a ring-like structure with a diameter of $\sim 2'$. The IGA and DRAO 21 cm continuum images make more detailed analysis possible, given the high data quality and closer sources (2.1 kpc) in the W3-5 region. Also, the cross-band simulation technique is likely to be applied not only to provide beam matched images in the *IRAS* wavelengths (as shown in the work described here), but also extended to include images of other wavelength.

Initial investigation shows the W4 region contains a loop/halo structure. The loop is probably swept up by the strong winds from the OB cluster IC-1805. The exterior part of the loop shows enhanced far-infrared emission (compared to 21 cm), which is generally thought to be thermal emission from dust heated by ultraviolet radiation (Boulanger & Perault 1988). This seems to indicate the enhanced far-infrared emission is due to non-

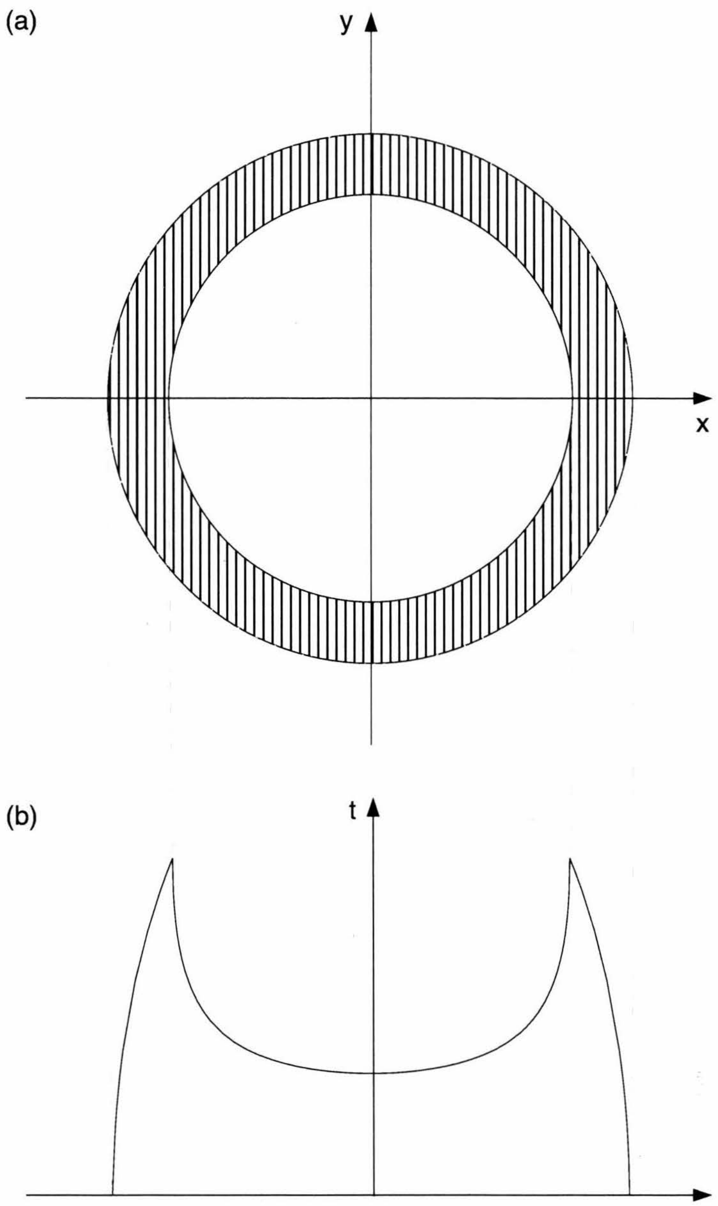

Figure 4.5: Illustrion of the limb-brightening effect for a spherical shell. Top figure (a) shows the cross section of the shell. Bottom figure (b) shows the thickness t as seen by a distant observer varying with x.

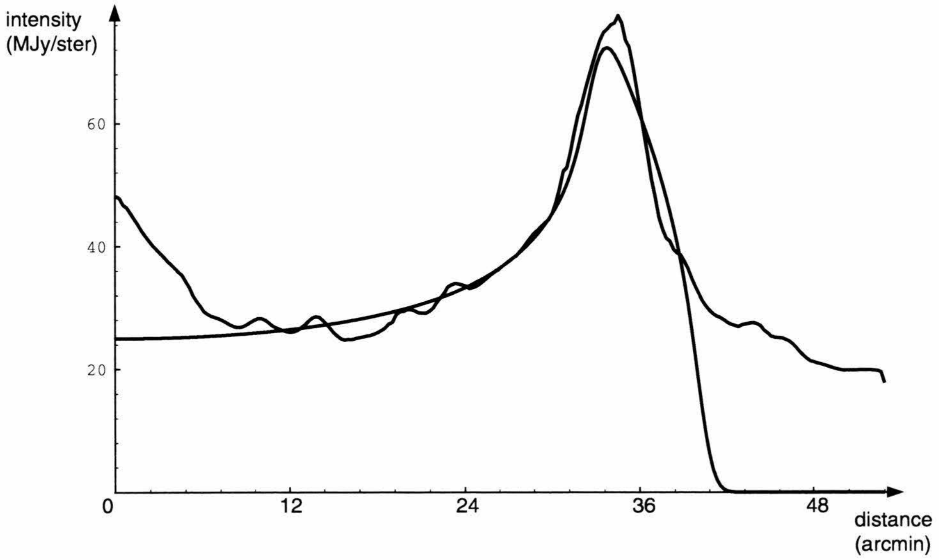

Figure 4.6: Fitting a limb-brightened shell to the W4 loop. Smooth curve represents brightness calculated from a uniform shell model, convolved with the 60μm HIRES beam. The other curve is obtained by averaging 3 slices across the loop in the 60μm W4 image. Horizontal axis: angular distance from loop center in arcminutes; Vertical: pixel intensity in MJy sr^{-1}.

ionizing ultroviolet photons from the OB cluster.

Further study is needed to determine whether the loop is ionization bounded. The enhanced radio continuum emission on the inner loop argues in favor of the hypothesis, but the existence of the faint ionized gas halo around the loop is against it. The temperature gradient of the halo indicates the halo is centered on the H II region and also powered by the OB cluster. One possible explanation is that the wind-blown shell is quite patchy instead of a uniformly closed shell, so that the Lyman continuum photons can leak through and ionize the low density gas.

References

Fowler, J. W. & Aumann, H. H. 1994. HIRES and beyond. In *Science with High Spatial Resolution Far-Infrared Data,* ed. S. Terebey & J. Mazzarella (Pasadena: JPL 94-5), 1.

Heyer, M. H., Carpenter, J., Snell, R. L., & Schloerb, F. P. 1994. FCRAO CO Survey of the Second Quadrant. *Bull. Amer. Astron. Soc.*, **184**, 27.05.

Massey, P., Johnson, K. E., & DeGioia-Eastwood, K. 1995. The initial mass function and massive star evolution in the OB associations of the northern Milky Way. *Astrophys. J.*, **454**, 151.

Normandeau, M., Taylor, A. R., & Dewdney, P. E. 1996. A Galactic chimney in the Perseus arm of the Milky Way. *Nature*, **380**, 687.

Normandeau, M., Taylor, A. R., & Dewdney, P. E. 1997. The Dominion Radio Astrophysical Observatory Galactic plane survey pilot project: the W3/4/5/HB3 region. *Astrophys. J. Suppl.*, **108**, 279.

Whiteoak, J. B. Z. 1994. High-resolution images of the dust and ionized-gas distribution in the Carina nebula. *Astrophys. J.*, **429**, 225.

Chapter 5

Summary

Here I briefly summarize the work presented in this thesis, emphasizing on the significance and possible future impacts of the contributions made.

The most visible and effective algorithmic enhancement is the offset compensation destriping algorithm (Section 2.3). The method is basically an adaptive self-calibration scheme, which combines the image reconstruction and calibration processes. The visual appearance of the reconstructed images is improved tremendously. More importantly, the striping artifact is no longer a limit on the optimal number of iterations and the resolution achieved, since the striping power is washed out monotonically (instead of growing with the number of iterations). The added amount of computation is negligible. Due to these reasons, IPAC has adopted the offset compensation destriping in the production version of HIRES since the beginning of 1996, and all HIRES images provided to the astronomers are now free of striping, which used to be the most prominent artifact.

The other major contribution in the algorithm aspect is the cross log entropy maximization algorithm for the purpose of ringing suppression (Section 2.4.2). Although the ringing suppression was not employed in the IGA production software, I consider it by all means a more important and more interesting piece of work than the destriping algorithm. The striping artifact is due to instrumental imperfection (specifically, gain and offset variations in the *IRAS* detectors), while point source ringing is ubiquitous in astronomical image reconstruction problems and more fundamental in nature. In the family of multiplicative iterative methods pioneered by the Richardson-Lucy algorithm, there have been numerous efforts to overcome the problem. However, the cross log entropy maximization offers a new, distinctive, and effective venue, and is simple in concept and implementation. Moreover, the marriage of image reconstruction with robust statistics could have more profound impacts than ringing suppression alone.

The parallel computing aspect was what motivated the project and made possible the production of the Atlas itself. The parallelization problem was interesting and required a solution different from many common decomposition schemes, primarily due to the irregular positions and overlap of the data samples. This led to a parallelization strategy requiring a moderate communication overhead, and a satisfactory efficiency of 60% was achieved. Using the parallel code running on the Intel Paragon, nearly 5000 square degrees of sky was processed in two wavelength bands in less than a year (including some reprocessing due to changes in software and processing options). This compares with the roughly 600 square degrees in four wavelength bands that IPAC processes annually using workstations alone. The project also enlarged the horizons of scientific research performed using the Caltech parallel computing facilities, being the first large scale astronomical imaging program to run on the Intel Paragon.

Last but not least, the final product of the whole project – the *IRAS* Galaxy Atlas itself – is of tremendous value to the community of astronomers and astrophysicists. Many algorithmic and processing improvements were carried out, in an effort to make the Atlas images more valuable scientifically and convenient to use. In particular, the surface brightness of the images agrees with the released IPAC product *IRAS* Sky Survey Atlas, and the geometry and data calibration of the images allow straight-forward mosaicking. Also, the IGA images have much better correction for striping than the previous IPAC image products (both HIRES and ISSA). The IGA is available over thousands of square degrees, and spans a tremendous range of physical conditions. Thus the Atlas is destined to become a useful tool for astrophysical studies that require both the large spatial span and the high resolution.

Appendix A

Selected Images from the *IRAS* Galaxy Atlas

This appendix contains some interesting images from the *IRAS* Galaxy Atlas, selected and arranged by Susan Terebey (used by permission).

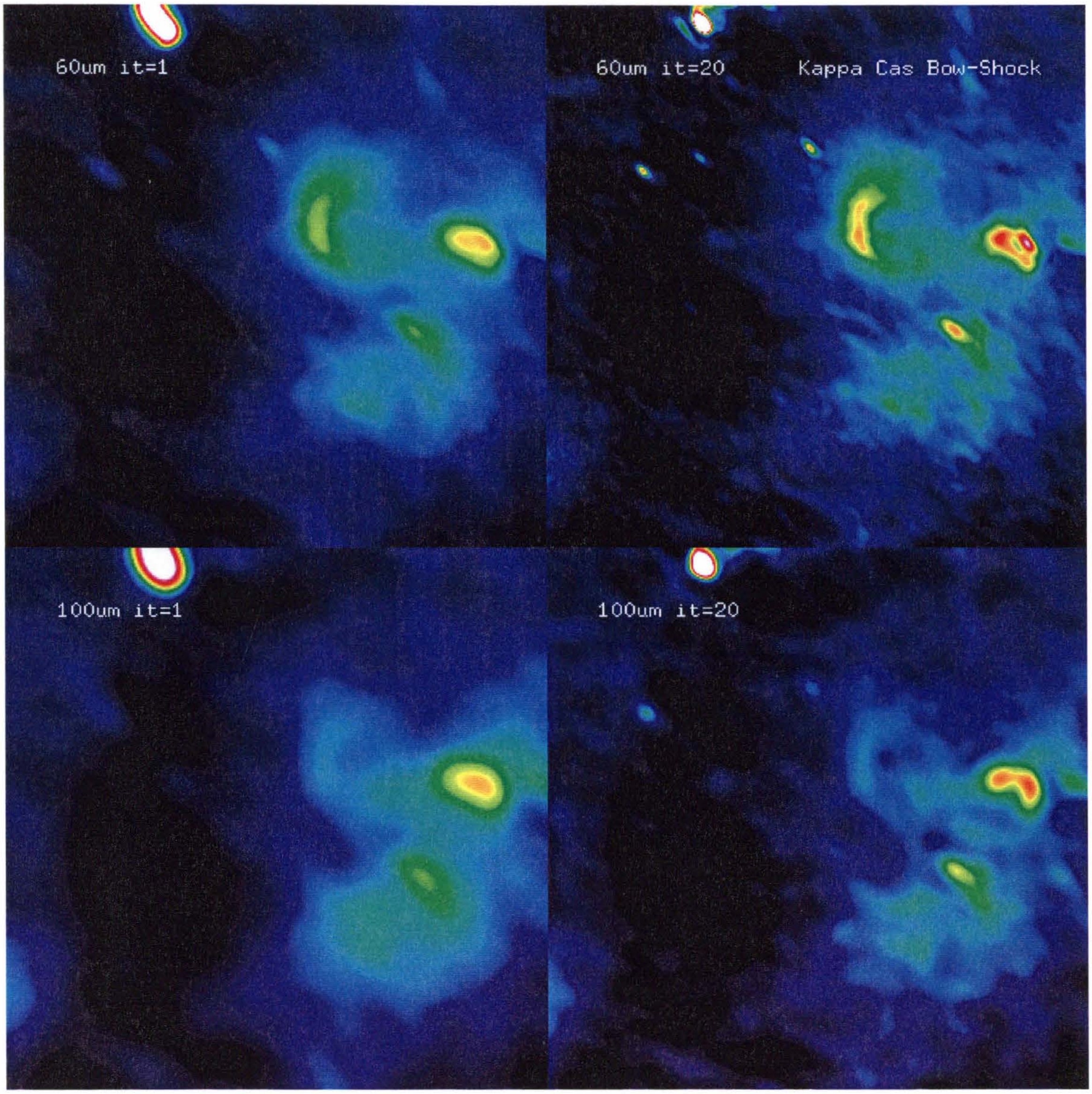

Figure A.1: A region in Cassiopeia. The resolution enhancement is crucial in recovering the bow shock structure near κ Cas in the 60 μm image. False colors are used to represent sky brightness (white > red > yellow > green > blue > black).

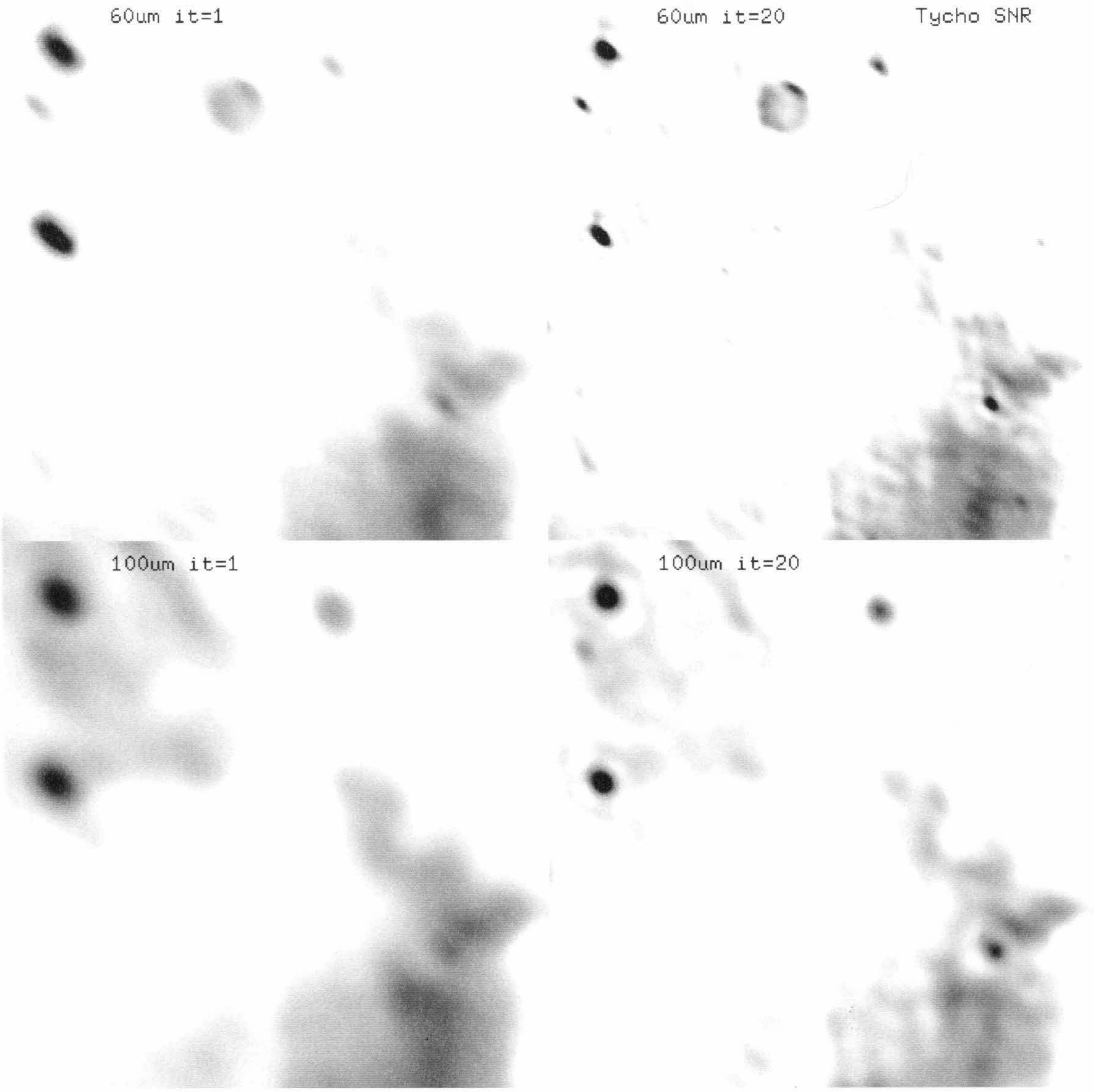

Figure A.2: Supernova remnant from Tycho's star. The shell structure is clearly seen in the 20th iteration 60 μm image. Tycho's star was a type I supernova that was observed in 1572 in the constellation Cassiopeia and was studied by astronomers in Europe, China, and Korea. Tycho Brahe's careful observations of its position have identified it with a known radio and X-ray source. Reverse tone is used (black is brighter).

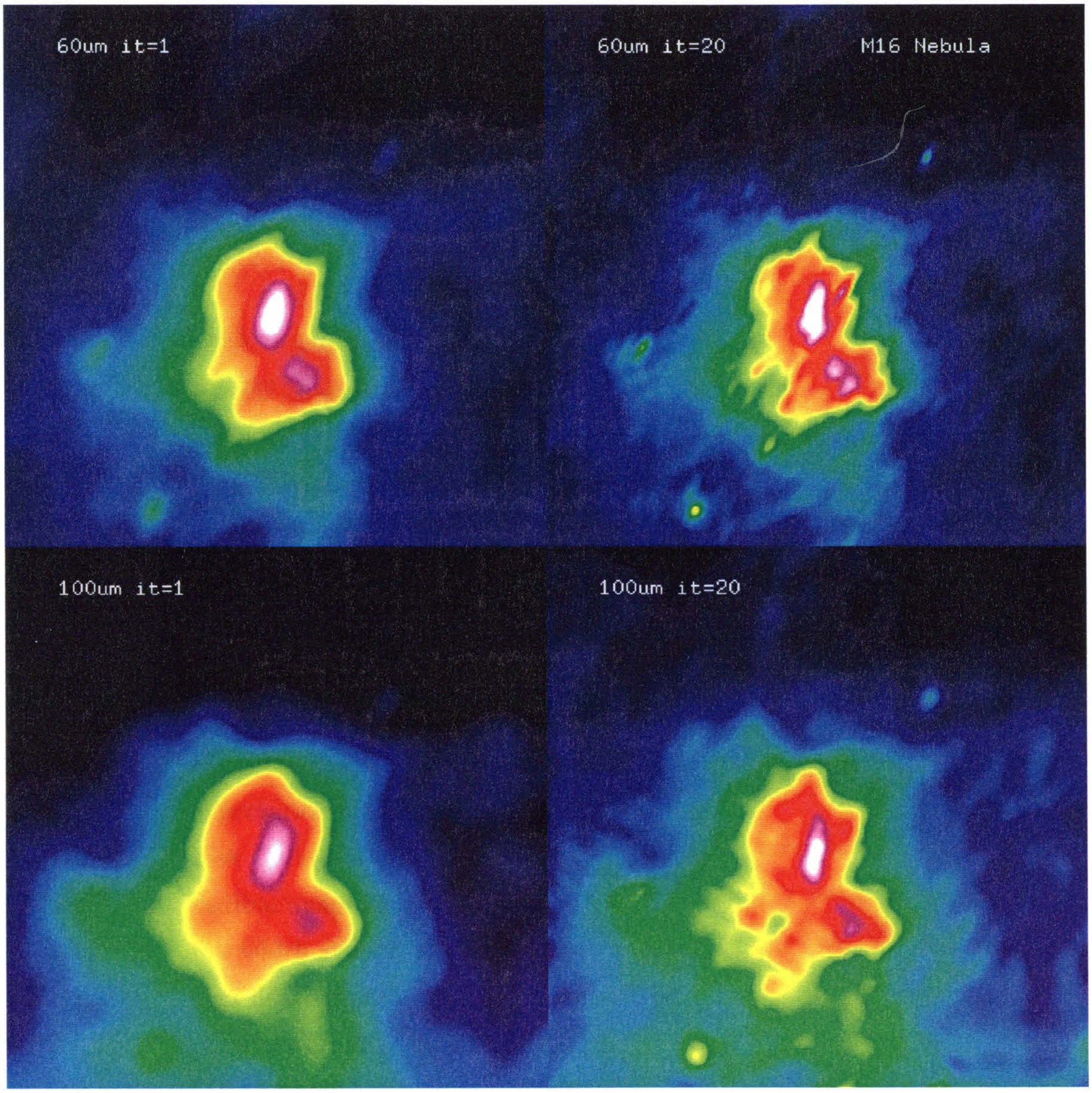

Figure A.3: The M16 nebula. False colors are used to represent sky brightness (white > red > yellow > green > blue > black).

Appendix B

Acronyms

AO	(*IRAS*) additional observation
BEM	HIRES beam sample map
BrkDet	Software in IGA production used to reproject and regroup detector data
CFV	HIRES correction factor variance map
CPU	central processing unit
CRDD	(*IRAS*) calibrated, reconstructed detector data
CVG	HIRES coverage map
DET	HIRES detector track map
DRAO	Dominion Radio Astrophysical Observatory
ECT	emission computed tomography
EM	expectation maximization (algorithm)
FCRAO	Five College Radio Astronomy Observatory
FITS	flexible image transport system
FWHM	full width at half maximum
GFLOPS	giga floating point operations per second
GPO	(US) Government Printing Office
HCON	(*IRAS*) hours-confirming (scans)
HIPPI	high performance parallel interface
HIRES	IPAC high resolution processing
HST	*Hubble Space Telescope*
IAU	International Astronomical Union
ICF	intrinsic correlation function

IGA	*IRAS* Galaxy Atlas
IMF	initial mass function
IMG	HIRES image (sky brightness map)
IPAC	Infrared Processing and Analysis Center
IRAS	*Infrared Astronomical Satellite*
IRTS	*Infrared Telescope in Space*
ISO	*Infrared Space Observatory*
ISRA	image space reconstruction algorithm
ISSA	*IRAS* Sky Survey Atlas
JPL	Jet Propulsion Labratory
KAO	Kuiper Airborne Observatory
LAUNDR	IPAC software to calibrate *IRAS* detector data
MART	multiplicative algebraic reconstruction technique
MCM	maximum correlation method
MLE	maximum likelihood estimate
MSC	MOST supernova remnant catalogue
MSX	*Midcourse Space Experiment*
MOST	Molonglo Observatory Synthesis Telescope
NASA	National Aeronautics and Space Administration
NGC	New General Catalogue of Nebulae and Clusters of Stars
NSSDC	National Space Science Data Center
NX	Intel's communication package running on the Paragon
OSF	Open Software Foundation, created by 9 computer vendors
OSF/1	operating system running on the Intel Paragon, released by OSF in 1990
PET	positron emission tomography
PHN	HIRES photometric noise map
PSC	(*IRAS*) Point Source Catalog
PSF	point spread function
PSR	pulsar
RAID	redundant arrays of independent disks (formerly "redundant arrays of inexpensive disks")
SNR	supernova remnant

SPARCstation	workstation made by Sun Microsystems
STScI	Space Telescope Science Institute
SUNMOS	Sandia-UNM Operating System
SmLAUN	software in IGA production to calibrate and subtract zodiacal emission from *IRAS* detector data
UNM	University of New Mexico
VLA	Very Large Array
YORIC	software in HIRES to perform image reconstruction using MCM

Colophon

This thesis was produced using the LaTeX version 2e (in 2.09 compatible mode) document preparation system by Leslie Lamport and the TeX version 3.1415 typesetting system by Donald Knuth. The LaTeX output was converted to printable PostScript page description language using version 5.58f of the `dvips` program by Radical Eye Software. Stuart Anderson adapted the `ucthesis` LaTeX 2.09 style file and AASTeX macros from the American Astronomical Society to produce the `srlthesis` style file, which conforms to the Caltech guidelines due to his efforts. This thesis uses a variant of this style file created by Deepto Chakrabarty, `srlthesis_chapref`.

The figures were created using a variety of software packages. Line drawings and image assembly were done using AppsoftDraw version 1.02 (Appsoft, Inc.) on the NeXT computer and IslandDraw version 4.0 (Island Software Corp.) on Sun SPARCstation. Plots were made with Mathematica version 2.2 (Wolfram Research, Inc.) and `gnuplot` UNIX version 3.5 (Colin Kelley and Thomas Williams). FITS images were displayed and captured in grayscale or color using Skyview version 3.15 developed at the Infrared Processing and Analysis Center. Surface plots were made using the image processing package Khoros version 1.0 (University of New Mexico). The PBM+ package version 4.1 by Jef Poskanzer was used extensively for conversion between different image formats and other adjustments.